A SYSTEMATIC SURVEY OF REVERSIBLE COVALENT DIPEPTIDYL INHIBITORS OF THE SARS-COV-2 MAIN PROTEASE

A REVERSIBLE CHEMOGENETIC SWITCH FOR CHIMERIC ANTIGEN RECEPTOR T CELLS

A Dissertation

by

ZHI GENG

Submitted to the Graduate and Professional School of
Texas A&M University
in partial fulfillment of the requirements for the degree of

DOCTOR OF PHILOSOPHY

Chair of Committee,	Wenshe Ray Liu
Committee Members,	Arthur Laganowsky
	Pingwei Li
	Frank Raushel
Head of Department,	Simon W. North

August 2023

Major Subject: Chemistry

ABSTRACT

SARS-CoV-2 has caused a global pandemic since emerged from Wuhan, China. The Main protease of this virus is an important target for drug discovery. To test the real inhibition effect of the developed small molecule inhibitors to Mpro, live-virus based assay is normally used. However, this can be problematic because a lot of other proteases that play important roles in the life cycle of this virus share a similar catalytic mechanism with Mpro, thus would be inhibited by these inhibitors as well. The live-virus based assay is also tedious, dangerous, and requires BSL-3 level laboratory which is not equipped by many institutions. We developed a cellular assay based on the cellular toxicity of Mpro, utilizing a Mpro-eGFP construct that can be directly quantified by flow cytometry to test the inhibition effect of inhibitors developed.

Combined with the cellular assay we developed, we systematically studied the inhibition effect for Mpro of a series of dipeptidyl inhibitors we developed using enzymatic inhibition assays, X-ray crystallization, live-virus based assays and cytotoxicity and in cell stability. The S2 binding pocket of Mpro was found to have a potential to accommodate larger and complicate binding groups and two compounds, MPI60 and MPI61 was selected as two compounds with the most significant potential for clinical study.

Chimeric antigen receptor (CAR) T cell therapy has shown its enormous ability in cancer treatment, while the uncontrollable T cell activation arise in potential of serious side effects. Many efforts have been done to control the activation of CAR-T cells but with obvious drawbacks. We propose a chemogenetic recurring switch on the basis of the third generation CAR design, using HCV-NS3 as the switch and ASV as the regulator. Compared to the standard CAR19 product, this switchable CAR-T design displayed excellent tumor killing effect both *in vitro* and *in vivo*.

ACKNOWLEDGEMENTS

Now that I'm writing this acknowledge part of my PhD thesis, everything still feels very surreal. When I was in the second year or so, talking to my friend Chesley and Lauren, I told them I feel like this journey will never end, because five years seems so long and I was so emerged and suffocated in my everyday life back then. But here I am, getting to the end of the tunnel.

I would like to thank my primary investigator, Dr. Wenshe Liu. When I got into the lab as a first-year graduate student, I felt like he was always looking at me like he's looking at a puppy. Over the years things have changed, his look certainly had more complicated components, but I'm lucky enough to have that kind-hearted care from him as a mentor. He always tries to look out for me, academically, psychologically, and for that I'm more than grateful.

I would like to thank my friends from the lab, without whom I would never be able to accomplish what I have done. They're my teachers, my supporters, when I got crazy, they tolerate me. As a student who transferred from doing chemistry to doing biological research, I struggled a lot at the beginning, Dr. Wenyue Cao was there, teaching me about all the basic techniques, helped me to build my confidence; when I feel overwhelmed, Trae and Kaitlin, their beautiful babies, Rosie and Tino, are always there to give me comfort. A special thank you goes to Amy Liu, who always try to give me hop for the future and warm me with love and care.

I would like to thank my gang from the Institute of Bioscience and Technology. Thank you for tolerating my quirkiness, my endless anxiety and drama. From all my friends in IBT, Denelle Orellana is my one and only rock that I can rely onto, who understands all the pain and stress and fear, who would never turn their back on me.

Lastly, thank my family back in China. You will always be my dream and my tears.

CONTRIBUTORS AND FUNDING SOURCES

Contributors

This work was supervised by a dissertation committee consisting of Professor Wenshe Ray Liu, Professor Arthur laganowsky and Professor Frank Raushel of the Department of Chemistry, and Professor Pingwei Li of the Department of Biochemistry and Biophysics.

The compounds synthesized in Chapter II and Chapter III were synthesized by Dr. Yugendar R. Alugbelli, Dr. Yuying Ma, Dr. Xinyu Ma, Dr. Veerabhadra R. Vulupara, Dr. Sandeep Atla and Kaustav Khatua, the antiviral assay data was collected by Sorrento Therapeutics. The *in vivo* M^{pro} quantification from viral infection was carried out by Sankar P. Chaki in Professor Benjamin Neuman's laboratory. *In vitro* characterization of inhibitors was carried out by Dr. Erol C. Vatansever, Dr. Kai S. Yang and Kaustav Khatua. The cellular assay was conducted in part with Dr. Wenyue Cao.

In Chapter IV, the plasmid construction was partially done by Dr. Chia-chuan Cho, the cell killing assay and character assays, animal experiments were conducted by Dr. Wenyue Cao under assistance of Zhi Geng.

Funding Sources

Graduate study was supported by a fellowship from Texas A&M University.

This work was supported by Welch Foundation (grant A-1715), National Institutes of Health (grants R35GM145351 to W.R.L., R21AI164088 to S.X., and R21EB032983 to W.R.L.), Texas A&M X Grants, and the Texas A&M EDGES Fellowship Program. Given that there are a substantial number of papers published about the MPro inhibitor development, we are not able to cite all of them. We apologize for missing citing any critical publications.

NOMENCLATURE

CoV	Coronavirus
MERS-CoV	the Middle East respiratory syndrome coronavirus
SARS-CoV	Severe acute respiratory syndrome coronavirus
SARS-CoV-2	Severe acute respiratory syndrome coronavirus 2
RNA	ribonucleic acid
Mpro	Main protease
PLpro	Papain-like protease
Gln	Glutamine
ACE-2	Angiotensin-converting enzyme-2
ORF	Open reading frame
RTC	Replicase-transcriptase complex
nsps	Non-structual proteins
RdRp	RNA-dependent RNA polymerase
COVID-19	Coronavirus disease 2019
P-pg	P-glycoprotein multidrug transporter
CAR	Chimeric Antigen Receptor
CD3ζ	T-cell surface glycoprotein CD3 zeta chain
scFv	single- chain variable fragment
CD28	Cluster of differentiation 28
CRS	cytokine release syndrome
ICANS	Immune effector cell-associated neurotoxicity syndrome
TLS	tumor lysis syndrome

PROTAC	proteasome-targeting chimera
TCR	T cell receptor
TMPRSS2	transmembrane protease serine 2
CtsL	cathepsin L
CtsB	cathepsin B
CPE	cytopathogenic effect
FRET	Förster resonance energy transfer
CFP	cyan fluorescent protein
YFP	Yellow fluorescent protein
eGFP	enhanced green fluorescent protein
IC50	half maximal inhibition concentration
EC50	half maximal effective concentration
HCV	Human hepatitis virus C
PRNTs	Plaque reduction neutralization tests
SSC-A	Size scatters-Area
SSC-H	Size scatters-Area
FSC-A	Forward scatters-Area
FITC-A	Fluorescein isothiocyanate-Area
HCQ	hydroxychloroquinine
CQ	chloroquinine
DCM	dichloromethane
DMAP	4-Dimethylaminopyridine
EDC	1-Ethyl-3-(3-dimethylaminopropyl)carbodiimide

DMSO	Dimethyl sulfoxide
CBZ	carboxybenzyl
BOC	*tert*-butyloxycarbonyl
CC50	half maximal cytotoxicity concentration

TABLE OF CONTENTS

LIST OF FIGURES

Page

LIST OF TABLES

Page

CHAPTER I

INTRODUCTION AND LITERATURE REVIEW

SARS-CoV-2 AND DRUG DISCOVERY

Coronaviruses (CoVs) are RNA pathogens that infect vertebrates including humans. In the 1960s, mildly pathogenic human CoVs were discovered[1], but the first epidemic human CoV, severe acute respiratory syndrome SARS-CoV, emerged in 2003[2-5]. In 2012, the Middle East respiratory syndrome MERS-CoV appeared and caused an outbreak, resulted in nearly 1000 deaths until 2020[6]; in the year end of 2019, SARS-CoV-2 quickly spilled from Wuhan, China, causing a global pandemic and contributed to millions of deaths over the past few years. All three pandemic CoVs were believed originated from animals and spread to humans during close human-animal interactions[7, 8].

Coronaviruses are a well-known source of respiratory illness in humans[9-12]. It is the primary cause for common cold, manifesting as a mild illness, contributing to up to 20% of all common cold cases[13]. There have been many identified hosts for the coronavirus, including rodents, feline, canine, turkey, swine, and humans. Bats are known to serve as the primary reservoir expect for MERS-CoV reservoir being dromedary camels[12, 14].

Belonging to the genus *Betacoronavirus,* SARS-CoV-2 is an enveloped positive-sense single-stranded RNA virus[7, 8, 15, 16]. It contains an RNA genome of about 30kb, which encodes two large overlapping polyprotein precursors, pp1a and pp1ab, four structural proteins: spike, envelope, membrane, and nucleocapsid, and several accessory proteins. To accomplish the life cycle, the virus needs to process the two polyproteins (pp1a/pp1ab) into individual nonstructual

proteins[17, 18]. This cleaving process is performed by two viral proteases: main protease (Mpro, also named 3CL protease) and papain-like protease (PLpro)[15]. Thus, these proteases are very important target for antiviral drug development. What's worth noticing is that Mpro exclusively cleaves polypeptides after a glutamine (Gln) residue, which no known human protease shows the same character, this may reduce the potential of having side effects when developing drugs specific for Mpro[19, 20].

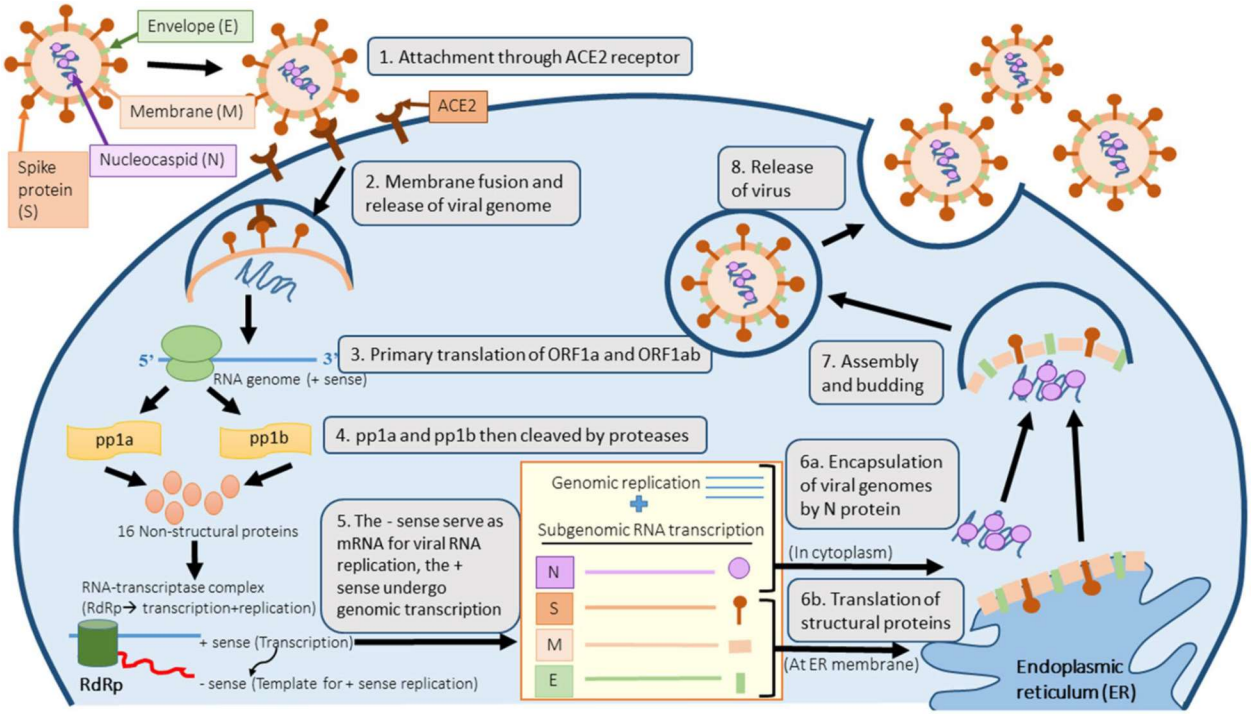

Figure 1. The replication cycle of SARS-CoV-2. Reprinted from [21]

The SARS-CoV-2 virus gets attachment with the host cell and get entry though its spike protein, which can be divided into two parts: the S1 receptor binding domain and the S2 fusion domain[22]. The spike protein binds to the angiotensin-converting enzyme-2 (ACE-2) receptor after activated by the host cells, then the virus fuse to the cell membrane and release the viral RNA genome into the host cytoplasm. The open reading frames ORF1a and ORF1b were then translated into polyproteins pp1a and pp1b, which were then cleaved into non-structural proteins (nsps). These nsps form a replicase-transcriptase complex (RTC), which produces prodcuts such as RNA-

dependent RNA polymerase (RdRp), which works in replicating the viral RNA. Then subgenomic mRNAs are produced and translated into viral proteins and packaged into new virions, which are then released through exocytosis.

SARS-CoV-2 Main protease

Main protease is a protease that processes the polypeptides translated from the genome RNA of the SARS-CoV-2 virus into structural and non-structural proteins, which is vital for the life cycle for the SARS-CoV-2 virus[15]. Because of its importance to the virus replication and controlling to the host cells, this protease is a very important druggable target. SARS-CoV-2 and SARS-CoV share a remarkable 96% sequence identity in their decoded Mpro[23].

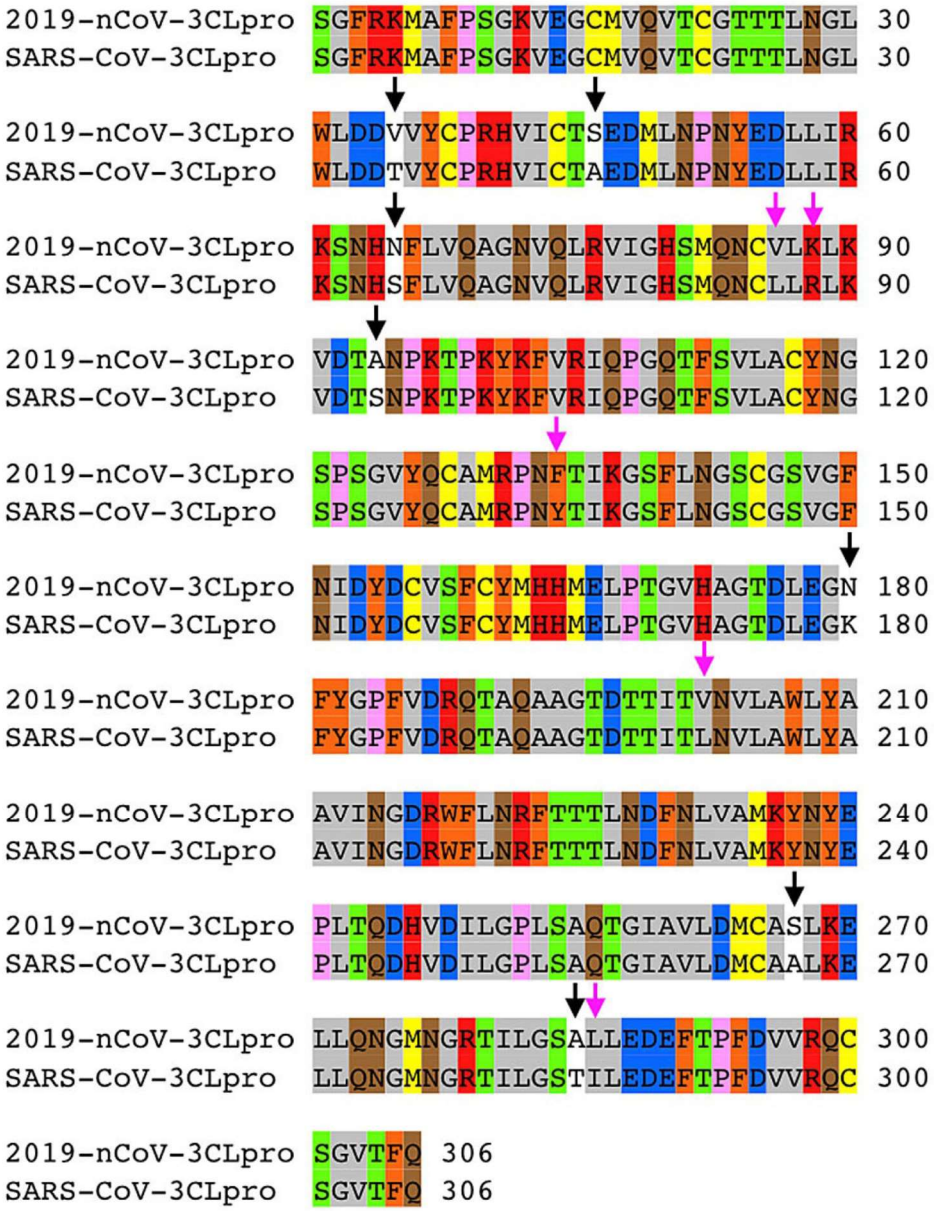

Figure 2. Sequence alignment for the amino acids between the SARS-CoV-2 (2019-nCoV) 3CLpro and the SARS-CoV 3CLpro. Conserved (pink arrows) and nonconserved (black arrows) mutations are highlighted. Gray: hydrophobic aliphatic, orange: neutral aromatic, yellow: thiol and sulfide, green: hydroxy, red: basic, blue: carboxylic acid, brown: primary amide, pink: proline. Reprinted from [23]

Mpro is approximately 34.21 kDa per monomer and is matured in a dimeric form[24]. The monomers are enzymatically less active, they have three domains, including domain I, domain II, and domain III[25, 26]. The catalytic site of Mpro is located in the intersection of domains I and II, which can be divided into mainly five binding pockets, S1, S2, S3, S4, and S5[27, 28]. The O^{β}

atom of glutamine could bind to the oxyanion hole (residues 143-145) of S1, and then the thiol of Cys145 could attack the C atom of glutamine as a nucleophile[29, 30]. Therefore, P1 almost always requires glutamine or lactam warhead[31-33]. The catalytic dyad of Mpro is formed by Cys145 and His41[34, 35]. This zwitter catalytic dyad needs to be activated by energetical water, which is maintained by His164 and Asp 187[36-40].

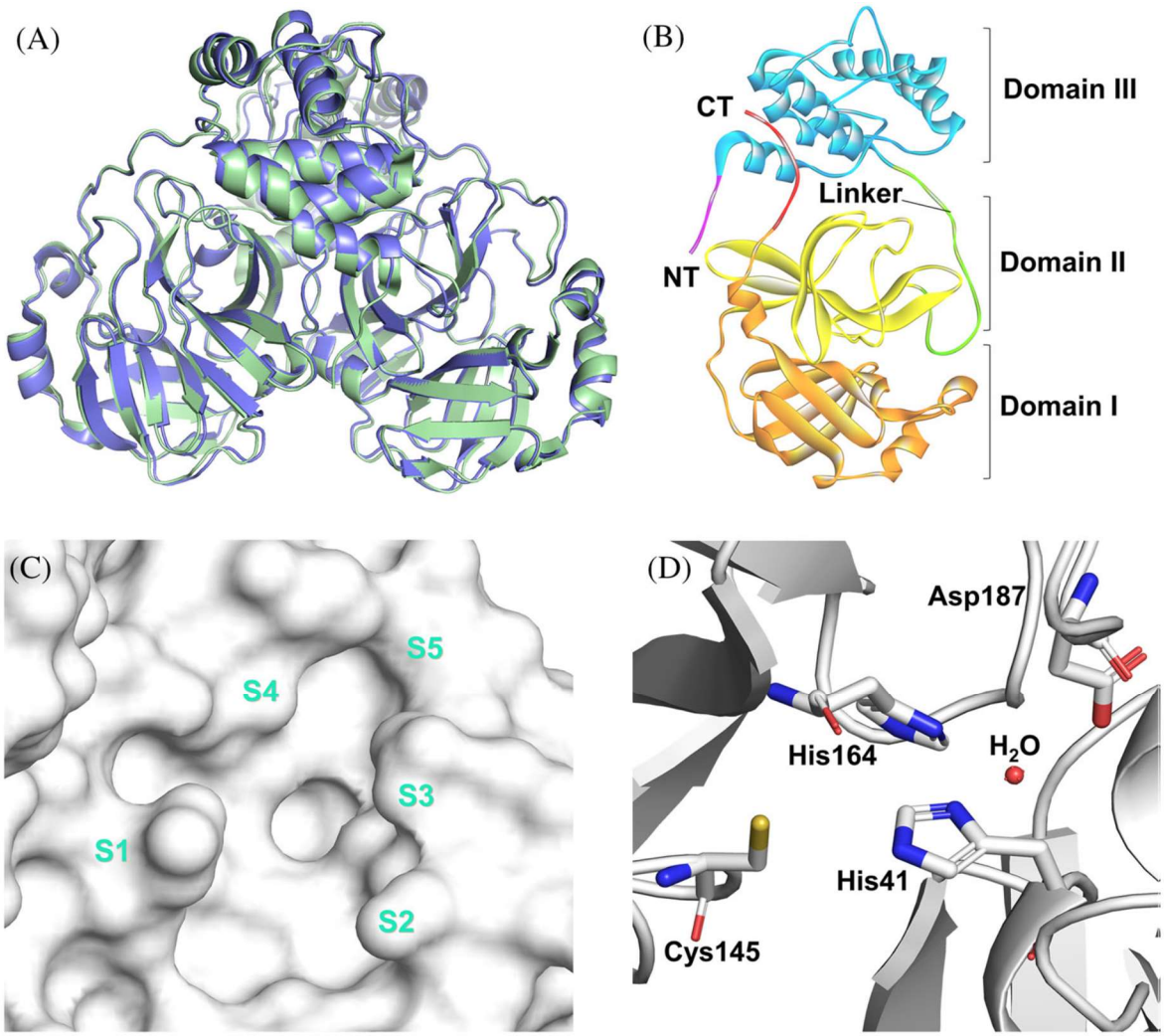

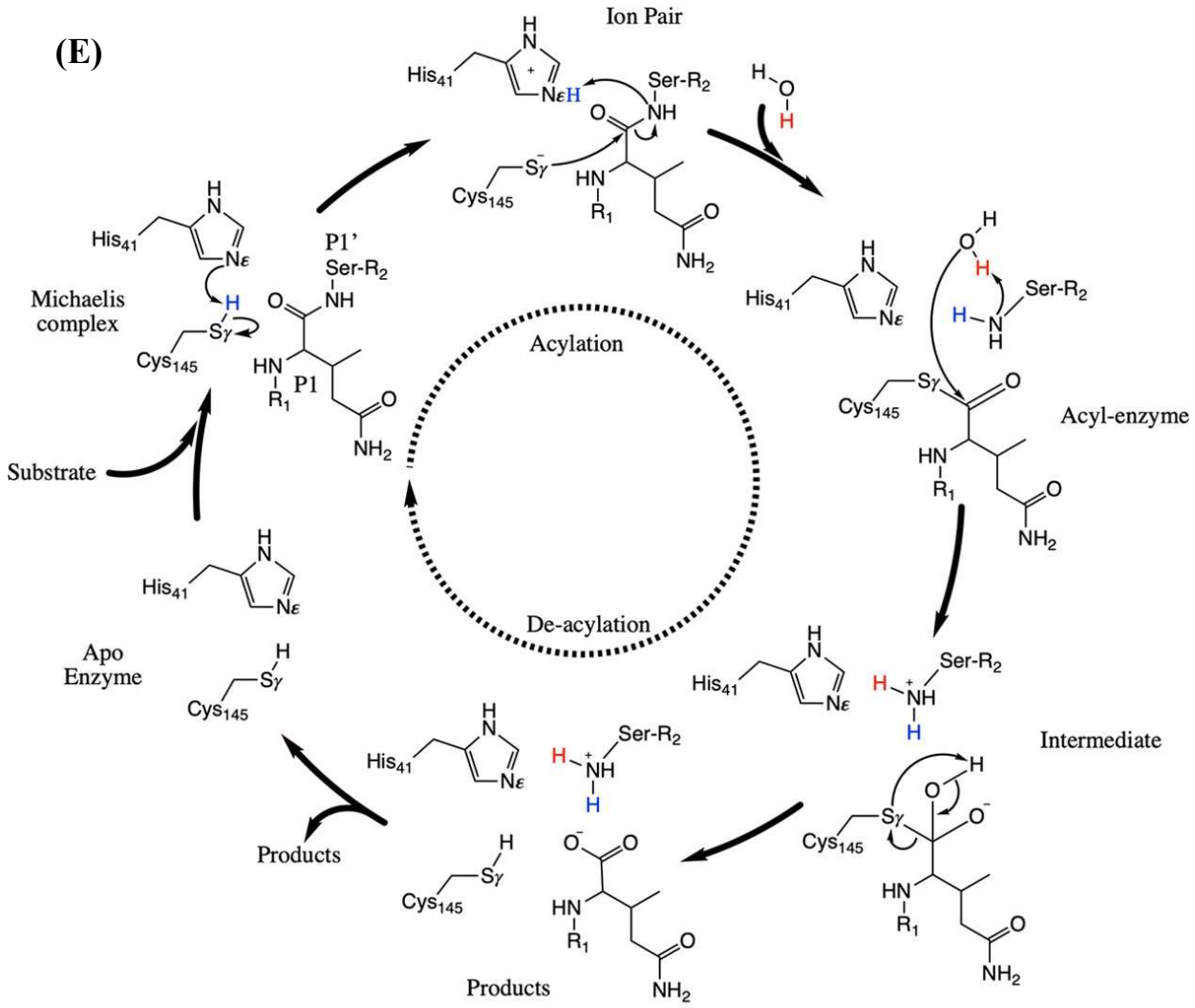

Figure 3. (A) The 3D structure of severe acute respiratory syndrome coronavirus 2 (SARS-CoV-2) 3CLpro (pale green, PDB: 6XHU) and severe acute respiratory syndrome coronavirus (SARS-CoV) Mpro (slate, PDB: 1UJ1). (B) Three structural domains (domain I: orange, domain II: yellow, domain III: blue) of SARS-CoV-2 Mpro monomer. (C) The surface representation for the catalytic pocket (sub-pockets: S1–S5) of SARS-CoV-2 3CLpro. (D) The amino acid residues in the active site of SARS-CoV-2 3CLpro. Reprinted from [24](E) The catalytic mechanism of 3CLpro on the hydrolysis of amide substrate. Reprinted from [41]

With the current coronavirus disease 2019 (COVID-19) pandemic prevailing and future CoV pandemics looming, it is paramount to develop orally available small-molecule drugs that can be broadly used as CoV antivirals for both treatment and prevention. So far, three orally

available medications have been approved for COVID-19 patient emergency use, including remdesivir, molnupiravir, and PAXLOVID™[42-44]. Both remdesivir and molnupiravir are nucleotide analogues. Remdesivir is an RNA replication inhibitor and known to have low efficacy in inhibiting SARS-CoV-2[45]. Differently, molnupiravir is an RNA mutagen. It reduced the death and hospitalization rate by 50% compared to placebo according to clinical trials[46]. However, its mutagen nature that drives SARS-CoV-2 to undergo mutagenesis warrants use with caution. Unlike remdesivir and molnupiravir, PAXLOVID™ is a combination therapy of nirmatrelvir and ritonavir. Nirmatrelvir is a reversibly covalent inhibitor of the SARS-CoV-2 main protease. Ritonavir is a human cytochrome P450 3A4 inhibitor that improves the metabolic stability of nirmatrelvir[47]. PAXLOVID™ failed as a pre-exposure prophylaxis method in clinical trials and its potential toxicity requires an administration period of 5 days. The current published results have shown that nirmatrelvir is a substrate of P-glycoprotein multidrug transporter (P-pg) that continuously pumps various and structurally unrelated compounds to the outside of human cells[44]. P-gp is known with varied expression levels in different tissues. Although ritonavir is a P-gp inhibitor as well, the expression variation of P-gp in different tissues likely causes different inhibition efficacy of PAXLOVID™ in different tissues[48]. This may explain why many patients had COVID-19 rebound after stopping taking PAXLOVID™ and SARS-CoV-2 from these patients with COVID rebound did not show resistance to PAXLOVID™. Due to concerns related to existing small molecule SARS-CoV-2 antivirals, the research of developing SARS-CoV-2 antivirals that have characteristics better than existing antivirals is still urgent.

CHIMERIC ANTIGEN RECEPTOR T CELL THERAPY

The idea of T cells engineered with Chimeric Antigen Receptor (CAR) has emerged as an important tool for cancer therapeutic use, especially blood cancers[49-57]. CAR-T cell

therapeutics that have been approved by the U.S. Food and Drug Administration for clinical use include Abecma™, Breyanzi™, Carvykti™, Kymriah™, Tecartus™, and Yescarta™. Many others are on clinical trials[58-65].

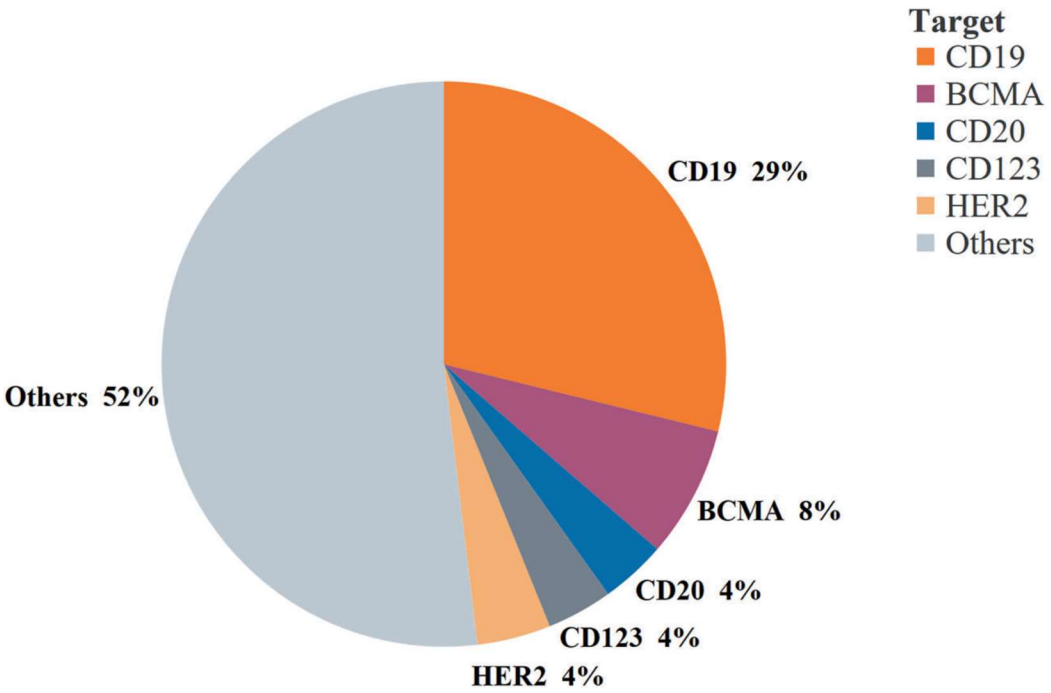

Figure 4. Percentage of targets in the 2019 global CAR-T cell pipeline. The top 5 CAR-T cell targets were selected, and a pie chart was plotted based on data from the Cancer Research Institute. Reprinted from [66].

CARs are designed in a modular fashion that typically consists of an extracellular target-binding domain, a hinge region, a transmembrane domain that anchors the CAR to the cell membrane, and one or more intracellular domains that transmit activation signals. Depending on the number of costimulatory domains, CARs can be classified into first (CD3ζ only), second (one costimulatory domain + CD3ζ), or third generation CARs (more than one costimulatory domain + CD3ζ)[67].

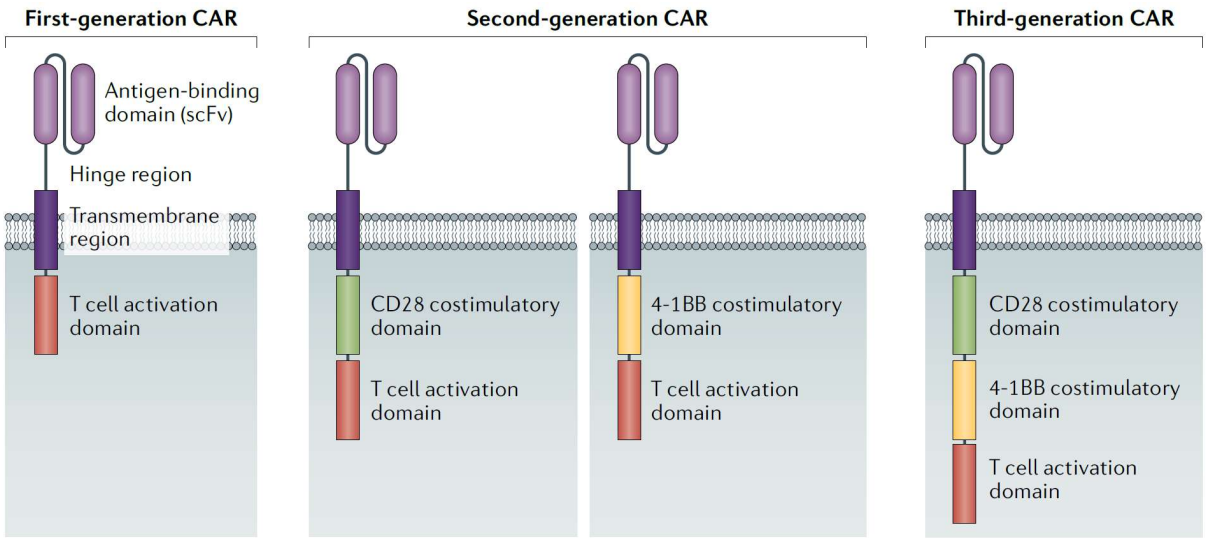

Figure 5. Structure of first- generation, second- generation and third- generation chimeric antigen receptors (CARs) Reprinted from [68].

First-generation CAR

First- generation CARs consist of a single- chain variable fragment (scFv)- based antigen-binding domain linked via hinge and transmembrane domains to a T cell activation domain derived from the CD3ζ subunit of the T cell receptor complex. This CAR design failed to work for eradicating cancer cells due to inefficient activation[69, 70]. A coinstimulatory domain was then introduced to form the second-generation CAR.

Second-generation CAR

Second-generation CARs include the components of the first-generation CAR but with the addition of a costimulatory domain, typically derived from CD28 or 4-1BB[71]. Introduction of costimulatory domains enhanced T cell activation in real world and clinical trials. Clinical trials with CARs incorporating CD28 or 4-1BB intracellular domains showed similar response rates in patients with hematologic malignancies. However, the persistence of T cells engineered with these two CAR designs is strikingly different. Preclinical studies identified these T cell persistence differences in head-to-head comparisons of CD28- and 4-1BB-based CAR T cells in animal

models[72, 73]. Clinical trials for B cell malignancies have shown that CD28-based CAR T cells are typically undetectable beyond 3 months[74, 75], whereas 4-1BB-based CAR T cells can persist in patients for several years after treatment[76]. Exhaustive studies indicate that signaling through CD28-based CARs results in more rapid T cell activation, proliferation, cytolysis, and increased glycolysis, but shorter T cell persistence.

Third-generation CAR

Third-generation CARs include the components of the first- generation CAR plus two costimulatory domains in tandem[77].

Limitations and safety concerns

Although powerful, CAR-T cell therapy has very serious safety concerns. Once infused into patient body, it's very difficult to control CAR-T cell's function. The release of certain cytokines might trigger cytokine release syndrome (CRS)[78], it can also result in Immune effector cell-associated neurotoxicity syndrome (ICANS)[79]. The tumor cell killing process may trigger tumor lysis syndrome (TLS) and anaphylactic effects[80]. The fact that almost all the surface antigen targeted on cancer cells can be found some where elsewhere results in potential on-target/off tumor toxicity. Thus, a better way to control CAR-T cells is in demand[81-83].

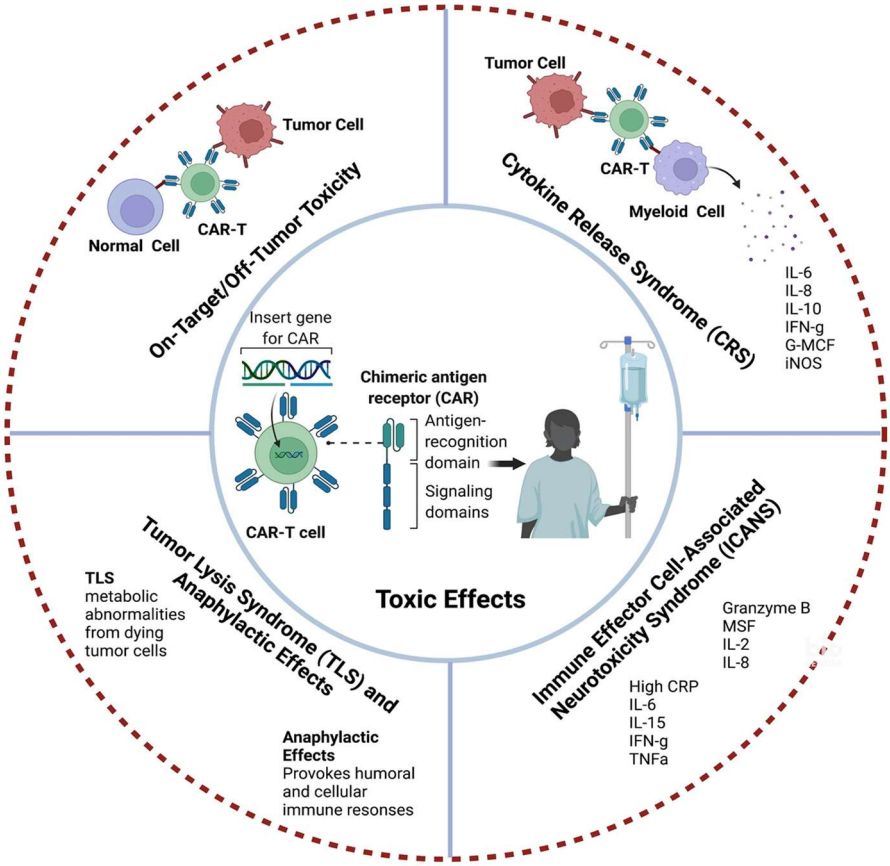

Figure 6. Toxic effects of CAR-T cell therapy

Switchable CAR-T cell therapy

To overcome the side effects of CAR-T cell therapies, a lot of efforts have been made. A strategy is to incorporate a switch in the CAR structure to control the function of CAR-T cells. If CAR-T cell activity can be shut down by a switch, the side effects may be partially eliminated. If the CAR-T cell can again be turned on, this can also delay CAR-T cell exhaustion and antigen escape. Several designs have been developed for this goal. First category is bivalent switches, they have two ends, one binds to the tumor cells, the other one binds to the CAR[84-91]. The two ends can be both small molecules, one small molecule and one biologic, or both biologics. When binding to both ends, they trigger T-cell activation, and when side effects are observed, the bivalent switch can be withdrawn to stop the T-cell activation. Another strategy is to use a small molecule

rapamycin to initiate dimerization between KFBP12-fused transmembrane/intercellular CAR component and an FRB-fused membrane bound scFv to generate a fully functional CAR of T cell surface[92, 93]. For the two strategies mentioned above, both turning on and turning off can be achieved. However, both strategies include complicated multiple components. The bivalent switch will need to pass clinical tests for uncertain biosafety, metabolic stability, toxicity and immunogenicity along with its regulated CAR-T therapy. Although rapamycin is approved clinically, it exhibits potent immunosuppressive activity that contradicts the underlying concept of CAR-T therapy[94]. The binding of rapamycin to endogenous proteins including FKBP12 and the mTOR complex may also lead to unpredicted CAR functions and interfere with accurate dosing of rapamycin. To eliminate CAR-T cells when side effects are observed, a suicide switch has been developed. It's based on rimiducid-triggered caspase-9 dimerization[95-97]. Unlike the strategies described above, the elimination of CAR-T cells is permanent. This is the major drawback of this strategy, to restore the therapeutic effect, T cells must be infused again. To control CAR display on T cells, an approach that is similar to the proteasome-targeting chimera (PROTAC) concept was invented[98, 99]. In this approach, a small molecule was used to control the cleavage of a degron that was fused to a CAR. This switch allows CAR display on T cells in the presence of a clinically approved small molecule. But withdrawing the small molecule will only prevent further CAR presentation and have no effects on the preexisting CAR. When side effects such as CRS are observed, withdrawing the controlling small molecule will not lead to immediate alleviation effects. Many safety concerns still remain. Another way to potentially turn off the CAR-T cell activity is to use dasatinib, a small molecule multityrosine kinase inhibitor, to suppress TCR-mediated signal transduction[100-103]. As a potentially generic switch for CAR-T cell therapeutics, dasatinib has been assessed in preclinical studies as a reversible switch. However,

the inhibitory effect of dasatinib is not robust in activated CAR-T cells[101]. Moreover, dasatinib is a nonspecific immunosuppressive drug that can suppress all T cells leading to other safety concerns[104].Therefore, a reversible CAR-T cell switch that is ultimately simple in its composition, allows quickly turning on and off the CAR-T cell activity, and resolve many concerns

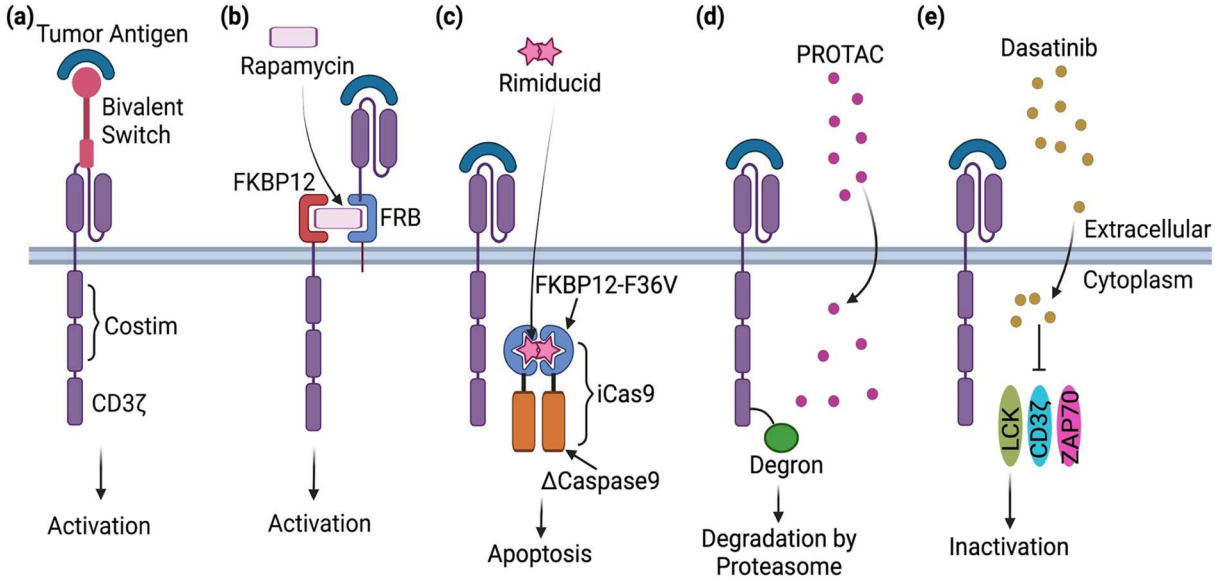

of existing switches is still an urgent and unmet need.

Figure 7. Switchable CAR-T systems that have been developed (generated by BioRender). Costim: costimulatory domain; iCas9: inducible caspase 9; PROTAC: proteasome-targeting chimera.

CHAPTER II

DEVELOPMENT OF A NOVEL CELLULAR ASSAY FOR SARS-CoV-2 INHIBITORS*

INTRODUCTION

COVID-19 is a global pandemic that has caused significant loss of life and disruption to societies worldwide. As of May 26th, 2021, the number of confirmed cases was over 167 million, with over 3.4 million deaths reported. The current approach to controlling the spread of the virus is through vaccination campaigns, targeting the Spike protein of the SARS-CoV-2 virus[105]. However, the highly mutable nature of the Spike protein has resulted in the emergence of new strains, leading to concerns about the efficacy of current vaccines against these new variants[23, 106, 107]. Spike protein shares only 76% identity between SARS-CoV-1 and SARS-CoV-2, despite the two share overall 82% genome sequence identity[17]. Despite the focus on vaccines, the need for targeted therapeutics for the treatment of patients with severe symptoms remains urgent. A small molecule medication targeting a conserved gene in SARS-CoV-2 could be a more effective way of containing the pandemic in both prevention and treatment, as it is easier to manufacture, store, deliver and administer, and less likely to be evaded by the virus.

The main protease (MPro) of SARS-CoV-2 is a potential target for drugs[108, 109] due to its high degree of conservation (96% protein sequence identity shared much higher than the overall 82% between SARS-CoV and SARS-CoV-2 is genome sequence identify shared between the two viruses[23])and work that has been done in developing MPro inhibitors[110-112].

*This chapter is reprinted with permission of Wenyue Cao, Chia-Chuan Dean Cho, Zhi Zachary Geng, Namir Shaabani, Xinyu R. Ma, Erol C. Vatansever, Yugendar R. Alugubelli, Yuying Ma, Sankar P. Chaki, William H. Ellenburg, Kai S. Yang, Yuchen Qiao, Robert Allen, Benjamin W. Neuman, Henry Ji, Shiqing Xu, and Wenshe Ray Liu *American Chemistry Science Central Science* **2022**, 8 (2), 192–204. DOI 10.1021/acscentsci.1c00910. Copyright 2022 The Authors. (https://pubs.acs.org/doi/full/10.1021/acscentsci.1c00910)

The general strategy for developing these inhibitors involves synthesizing an active site inhibitor, testing its enzymatic inhibition, and then conducting crystallographic and antiviral analysis optimize the drug. For most medicinal chemists, the bottleneck in this drug discovery process is the antiviral assay that requires the use of a BSL3 facility which is often not accessible. The antiviral assay itself may also lead to misleading results about the real mechanism of an MPro inhibitor. In the life cycle of SARS-CoV-2, there are several proteases that play critical roles. These proteases include transmembrane protease serine 2 (TMPRSS2), cathepsin L (CtsL), cathepsin B (CtsB), papain-like protease (PLPro), main protease (MPro), and furin. TMPRSS2 primes Spike for interactions with the host receptor ACE2 during the virus entry process[113]. CtsL helps in the membrane fusion of the virus with the endosome to release the virus RNA genome into the host cytosol[114]. CtsB has also been suggested to have a role in the SARS-CoV-2 entry[115]. After the RNA is released, it is translated by the host ribosome to form two large polypeptides, ORF1a and ORF1ab, which are processed into 15 mature nonstructural proteins (nsps) by PLPro and MPro. Some nsps package into an RNA replicase complex that replicates both genomic and subgenomic RNAs, while furin hydrolyzes Spike to prime it for new virion packaging and release[116]. Inhibition of MPro will prevent the virus from forming a functional virus particle, which is a target for antiviral treatments. Inhibiting other proteases, such as TMPRSS2, CtsL, and CtsB, could also potentially impact the SARS-CoV-2 life cycle, but MPro inhibition appears to be a more well-established target due to its conserved nature and essential role in the virus life cycle. However, the interplay between these proteases and MPro still requires further investigation. MPro, PLPro, CtsB, and CtsL are cysteine proteases with a similar catalytic mechanism and TMPRSS2 and furin are serine proteases. Some developed MPro inhibitors are prone to form covalent adducts with serine proteases as well as cysteine proteases, which can cause

unselective inhibition of multiple proteases[117, 118]. The localization of these proteases in different parts of the host cell also requires different characteristics in their inhibitors, such as cellular permeability and pH sensitivity. The antiviral assay of a developed MPro inhibitor may not necessarily reflect inhibition of MPro and can cause misunderstanding, which is why a direct reflection of MPro inhibition in the host cell is crucial for the assessment and optimization of MPro inhibitors. In order to effectively inhibit the SARS-CoV-2 virus, it is important to target the proteases that play a critical role in its life cycle, such as MPro, PLPro, CtsB, CtsL, TMPRSS2, and furin. These proteases have different catalytic mechanisms, localizations in host cells, and sensitivities to inhibitors. The inhibitors currently developed for MPro have covalent warheads, such as aldehyde and ketone, making them prone to form covalent adducts with other proteases. All these proteases are also localized in different parts of the host cell. Their inhibition requires different characteristics in their inhibitors such as cellular permeability and pH sensitivity. A simple antiviral assay of a developed MPro inhibitor will likely lead to a positive result that reflects inhibition not necessarily of MPro and therefore causes misunderstanding that can be detrimental to further rounds of lead optimization. Therefore, a direct assay system that reflects MPro inhibition in host cells is crucial for assessing and optimizing MPro inhibitors. The current work will describe such a system and its application in evaluating different MPro inhibitors.

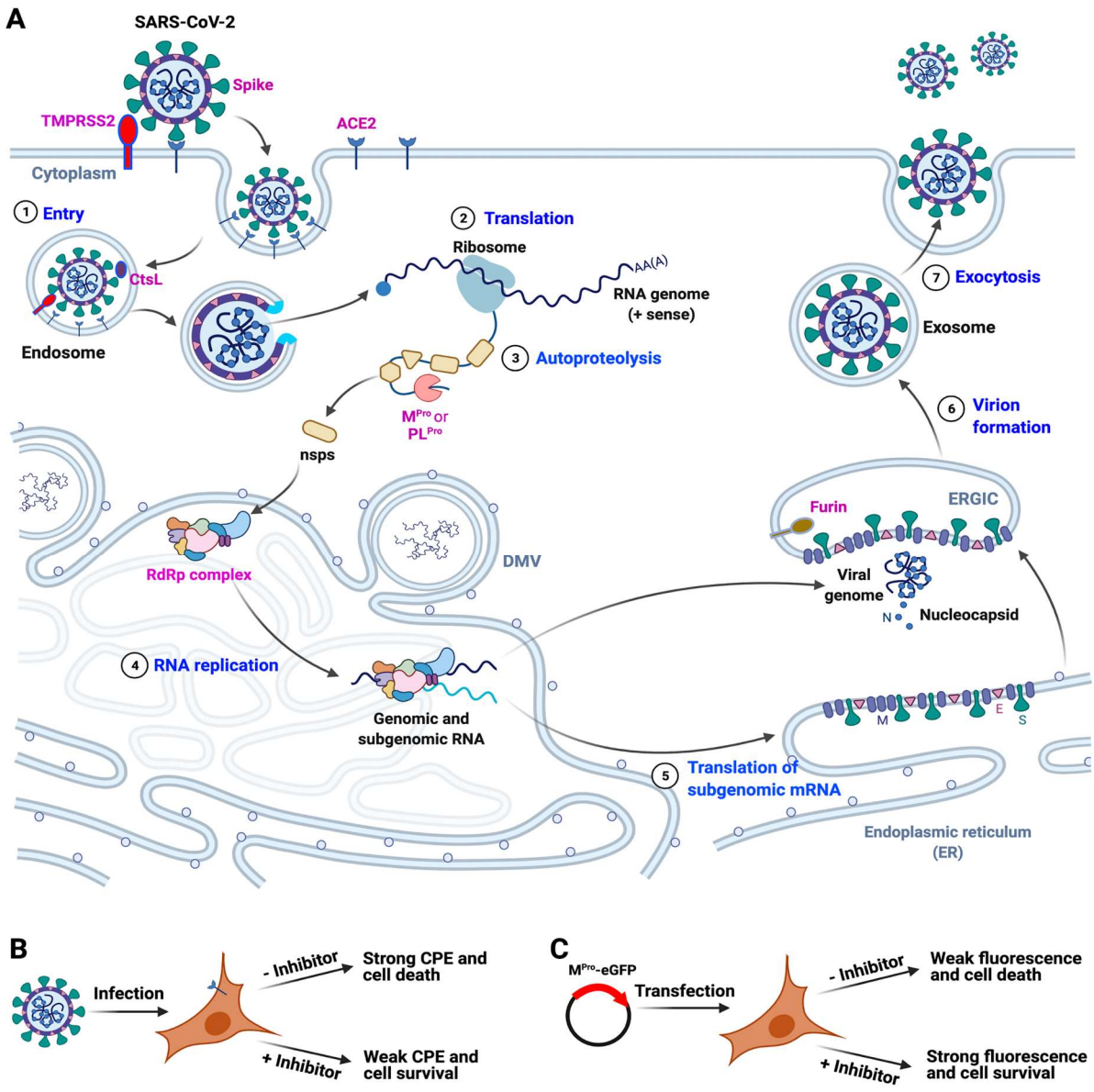

Figure 8. The life cycle of SARS-CoV-2 and two assays for M^{Pro}-targeting antivirals. (A) A cartoon diagram illustrating the life cycle of SARS-CoV-2. Seven sequential steps are labeled in blue. Proteins that are labeled in pink are targets for the development of antivirals. TMPRSS2, CtsL and furin are three host proteases that prime Spike for viral entry and new virion packaging. ACE2: angiotensin-converting enzyme 2; TMPRSS2: transmembrane protease serine 2; CtsL: cathepsin L; M^{Pro}: main protease; PL^{Pro}: papain-like protease; RdRp: RNA-dependent RNA polymerase; nsp: nonstructural protein. (B) An antiviral assay based on the inhibition of virus infection-triggered cytopathogenic effect (CPE) and cell death. (C) An antiviral assay based on the inhibition of M^{Pro}-induced apoptosis in host cells and the fluorescence of the expressed M^{Pro}-eGFP fusion protein.

RESULTS

Our group has designed, synthesized and characterized the inhibition character to SARS-CoV-2 of MPI8[119]. A fluorescent peptide assay was used to measure the IC50 value for MPIs designed and synthesized, with MPI8 giving an IC50 value of 105nM; to evaluate the real-life efficacy of these compounds of inhibiting SARS-CoV-2, a life virus based microneutralization assay was conducted in Vero E6 cells. MPI8 was giving cytopathogenic effect (CPE) at 2.5 μM, when using A549/ACE2 cells (which is better in mimicking human body environment), giving CPE at 160-310 nM. It was also studied by us that MPI8 is a potent inhibitor to Cathepsin L, which is another protease that plays important role in the life cycle of the SARS-CoV-2 virus. To study the interaction between inhibitors and SARS-CoV-2 Mpro, using a life virus-based assay may give misleading results because inhibitors designed for Mpro tend to have inhibition effect for cathepsin B, cathepsin L, etc. as well. It's also worth noticing that a live-virus based assay requires BSL-3 level biosafety laboratory, which is not equipped by any facilities. But using a cell-based assay to evaluate Mpro inhibitors is crucial: we need a cellular environment to test the viability and stability of the compound; we need the cell membrane to test the ability of the compound to get through the membrane. Thus, developing a cellular assay that is specifically targeted to Mpro is crucial.

Our first design is to use a Förster resonance energy transfer (FRET) pair to test the efficacy of the inhibitors. We tried to express the main protease with a cyan fluorescent protein (CFP) fused to the N terminal and a yellow fluorescent protein fused to the C-terminal. CFP and YFP form a Förster resonance energy transfer (FRET) pair[120]. Mpro would automatically cut off protein on its C-terminal. When added inhibitor and the bioactivity of Mpro being inhibited, the YFP on the C-terminal on this fusion protein wouldn't be cut off, resulting in FRET signals. Without inhibitor, the FRET signal would be lost. We constructed plasmid pECFP-M^{Pro}-EYFP encoding fusion

protein CFP-Mpro-YFP and tried to transfect 293T cells with this plasmid. Surprisingly this fusion protein caused cytotoxicity effect and most of the cells couldn't survive. Repeating the experiment resulted in the same result. It has been reported that Mpro would have cytotoxicity effect on human cells[121]. We then tried to transfect 293T cells using plasmid pECFP-M^{Pro}-EYFP with presence of 10 μM MPI8, resulting in cell survival and expression of the fusion protein, the fluorescence was directly detected.

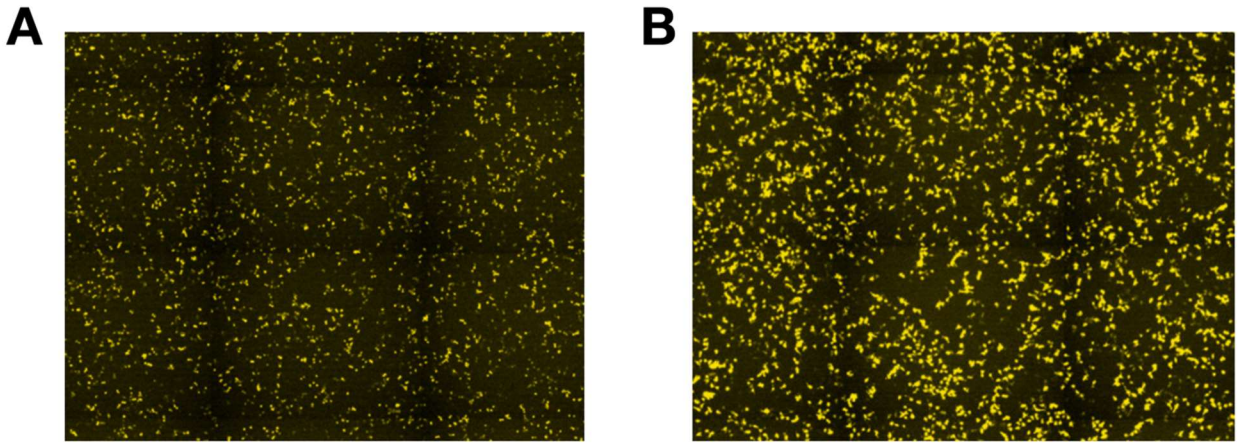

Figure 9. Yellow fluorescence from expressed CFP-M^{Pro}-YFP in 293T cells transfected with pECFP-M^{Pro}-EYFP and grown in the absence (A) or presence (B) of 10 μM MPI8.

The correlation between existence of MPI8 and expression of the fusion protein is probably that Mpro expressed its cell toxicity by interrupting the translation process. now that the main protease is inhibited, the translation process is restored, cells are healthy and able to express more fusion proteins. This correlation actually mimics the live-virus based assay to an extended level but it's very specific for the main protease. Thus, we decided to adopt this new strategy for our cell assay design.

In this design, a FRET pair is no longer needed, so we decided to label the main protease protein with enhanced green fluorescent protein (eGFP), resulting in Mpro-eGFP fusion protein. When expressed in host cells, this can be easily analyzed and quantified using flow cytometry. To prevent the green fluorescent protein being cut off from the C-terminal of the fusion protein, we

introduced a mutation Q306G to Mpro so it wouldn't automatically cleavage its C-terminal protein. MPro requires a free N-terminal serine for strong activity. To achieve this, we built two constructs as shown in Figure 10. The first construct pLVX-MPro-eGFP-1 encodes MPro-eGFP with a N-terminal methionine that relies on host methionine aminopeptidases for its cleavage. The second construct pLVX-MPro-eGFP-2 encodes MPro-eGFP containing a short N-terminal peptide that has an MPro cleavage site at the end for its autocatalytic release. Transfection of 293T cells with two constructs showed that pLVX-MPro-eGFP-2 led to more potent toxicity to cells and this toxicity was effectively suppressed when we provided 10 μM MPI8 in the growth media. Therefore, we selected pLVX-MPro-eGFP-2 for all our following studies.

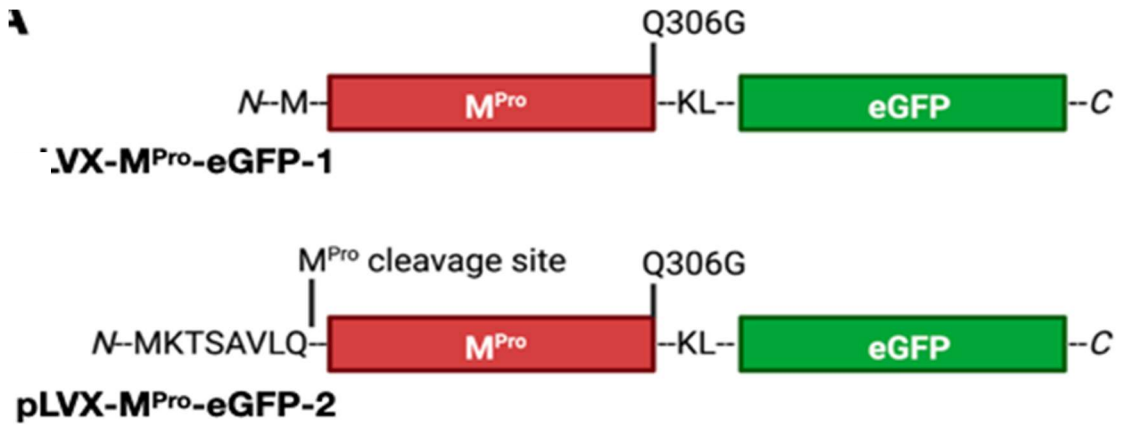

Figure 10. Plasmids constructed for Mpro-eGFP.

To test the correlation between the concentration of MPI8 and the expression level of Mpro-eGFP protein, we transfected HEK293T/17 cells with PLVX-Mpro-eGFP-2 plasmid, and then plated the cells with MPI8 at a concentration of 0, 20, 40, 160 nM. After 72h, the cells were harvested and analyzed using flow cytometry.

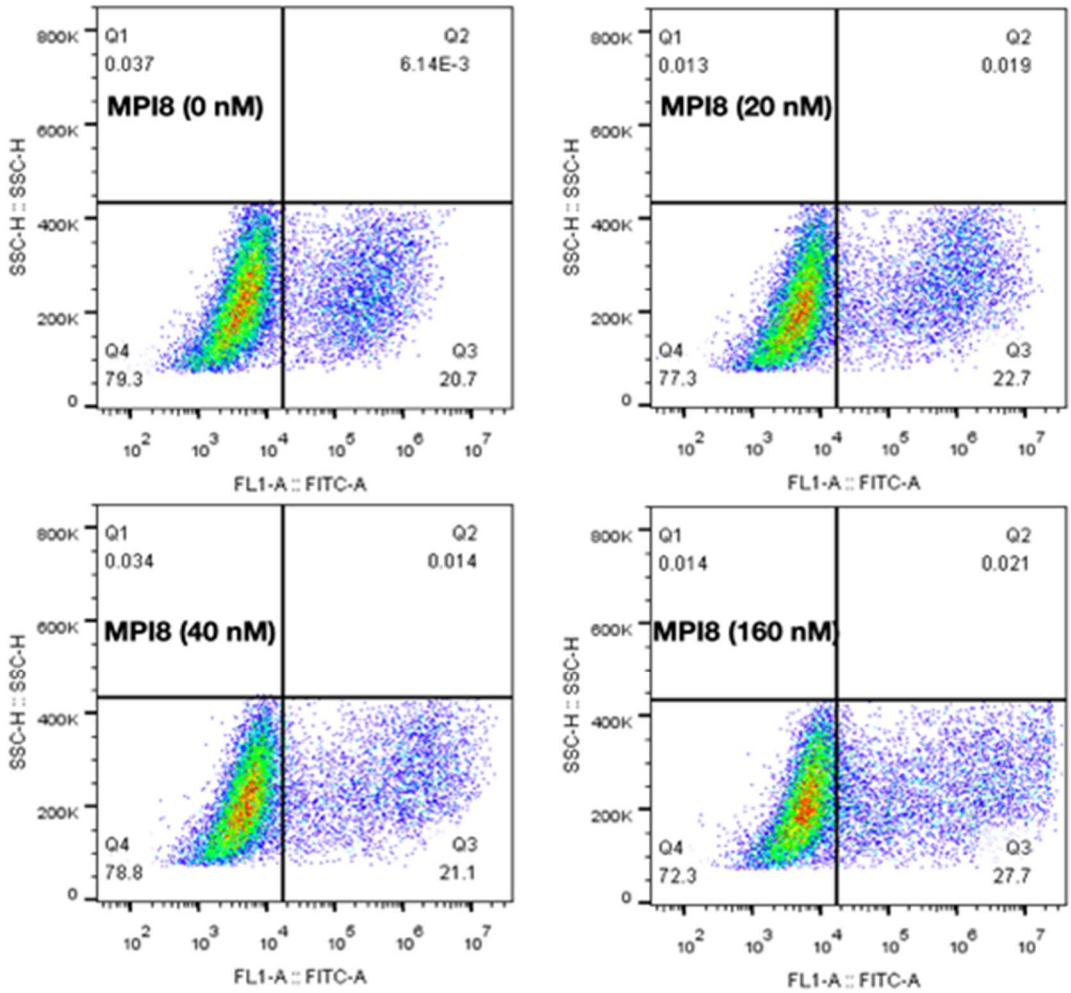

Figure 11. Flow cytometry analysis for HEK293T/17 cells incubated with different concentrations of MPI8

With higher concentration of MPI8, both cell number and green fluorescent intensity increased. To establish a mathematical relationship between the concentration and the green fluorescence intensity thus to obtain a EC50 value, a 5-fold dilution was performed with MPI8 for the transfected HEK 293T/17 cells. After 72h incubation, the cells were harvested and analyzed using flow cytometry. Cells with FL1-A signal above 1×10^6 were analyzed. We built a METLAB script to calculate average eGFP fluorescent intensity of all analyzed cells and plotted average eGFP fluorescent intensity against the MPI8 concentration as shown in Figure 12. The data showed

obvious MPI8-induced saturation of MPro-eGFP expression and fit nicely to a three-parameter dose dependent inhibition mechanism in Prism 9 for IC50 determination.

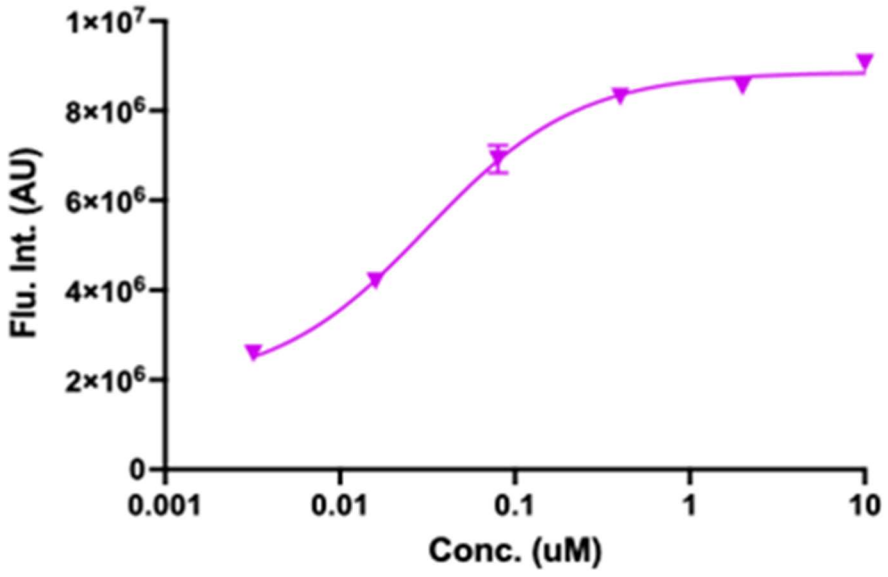

Figure 12. EC50 curve of MPI8

Now that the cellular assay system has been established, we performed a series of experiments to verify that the cell toxicity is from expression of Mpro, and an efficient Mpro inhibitor can reverse the cytotoxicity effect. First, we used an anti-annexin V labelling kit to measuring the cytotoxicity effect Mpro has on HEK 293T/17 cells. The PLVX-Mpro-eGFP-2 plasmid was used along with PMD2.G and PsPAX2 plasmids from Didier Trono lab to produce lentivirus, and then we used the virus to infect HEK293T/17 cells to afford a stable cell line that express Mpro-eGFP after a puromycin selection. This cell line was used for cell apoptosis study. We tested the cell apoptosis for HEK 293T/17 cells, HEK 293T/ cells cultured with MPI8, stable cell line, stable cell line with MPI8 and HEK293T/17 cells with antimycin A, a cell apoptosis inducer, as a positive control. Data was collected at 12, 24, 36, 48, 60, 72h respectively. The assay was repeated three times and the results were shown in Figure 13. from the assay, we can clearly tell 1 μM MPI8 doesn't induce cell apoptosis in HEK 293T/17 cells; at around 72 h, the cell

apoptosis reaches climax in the stable cell line that express Mpro-eGFP. Existence of MPI8 can either prevent or reverse the process of cell apoptosis.

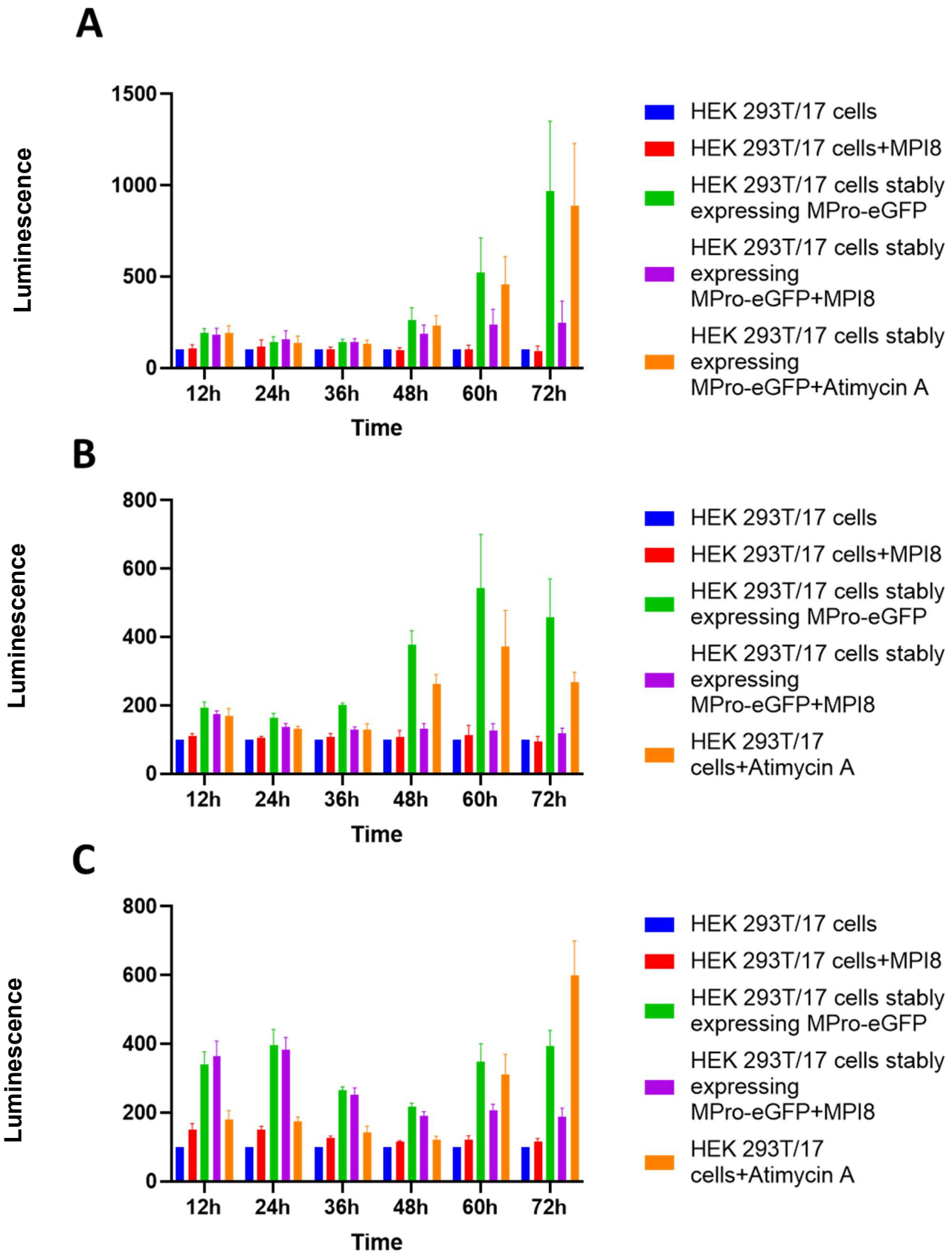
A
Luminescence
1500
1000
500
0
12h
24h
36h
48h
60h
72h
Time
HEK 293T/17 cells
HEK 293T/17 cells+MPI8
HEK 293T/17 cells stably expressing MPro-eGFP
HEK 293T/17 cells stably expressing MPro-eGFP+MPI8
HEK 293T/17 cells stably expressing MPro-eGFP+Atimycin A
B
Luminescence
800
600
400
200
0
12h
24h
36h
48h
60h
72h
Time
HEK 293T/17 cells
HEK 293T/17 cells+MPI8
HEK 293T/17 cells stably expressing MPro-eGFP
HEK 293T/17 cells stably expressing MPro-eGFP+MPI8
HEK 293T/17 cells+Atimycin A
C
Luminescence
800
600
400
200
0
12h
24h
36h
48h
60h
72h
Time
HEK 293T/17 cells
HEK 293T/17 cells+MPI8
HEK 293T/17 cells stably expressing MPro-eGFP
HEK 293T/17 cells stably expressing MPro-eGFP+MPI8
HEK 293T/17 cells+Atimycin A

Figure 13. 293T/17 cells that were established in the presence of MPI8 exhibited strong apoptosis when MPI8 was withdrawn from the growth media. The cell assay was performed with RealTime-Glo™ Annexin V Apoptosis and Necrosis Assay kit from Promega. HEK 293T/17 and constructed HEK 293T/17 cells stably expressing M^{Pro}-eGFP were used for this cell assay. The cells were maintained in high glucose DMEM medium supplemented with 10% FBS, plated with a cell density of 5×10^5 cells/mL. Five groups of experiments were set: HEK 293T/17; HEK 293T/17 + MPI8 (1 μM); HEK 293T/17 cells stably expressing M^{Pro}-eGFP; HEK 293T/17 cells stably expressing M^{Pro}-eGFP + MPI8 (1 μM); HEK 293T/17(b&c) or HEK 293T/17 cells stably expressing M^{Pro}-eGFP(a) + Antimycin A (1 μM); Each experiment has 5 repeats. The cell assay was performed as instructed by the protocol, luminescence was recorded at 12h, 24h, 36h, 48h, 60h, 72h after plating the cells. The luminescence readings were normalized using HEK 293T/17 as a negative control, which was set to a unit of 100.

Another set of apoptosis assay was performed on HEK293T/17 cells transfected with PLVX-Mpro-eGFP-2. The cells were plated with DMSO as vehicle control or 1 um MPI8, or transfected with 10/30 nm Mpro-target siRNA. The cell apoptosis was tested on 48h and 72h respectively. It is seen that the Mpro-target siRNA can very efficiently reduce cell apoptosis, even better than MPI8. The expression of Mpro is why the cells are going through cell apoptosis and

inhibition of the protease can help.

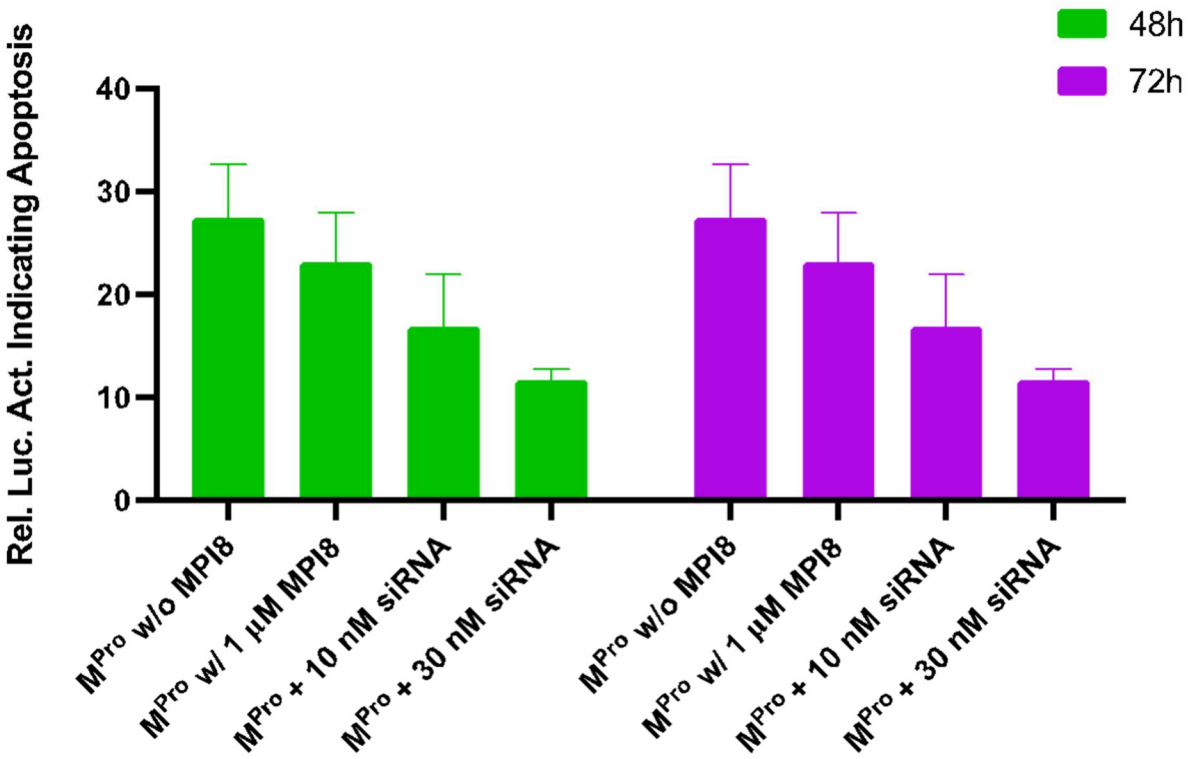

Figure 14. Cellular toxicity from MPro was inhibited by MPro-targeting siRNA. 293T cells were transiently transfected with PLVX-MPro-eGFP-2 and then incubated with or without MPI8 or MPro-targeting siRNA. SiRNA was transfected with lipofectamine 3000 (ThermoFisher L3000001), according to the protocol (ThermoFisher Document Part No. 100022234), at 24 and 48h after cells were plated respectively. After 48 and 72 h, cellular apoptosis indicating cell death was analyzed using the Promega RealTime-GloTM apoptosis assay kit.

We then tried to get some insight on why the main protease would actively induce cell apoptosis. We made a stable cell line using a plasmid that encodes Mpro(C145S)-eGFP as stated above. With the cysteine being mutated, this construct is no longer active anymore. HEK293T/17, Stable cell line that express MPro-eGFP and stable cell line that express Mpro(C145S)-eGFP were cultured with or without MPI8 and harvested at different time point, lysed and analyzed using western blot with anti-Mpro antibody.

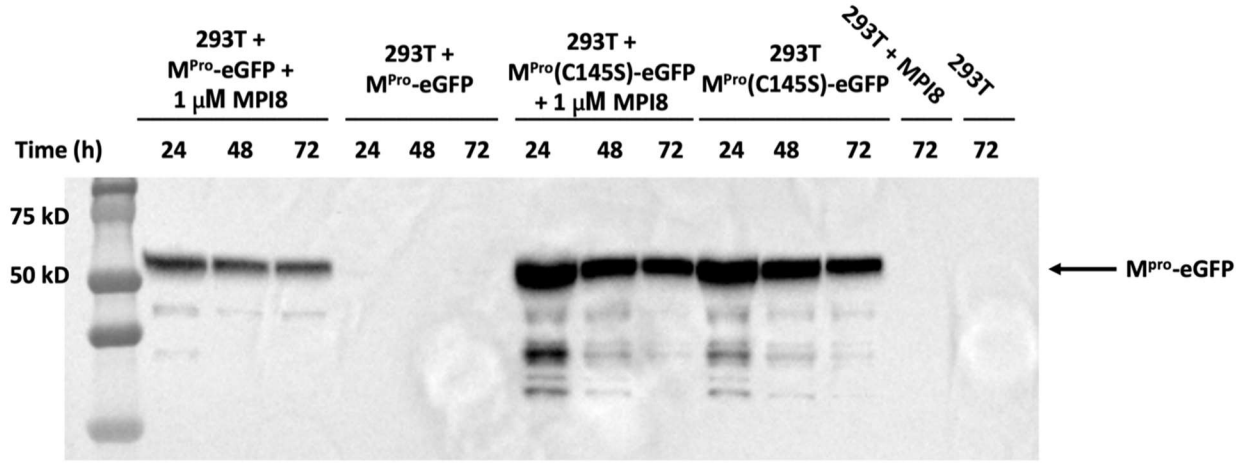

Figure 15. The cellular toxicity of M^{Pro} is from its protease activity. Cells were transfected with plasmids coding active M^{Pro}-eGFP or inactive M^{Pro}(C145S)-eGFP. Without 1 μM MPI8, the expression of M^{Pro}-eGFP led to cell death and no detectable M^{Pro}-eGFP. The addition of 1 μM MPI8 led to cell survival and detectable M^{Pro}-eGFP. However, in either presence or absence of 1 μM MPI8, cells expressing inactive M^{Pro}(C145S)-eGFP showed highly expressed M^{Pro}(C145S)-eGFP. The displayed gel was Western blotting by anti-M^{Pro}.

Determination of EC50 values for published compounds MPI1-7, MPI9, GC376, and 11a

MPI8 was one of 9 β-(*S*-2-oxopyrrolidin-3-yl)-alaninal (Opal)-based, reversible covalent M^{Pro} inhibitors MPI1-9 we previously developed. GC376 is a prodrug, when encountered with water it would release its opal component[122]. 11a was another opal-based reversible covalent Mpro inhibitor developed in 2020[112]. In our previous study, these 11 compounds showed very high potency in inhibiting Mpro with the fluorescent peptide assay, giving an IC50 value from 8.5-105nM. We have tested the EC50 value of MPI8 using the newly developed cellular assay as stated above, so we used exactly the same procedure to test the inhibition efficacy of all these Opal-based inhibitors for Mpro. At 10 μM, all molecules promoted cell survival and Mpro-eGFP expression significantly. But only MPI5, 6 and 7 induced saturated Mpro-eGFP expression under the concentrations analyzed. The determined EC50 for MPI5, 6 and 7 are 0.66, 0.12 and 0.19 μM,

respectively. MPI2-4, MPI9, GC376 and 11a have EC50 values that are higher than 2 μM while MPI1 showed an EC50 value at 10 μM.

Boceprevir, telaprevir, calpeptin, MG-132, MG-115, calpain inhibitor II, calpain inhibitor XII, and K777

Some FDA-approved and investigational medications came into researchers' view in drug repurposing researches as Mpro inhibitors. We have included HCV drugs boceprevir, telaprevir, and calpain inhibitor XII in our study. These compounds have an α-ketoamide moiety that can form a reversible covalent adduct with the active site cysteine of Mpro[117, 123, 124]. Calpeptin, MG-132 and calpain inhibitor II, these compounds have an aldehyde that can react with the cysteine reversibly. K777 is known to be a CtsL inhibitor, in live-cell based assays, it showed high potency of inhibiting SARS-CoV-2 replication as well[125]. With a vinylsulfonate moiety, it has a tendency to form permanent covalent bond with the Mpro active site cysteine, we included this molecule in our study too. As shown in Figure 17, calpeptin, MG-115, MG-132, telaprevir and K777 showed almost undetectable inhibition efficacy in our cellular assay under 10 μM. Boceprevir and calpain inhibitor II started to show inhibition for Mpro starting at 10 μM, under 2 μM, there was no inhibition. Calpeptin XII inhibitor showed the best performance in this group, but its estimated EC50 was still higher than 10 μM.

Carmofur, tideglusib, ebselen, disulfiram, and PX-12

Carmofur, tideglusib, ebselen, disulfiram and PX-12 were also included in this study from drug repurposing researches[109]. Carmofur is an antineoplastic agent, it reacts with the Mpro active site cysteine to generate a permanent thiocarbamate covalent bond. All other four compounds are redox active for covalent conjugation with the Mpro active site cysteine[126]. We used the same procedure developed for the cellular assay to test the inhibition for Mpro for these

compounds. Only PX-12 showed some inhibition effect at the concentration of 10 μM, all the other compounds tested in this group showed undetected inhibition effect under the concentration of 10 μM.

Bepridil, chloroquine, and hydroxychloroquine

Bepridil is an antianginal drug. We previously reported this compound to have high potential of inhibiting SARS-CoV-2 using computational docking analysis, the live-virus based SARS-CoV-2 inhibition assay also indicated this compound is a potent inhibitor for the virus[127]. We want to have some insight for the mechanism of this compound prohibiting the replication of the SARS-CoV-2 virus, so we included this compound in this study. A publication reported that chloroquine and hydroxychloroquine are potent inhibitors for Mpro[128], so we included these two compounds in this study too. The cellular assay was performed as stated above. Bepridil showed weak inhibition to Mpro up to a concentration of 10 μM, while chloroquine and hydroxychloroquine showed undetectable inhibition effect for Mpro. Using both a commercial and homemade substrate, we redid the enzymatic inhibition assay for chloroquine and hydroxychloroquine. Our result indicates Mpro remains 84% activity at 16 μM chloroquine and almost 100% activity at 16 μM hydroxychloroquine.

Diarylesters 10-1, 10-2, and 10-3

Benzotriazole esters were found to be potent inhibitors for SARS-CoV-1 Mpro. They were contaminants in a peptide library and were discovered accidently[129, 130]. A number of diarylesters were designed later and tested to be potent SARS-CoV-1 Mpro inhibitor based on the mechanism of the benzotriazole ester compounds inhibiting the enzyme[131, 132]. We included diarylesters 10-1, 10-2, 10-3 in this study to test whether these compounds would also inhibit SARS-CoV-2 Mpro. We performed the enzymatic assay on these three compounds and the IC50

values we got for 10-1, 10-2, 10-3 were 0.067, 0.038 and 7.6 μM respectively. We then performed the cellular assay for these three compounds. As shown in figure 17D. All three compounds started to show inhibition effect starting at the concentration at 2 and 10 μM. The EC50 of these compounds are higher than 10 μM.

The effect of CP-100356 on cellular potency of peptide-based M^{Pro} inhibitors

Mdr-1/gp is a protytical ABC transport which exports toxins from inside of the cells, it is also known as a multi-drug resistance protein, which reduces the efficacy of a lot of drug molecules in cells. CP-100356 is a high-potent inhibitor to this protein, and has been reported to help the antiviral efficacy for Mpro inhibitors[133]. We wanted to test whether this compound would help the Opal-based Mpro inhibitor we designed would be enhanced by this molecule, so we performed the cellular assay again for MPI1-9, GC376 and 11a under the presence of 0.5 μM CP-100356. In these compounds, MPI8 showed a similar inhibition curve with and without CP-100356, giving an EC50 value of 39 nM. All other Opal-based inhibitors displayed a better inhibition curve. MPI5 and MPI6 gave an EC50 value of 580 and 75 nM respectively, in the presence of CP-100356, which is slightly lower than without CP-100356. MPI7 gave an EC50 value of 75nM in the presence of CP-100356, compared to 190 nM without CP-100356, it was 60% lower. The EC50 value of MPI4, GC376 and 11a were also improved to 1.8, 2.2 and 1.4 μM respectively. However, repeating the cellular assay with the presence of CP-100356 for 10-1, 10-2, 10-3 didn't result in similar

improvement in inhibition.

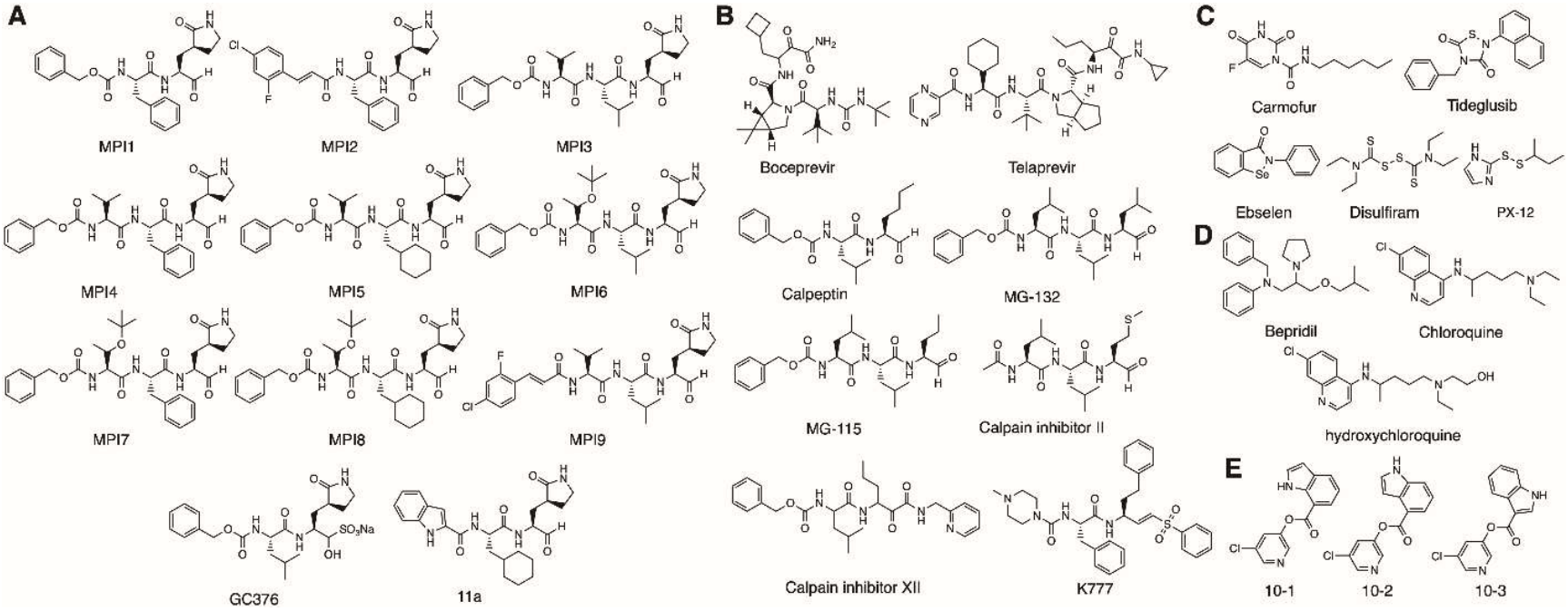

Figure 16. The structures of inhibitors that were investigated in their cellular inhibition of M^{Pro}. (A) Reversible covalent inhibitors designed for M^{Pro}. (B) Investigational covalent inhibitors that were developed for other targets. (C) Inhibitors that were identified via high-throughput screening. (D) FDA-approved medications that have been explored as M^{Pro} inhibitors. (E) Diaryl esters that have high potency to inhibit M^{Pro}.

The determination of antiviral EC_{50} values for MPI5-8

Our previous antiviral assay for Opal inhibitors were based on on-off observation of CPE in Vero E6 and ACE2+ A549 cells. To quantify antiviral EC50 values of MPI5-8, we conducted plaque reduction neutralization tests of SARS-CoV-2 in Vero E6 cells in the presence of MPI5-8. we infected Vero E6 cells with SARS-CoV-2, grew infected cells in the presence of different concentrations of each inhibitor for 3 days, and then quantified SARS-CoV-2 plaque reduction. Based on SARS-CoV-2 plaque reduction in the presence of MPI5-8, we determined antiviral EC50 values for MPI5-8 as 73, 209, 170, and 30 nM, respectively.

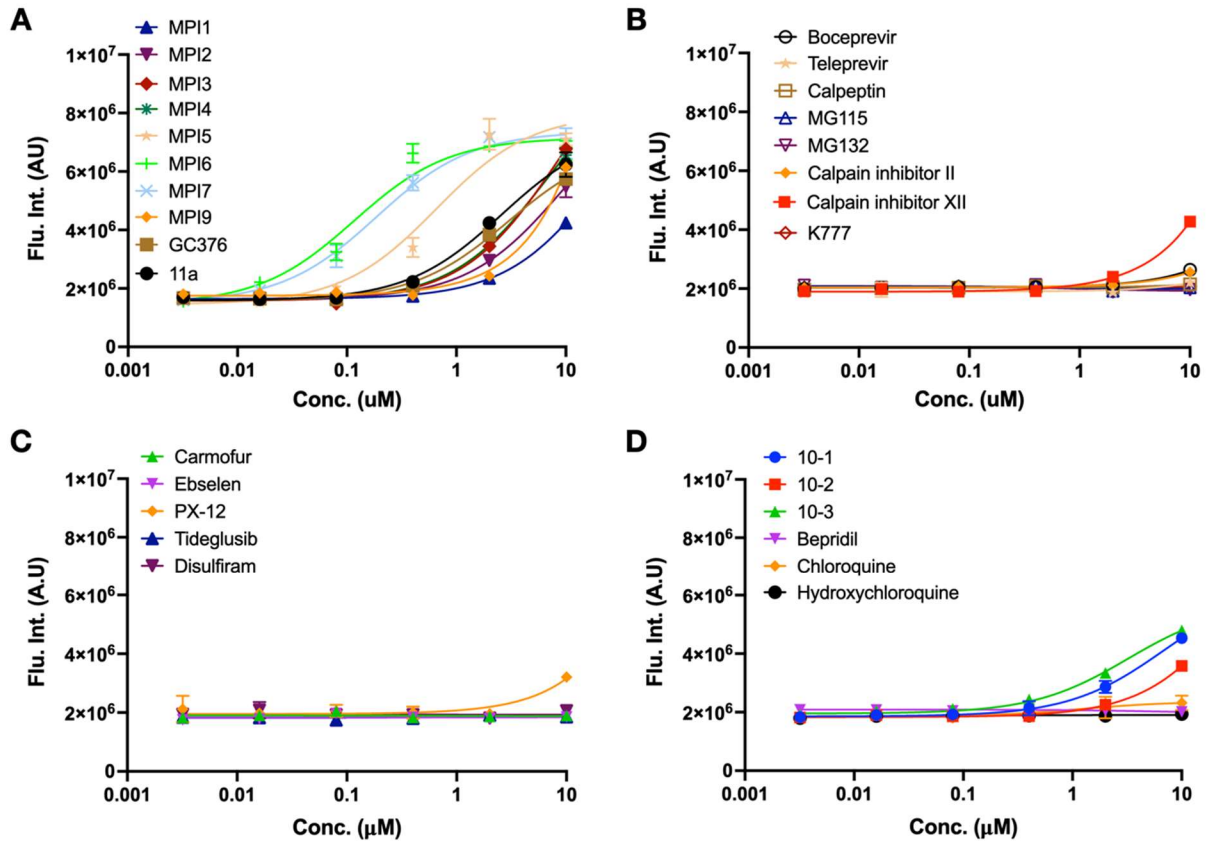

Figure 17. Cellular potency of literature reported M^{Pro} inhibitors. K777 is included as a potential M^{Pro} inhibitor.

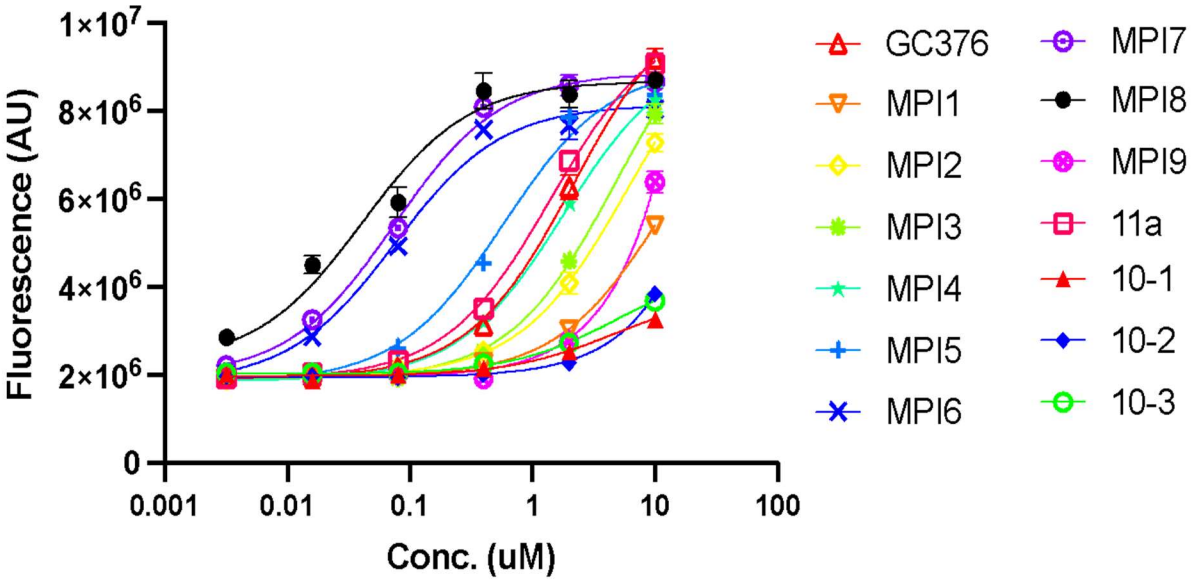

Figure 18. Cellular potency of selected compounds in their inhibition of M^{Pro} in the presence of 0.5 μM CP-100356.

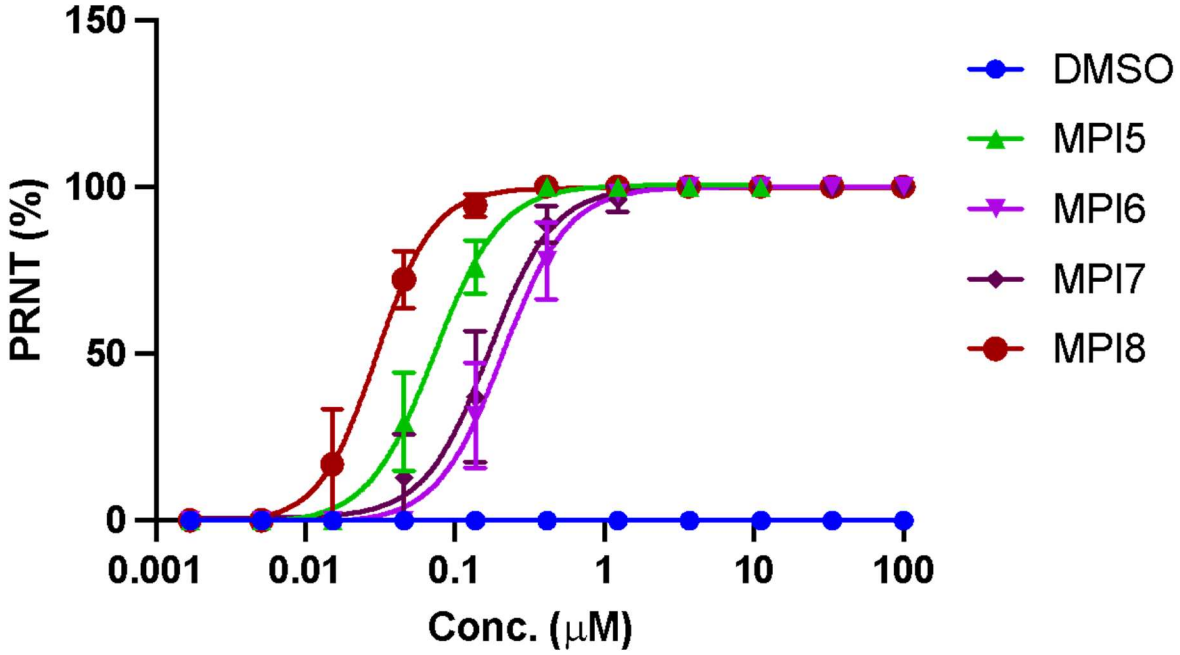

Figure 19. Plaque reduction neutralization tests (PRNTs) of MPI5-8 on their inhibition of SARS-CoV-2 in Vero E6 cells. DMSO was used as a negative control.

DISCUSSION

To replicate itself and finish its life cycle, the SARS-CoV-2 virus needs protease from both human host cells and the virus itself. It is worth noticing when developing inhibitors for these druggable targets that because these proteases share similar catalytic mechanisms, it is highly possible that an inhibitor developed for on enzyme would also inhibit one another. Therefore, a direct antiviral assay may give misleading results when used to give information for inhibitor designed for a specific enzyme. On the other hand, live-virus based assays require BSL-3 level biosafety facility to handle the virus, this very much limited the ability for researchers to perform these assays. The antiviral assay itself is time-consuming, complicated and dangerous, all of these factors limited this step to put in high throughput drug screening. To resolve these issues, we developed a cellular Mpro inhibition assay that can be easily characterized using fluorescent cell cytometry for bulk analysis of M^{Pro} inhibitors. We applied this assay to analyze 30 claimed M^{Pro} inhibitors and revealed unique features for a number of them.

We designed and previously reported MPI1-9 as efficient Mpro inhibitors[118]. Our fluorescent peptide assay gave an enzymatic IC50 value of them at all around or below 100 nM(table 1). In this group of compounds, MPI3 had the best performance in enzymatic inhibition, giving an IC50 value of 8.5 nM. However, it didn't perform very well in a CPE-based antiviral assay in Vero E6 cells. This assay showed MPI3 only weakly inhibited SARS-CoV-2. On the other hand, another compound, MPI8, which has an enzymatic IC50 value of only 105 nM, showed the best inhibition performance against SARS-CoV-2 in this group. Another antiviral assay performed in ACE2+ A549 cells showed that at around a concentration of 200 nM MPI8, the CPE caused by SARS-CoV-2 were completely inhibited. In general, the cellular Mpro inhibition potency of MPI1-9 correlates well with the antiviral potency. We quantified the antiviral effects of MPI5-8 against

SARS-Cov-2 in Vero E6 cells to analyze if the cellular potency tested agrees with the real antiviral effects. In this group of compounds, MPI5 showed a 9-fold less significant antiviral EC50 value than its cellular EC50 inhibition value, but other compounds, MPI6-8, displayed close values for both antiviral EC50 and cellular EC50s. the cellular inhibition potency tested through this newly developed assay closely matches the real antiviral assay, especially for MPI8, our determined EC50 values for the antiviral assay and cellular assay were almost identical. The difference between EC50 values obtained for MPI5 probably came from the difference in cell lines used in the assays. Being a cell line that was extracted from African monkey, it is possible that compared to HEK293T/17 cell line which was developed from human, MPI5 is more stable toward proteolytic digestion in this cell line. Upon the addition of the protytical ABC transporter inhibitor CP-100356, although most of the inhibition potency of MPIs improved, but not by very much. This indicates the low cellular and antiviral potency of MPI3 and other MPIs were not because they were transported from the inside of the cells. Possible reasons that these compounds have lower real inhibition activity might be low permeability and low stability in cells, including interactions with both extracellular and intercellular proteases. What's worth noticing in this group of compounds is MPI8, which has the highest potency of inhibiting SARS-CoV-2 in both real antiviral assay and the cellular assay. It has a cellular assay EC50 value of 31 Nm, which was lower than the determined enzymatic IC50 value. A possible reason would be accumulation of this compound in cells, which needs further study. Other MPI inhibitors with high inhibiting potency were MPI5, 6 and7, they all have an EC50 value below 1 μM. Among all the 30 compounds tested in this section, MPI5-8 displayed the best inhibiting potency toward SARS-CoV-2 Mpro.

GC376 is a medication that is going through clinical investigation of repurposing for the treatment of COVID-19 by Anivive Lifesciences Inc. It is an investigational medication for feline infectious peritonitis, a lethal coronavirus disease in cats. In our enzymatic inhibition study, GC376 displayed a relatively high potency, giving IC50 of 30 nM, but in the newly developed cellular assay, it only has weak inhibition effect. This result also agrees with the antivial potency determined from two different studies, giving an EC50 value of 3.37 and 0.7 μM, respectively[117, 124]. Like MPI3, low permeability and stability in cells may contribute to this lower cellular inhibition potency and antiviral activity. 11a is an inhibitor which performed well in the antiviral assay, giving an EC50 value of 0.53 μM[112], however, it didn't perform as well in the cellular assay. The estimated EC50 value obtained from this assay was higher than 2 μM. Although the difference between the real antiviral assay result and the cellular assay result was not massive, this still indicates that 11a might inhibit the life cycle of SARS-CoV-2 in ways other than inhibiting Mpro, which needs to be further studied.

Boceprevir and telaprevir are two antiviral drugs approved by FDA for hepatitis C virus infection. Both of them showed enzymatic activity in inhibiting Mpro. Boceprevir has also been tested in an antiviral assay, giving an EC50 value of 1.31 μM. Despite the relatively high antiviral potency, both of the compounds showed very weak inhibition activity toward s Mpro in the cellular assay. For boceprevir, there must be something other than the inhibition effect for Mpro that worked to prohibit the life cycle of SARS-CoV-2, which need to be investigated. This might inspire researchers for future drug discovery. For the other aldehyde and ketone-based inhibitors, calpeptin, MG-132, MG-115, calpain inhibitor II and calpain inhibitor XII, only calpain inhibitor XII displayed minor inhibition effect for Mpro, with an estimated EC50 higher than 10μM, others showed little to undetectable inhibition effect. In the antiviral assay, calpain inhibitor II and calpain

inhibitor XII showed antiviral effect with an EC50 value at 2.07 and 0.49 respectively, indicating that the antiviral effect of these two compounds is not contributed mainly from the inhibition of Mpro. Wang *et al.* have explored compounds with dual functions to inhibit both M^{Pro} and host calpains/cathepsins as antivirals for SARS-CoV-2[134]. Calpain inhibitor II and XII were included in this study, it is highly likely that they inhibit the host cell protease to prohibit the life cycle of the virus. K777 weakly inhibited M^{Pro} in a kinetic assay but potent inhibited SARS-CoV-2 in an antiviral assay.[135] It showed undetectable cellular M^{Pro} inhibition potency in our assay confirming that it must target other key process(es) in the SARS-CoV-2 life cycle.

Carmofur, tideglusib, ebselen, disulfiram, and PX-12 were discovered as M^{Pro} inhibitors from high-throughput screening. Carmofur reported a relatively high IC50 value in the enzymatic assay of 1.35 μM, which was expected for it would react with the active site cysteine to form a permanent thiocarbamate covalent bond, but this high inhibition effect was not observed in either the cellular assay nor the real antiviral assay. This compound showed no detectable effect in the cellular assay to a concentration up to 10 μM, this is likely because the compound is too reactive in a biological environment. Tideglusib, ebselen, disulfiram, and PX-12 are redox activity compounds that can form covalent adducts with the M^{Pro} active site cysteine. In this group of compounds, only PX-12 showed very weak inhibition effect in our cellular assay at a concentration of 10 μM, activity was not detected for other compounds. Among these four compounds, only ebselen has an available antiviral assay EC50 value at 4.67 μM. This indicates this compound works on other process other than inhibiting Mpro to stop the SARS-CoV-2 virus.

Bepridil is an antianginal drug with a demonstrated antiviral effect for SARS-CoV-2. In the enzymatic Mpro inhibition test it only showed an IC50 value at 72 μM but in the real antiviral assay performed with ACE2+ A549 cells it showed an EC50 value of 0.46 μM. Bepridil is known

to inhibit ither human pathogens as well[136]. In our cellular assay we obtained a very low potency of bepridil for inhibiting Mpro, this actually agrees with its high enzymatic IC50 value. It is worth noticing that bepridil must have a mechanism of inhibiting SARS-CoV-2 other than inhibiting Mpro. Which requires investigation. Chloroquine and hydroxychloroquine are two drugs repurposed for COVID-19 treatment. In an antiviral assay, they gave an EC50 value of 5.47 and 0.72 μM respectively[136]. A previous study stated that chloroquine and hydroxychloroquine showed inhibition effect in enzymatic assays despite that TMPRESS2 was shown to be the target of these two molecules[137]. To test whether these two compounds would inhibit Mpro, we performed our newly developed cellular assay and reperformed the enzymatic assay on these compounds. Both of the compounds showed almost undetectable inhibition effect under the concentration of 10 μM in the cellular assay; in the enzymatic assay, these compounds showed little to no inhibition effect up to a concentration of 16 μM. Our cellular data, enzymatic inhibition data and another study indicates that these two compounds don't inhibit Mpro[138]. Their inhibition effect for SARS-CoV-2 arises from other mechanism.

10-1, 10-2 and 10-3 are three diaryl esters. In the enzymatic assay, 10-1 and 10-2 showed high potency in inhibiting Mpro. Although much lower than MPI5-8, all three compounds displayed good cellular Mpro inhibition effect at the concentration of 10 μM. 10-3 didn't perform as well as 10-1 and 10-2 in the enzymatic assay, but its cellular inhibition potency was slightly higher than the latter two compounds. This may arise from the stability of the compound in cells compared to 10-1 and 10-2. When developing diaryl esters as Mpro inhibitors in the future, balancing the enzymatic activity and stability is recommended.

As a protyical ABC transporter inhibitor, CP-100356 can potentially improve intracellular accumulation of exogenous toxic molecules in cells. Addition of CP-100356 improved the

performance of all Opal-based inhibitors in the cellular assay except for MPI8, but this improvement was very limited. Among the compounds tested, MPI7 reported a highest improvement on EC50, from 0.19 μM to 0.075 μM. CP-100356 is not an approved medication, combining this drug with other medication in the treatment of COVID-19 would face very much of a limitation. Due to its nonsignificant improvement of cellular activity for an M^{Pro} inhibitor, we caution against its use. MPI8 behaved almost the same with or without the presence of CP-100356, enhancing our theory of this compound accumulating in the cell to have a better cellular inhibition effect than its enzymatic inhibition performance.

CONCLUSION

We have developed a cellular assay for the determination of cellular potency of SARS-CoV-2 M^{Pro} inhibitors. Unlike an antiviral assay in which the interference of any key step in the SARS-CoV-2 life cycle may lead to a strong antiviral effect, this new cellular assay reveals only cellular M^{Pro} inhibition potency of a compound. It provides more precise information that reflects real M^{Pro} inhibition in cells than an antiviral assay. Using this assay, we characterized 30 M^{Pro} inhibitors. Our data indicated that 11a, boceprevir, ebselen, calpain inhibitor II, calpain inhibitor XII, K777, and bepridil likely interfere with key processes other than the M^{Pro} catalysis in the SARS-CoV-2 pathogenesis and replication pathways to convene their strong antiviral effects. Our results also revealed that MPI8 has the highest cellular potency among all compounds that were tested. It has a cellular M^{Pro} inhibition IC_{50} value of 31 nM. As the compound with the highest antiviral potency with an EC_{50} value of 30 nM, we cautiously believe and recommend that MPI8 is ready for preclinical and clinical investigations for COVID-19 treatment.

Table 1: Determined enzymatic and cellular IC_{50} values in inhibiting SARS-CoV-2 M^{Pro} for different inhibitors

Compound ID	Enzymatic IC_{50} (μM)	Cellular IC_{50} (μM)	Cellular IC_{50} (μM) with CP-100356	Antiviral EC_{50} (μM)	Compound ID	Enzymatic IC_{50} (μM)	Cellular IC_{50} (μM)	Cellular IC_{50} (μM) with CP-100356	Antiviral EC_{50} (μM)
MPI1[139]	0.100 ± 0.023	> 10	> 2		MG-132[140]	3.9 ± 1.0	n.d.[c]		
MPI2[139]	0.103 ± 0.014	> 2	> 2		Calpain inhibitor II[140]	0.97 ± 0.27	> 10		[a]2.07 ± 0.76
MPI3[139]	0.0085 ± 0.0015	> 2	> 2		Calpain[10] inhibitor XII	0.45 ± 0.06	> 10		[a]0.49 ± 0.18
MPI4[139]	0.015 ± 0.005	> 2	1.8 ± 0.01		K777[135]	> 100	n.d.		[a]0.62
MPI5[139]	0.033 ± 0.002	0.66 ± 0.15	0.58 ± 0.06	0.073 ± 0.007	Carmofur[141, 142]	1.35 ± 0.04	n.d.		> 100[b]
MPI6[139]	0.060 ± 0.004	0.12 ± 0.03	0.075 ± 0.008	0.209 ± 0.022	Tideglusib[142]	1.55 ± 0.30	n.d.		
MPI7[139]	0.047 ± 0.003	0.19 ± 0.03	0.075 ± 0.006	0.170 ± 0.022	Ebselen[142]	0.67 ± 0.09	n.d.		4.67 ± 0.80[a]
MPI8[139]	0.105 ± 0.022	0.031 ± 0.002	0.039 ± 0.007	0.030 ± 0.003	Disulfiram[142]	9.35 ± 0.18	n.d.		
MPI9[139]	0.056 ± 0.014	> 2	> 2		PX-12[142]	21.4 ± 7.1	> 10[c]		
GC376	0.030 ± 0.0086[139]	> 2	2.2 ± 0.2	[a]3.37 ± 1.68[140] / 0.70[143]	Bepridil[144]	72 ± 3	n.d.		0.46[a]

11a[4]	0.053 ± 0.005	> 2	1.4 ± 0.1	0.53 ± 0.01[a]	Chloroquine[145, 146]	3.9 ± 0.2	n.d.		5.47[a]
Boceprevir	4.2 ± 0.6[140] / 8.0 ± 1.5[143]	>> 10		[a]1.31 ± 0.58[140] / 15.57[143]	Hydroxychloroquine[145, 146]	2.9 ± 0.3	n.d.		0.72[a]
Telaprevir[123]	15.3	>> 10			10-1	0.040 ± 0.004	> 10	> 10	
Calpeptin[140]	10.7 ± 2.8	n.d.			10-2	0.068 ± 0.005	> 10	> 10	
MG-115[140]	3.1 ± 1.0	n.d.[c]			10-3	5.72 ± 0.43	> 10	> 10	

[a] Primary CPE assay

[b]Genomic RNA quantification

[c]Toxic at 10 μM

n.d.: not detected

MATERIALS AND METHODS

Chemicals, reagents, and cell lines from commercial providers. We purchased HEK293T/17 cells from ATCC, DMEM with high glucose with GlutaMAX™ Supplement, fetal bovine serum, 0.25% Trypsin-EDTA, phenol red, puromycin, lipofectamine 3000, and dimethyl Sulfoxide from Thermo Fisher Scientific, linear polyethylenimine MW 25000 from Polysciences, RealTime-Glo™ annexin V apoptosis and necrosis assay kit from Promega, EndoFree plasmid DNA midi kit from Omega Bio-tek, antimycin a from Sigma Aldrich, GC376 from Selleck Chem, boceprevir, calpeptin, MG-132, telaprevir, and carmofur from MedChemExpress, ebselen from TCI, calpain inhibitors II and XII from Santa Cruz Biotechnology, MG-115 From Abcam, tideglusib, disulfiram and PX-12 from Cayman Chemical, chloroquine diphosphate from Alfa Aesar, hydroxychloroquine sulfate from Acros Organics, a fluorogenic M^{Pro} substrate DABCYL-Lys-Thr-Ser-Ala-Val-Leu-Gln-Ser-Gly-Phe-Arg-Lys-Met-Glu-EDANS from Bachem, and K777 as a gift from Prof. Thomas Meek at Texas A&M University. The synthesis of MPI1-9 and 11a were shown in a previous publication.[139]

Plasmid construction. We amplified M^{Pro} with an *N*-terminal KTSAVLQ sequence using two primers FRET-M^{pro}-for and FRET-M^{pro}-rev primers (Table S1) and cloned it into the pECFP-18aa-EYFP plasmid (Addgene, #109330) between XhoI and HindIII restriction sites to afford pECFP-M^{Pro}-EYFP. To construct pLVX-M^{Pro}-eGFP-1, we amplified M^{Pro} with an *N*-terminal methionine using primers XbaI-Mpro-f and Mpro-HindIII-r (Table S1) and eGFP using primers HindIII-eGFP-f and eGFP-NotI-r. We digested the M^{Pro} fragment using XbaI and HindIII-HF restriction enzymes and the eGFP fragment using HindIII-HF and NotI restriction enzymes. We ligated the two digested fragments together with the pLVX-EF1α-IRES-Puro vector (Takara Bio 631988) that was digested at XbaI and NotI restriction sites. To facilitate the ligation of three

fragments, we used a ratio of M^{Pro}, eGFP and pLVX-EF1α-IRES-Puro digested products as 3:3:1. We constructed pLVX-M^{Pro}-eGFP-2 in the same way as pLVX-M^{Pro}-eGFP-1 except that we amplied the M^{Pro} fragment using primers XbaI-Cut-Mpro-f and Mpro-HindIII-r (Table S1). XbaI-Cut-Mpro-f encodes an MKTSAVLQ sequence for its integration to the M^{Pro} *N*-terminus.

Transfection and MPI8 inhibition tests using pECFP-M^{Pro}-EYFP. We grew 293T cells to 60% confluency and then transfected them with pECFP-M^{Pro}-EYFP using Lipofectamine 3000. We added 10 μM MPI8 at the same time of transfection. After 72 h incubation, cells were collected and analyzed by flow cytometer as well as fluorescence microscopy. In order to obtain high-definition image, glass bottom plates were used for microimaging.

Transfection and inhibition tests using pLVX-M^{Pro}-eGFP-1 and pLVX-M^{Pro}-eGFP-2. We grew 293T cells to 60% confluency and transfected them with pLVX-MPro-eGFP-1 or pLVX- using Lipofectamine 3000. We added Different concentration of MPI8 from nM to μM level at the same time of transfection. After 72 h incubation, we analyzed the transfected 293T cells using flow cytometry to determine fluorescent cell numbers and the eGFP fluorescent intensity.

The establishment of 293T cells stably expressing M^{Pro}-eGFP. To establish a 293T cell line that stably expresses M^{Pro}-eGFP, we packaged lentivirus particles using the pLVX-M^{Pro}-eGFP-2 plasmid. Briefly, we transfected 293T cells at 90% confluency with three plasmids including pLVX-M^{Pro}-eGFP-2, pMD2.G and psPAX2 using 30 μg/mL polyethyleneimine. We collected supernatants at 48 h and 72 h after transfection separately. We concentrated and collected lentiviral particles from collected supernatant using Ultracentrifugation. We then transduced fresh 293T cells using the collected lentivirus particles. 48 h of transduction, we added puromycin the culture media to a final concentration of 2 μg/mL. We gradually raised the puromycin concentration 10

μg/mL in two weeks. The final stable cells were maintained in media containing 10 μg/mL puromycin.

Apoptosis analysis. We performed the apoptosis analysis of the M^{Pro} stable cells and cells transiently transfected with the pLVX-M^{Pro}-eGFP-2 plasmid using the RealTime-Glo™ Annexin V Apoptosis and Necrosis Assay kit from Promega. The cells were maintained in high glucose DMEM medium supplemented with 10% FBS, plated with a cell density of 5×10^5 cells/ml. We set up five groups of experiments including 1) HEK 293T/17, 2) HEK 293T/17 + MPI8 (1 μM)**,** 3) HEK 293T/17 cells stably expressing MPro-eGFP**, 4)** HEK 293T/17 cells stably expressing MPro-eGFP + MPI8 (1 μM)**, and 5)** HEK 293T/17 or HEK 293T/17 cells stably expressing MPro-eGFP + antimycin A (1 μM). Each experiment was repeated for 5 times. The assay was performed according to the instructor's protocol. Chemiluminescence was recorded at 12, 24, 36, 48, 60, and 72 h after plating the cells. The luminescence readings were normalized using HEK 293T/17 as a negative control.

Cellular M^{Pro} inhibition analysis for 29 selected compounds. We grew HEK 293T/17 cells in high-glucose DMEM with GlutaMAX Supplement and 10% fetal bovine serum in 10 cm culture plates under 37 °C and 5% CO_2 to 80%~90% and then transfected cells with the pLVX-M^{Pro}-eGFP-2 plasmid. For each transfection, we used 30 μg/mL polyethyleneimine and the total of 8 μg of the plasmid in 500 μL of the opti-MEM medium. We incubated cells with transfecting reagents for overnight. On the second day, we removed the medium, washed cells with a PBS buffer, digested them with 0.05% trypsin-EDTA, resuspended the cells in the original growth media, adjusted the cell density to 5×10^5 cells/mL, provided 500 μL of suspended cells in the growth media to each well of a 48-well plate, and then added 100 μL of a drug solution in the

growth media. These cells were then incubated under 37°C and 5% CO_2 for 72h before their flow cytometry analysis.

Data collection, processing, and analysis. The cell was incubated with various concentrations of drugs in 37 ºC for 3 days. After 3 days of incubation, we removed the media and then washed cells with 500 µL of PBS to remove dead cells. Cells were then trypsinized and spun down at 800 rpm for 5 min. We removed the supernatant and suspended the cell pellets in 200 µL of PBS. The fluorescence of each cell sample was collected by Cytoflex Beckman Flow Cytometer based on the size scatters (SSC-A and SSC-H) and forward scatter (FSC-A). We gated cells based on SSC-A and FSC-A then with SSC-A and SSC-H. The eGFP fluorescence was excited by blue laser (488 nm) and cells were collected at FITC-A (525 nm). After collecting the data, we analyzed and transferred data to csv files containing information of each cell sample. We then analyzed these files using a self-written MATLAB program for massive data processing. We sorted the FITC-A column from smallest to largest. A 10^6 cutoff was set to separate the column to two groups, larger as positive and smaller as negative. We integrated the positive group and divided the total integrated fluorescent intensity by the total positive cell counts as Flu. Int. shown in all the graphs. The standard deviation of positive fluorescence was also calculated. It was then plotted and fitted non-linearly with an agonist curve (three parameters) against drug concentrations in the program Prism 9 (from GraphPAD) for IC_{50} determination.

Kinetic recharacterization of chloroquine and hydroxychloroquine. We prepared 10 mM stock solutions of hydroxychloroquinine (HCQ) and chloroquinine (CQ) in a PBS buffer and carried out IC_{50} assays for both HCQ and CQ by measuring activities of 50 nM M^{pro} against a concentration range of 0 to 16 µM HCQ and CQ. Serial dilutions of HCQ and CQ were carried out in the assay buffer by keeping the PBS concentration same. First, 100 nM M^{pro} in assay buffer

(10 mM phosphate, 10 mM NaCl, 0.5 mM EDTA, pH 7.6) were treated with two times the working concentration of HCQ and CQ at 37 ºC for 30 minutes. Then, 20 μM of the fluorogenic M^{Pro} substrate (prepared from 1 mM stock solution of the dye in DMSO) in the assay buffer was added to the reaction mixture to a final concentration of 10 μM. Immediately after the addition of the substrate, we started to monitor the reaction in a BioTek Neo2 plate reader with an excitation wavelength at 336 nM and emission detection at 490 nM. Initial product formation slopes at the first 5 minutes were calculated by simple linear regression and data were plotted in GraphPad Prism 9.

The synthesis of 5-chloropyridin-3-yl 1H-indole-7-carboxylate (10-1)

To a solution of 5-chloropyridin-3-ol (1 mmol, 130 mg) and 1H-indole-7-carboxylic acid in anhydrous dichloromethane (DCM), we added DMAP (0.1 mmol, 12 mg) and EDC (1.2 mmol, 230 mg). The resulting solution was stirred at room temperature overnight. Then the reaction mixture was evaporated *in vacuo* and the residue was purified with flash chromatography to afford **10-1** as white solid (210 mg, 77%).

^{1}H NMR (400 MHz, DMSO-d_6) δ 11.34 (s, 1H), 8.65 (dd, J = 10.8, 2.2 Hz, 2H), 8.19 (t, J = 2.2 Hz, 1H), 8.03 – 7.92 (m, 2H), 7.47 (t, J = 2.9 Hz, 1H), 7.23 (t, J = 7.7 Hz, 1H), 6.65 (dd, J = 3.1, 1.9 Hz, 1H). ^{13}C NMR (101 MHz, DMSO) δ 164.7, 147.9, 146.1, 143.0, 134.9, 131.2, 131.0, 130.2, 128.0, 127.9, 125.3, 119.2, 111.3, 102.5. ESI-HRMS: calculated for $C_{14}H_{10}ClN_2O_2^+$: 273.0425; found: 273.0420.

The synthesis of 5-chloropyridin-3-yl 1H-indole-4-carboxylate (10-2). To a solution of 5-chloropyridin-3-ol (1 mmol, 130 mg) and 1H-indole-4-carboxylic acid in anhydrous DCM, we added DMAP (0.1 mmol, 12 mg) and EDC (1.2 mmol, 230 mg). The resulting solution was stirred

at room temperature overnight. Then the reaction mixture was evaporated *in vacuo* and the residue was purified with flash chromatography to afford **10-2** as white solid (220 mg, 80%).

^{1}H NMR (400 MHz, Chloroform-*d*) δ 8.72 (s, 1H), 8.53 (dd, *J* = 7.2, 2.2 Hz, 2H), 8.10 (dd, *J* = 7.5, 0.9 Hz, 1H), 7.75 (t, *J* = 2.2 Hz, 1H), 7.71 (dt, *J* = 8.1, 1.0 Hz, 1H), 7.43 (t, *J* = 2.9 Hz, 1H), 7.32 (t, *J* = 7.8 Hz, 1H), 7.23 (ddd, *J* = 3.2, 2.1, 0.9 Hz, 1H). ^{13}C NMR (101 MHz, $CDCl_3$) δ 165.0, 147.8, 145.7, 141.7, 136.7, 131.9, 130.0, 128.0, 127.2, 124.6, 121.3, 119.3, 117.4, 103.8. ESI-HRMS: calculated for $C_{14}H_{10}ClN_2O_2^+$: 273.0425; found: 273.0420.

The synthesis of 5-chloropyridin-3-yl 1H-indole-3-carboxylate (10-3). To a solution of 5-chloropyridin-3-ol (1 mmol, 130 mg) and 1H-indole-3-carboxylic acid in anhydrous DCM, we added DMAP (0.1 mmol, 12 mg) and EDC (1.2 mmol, 230 mg). The resulting solution was stirred at room temperature overnight. Then the reaction mixture was evaporated *in vacuo* and the residue was purified with flash chromatography to afford **10-3** as white solid (190 mg, 69%).

^{1}H NMR (400 MHz, DMSO-d_6) δ 12.27 (s, 1H), 8.58 (dd, *J* = 2.3, 1.0 Hz, 2H), 8.40 (s, 1H), 8.08 (t, *J* = 2.2 Hz, 1H), 8.06 – 8.00 (m, 1H), 7.60 – 7.51 (m, 1H), 7.31 – 7.22 (m, 2H). ^{13}C NMR (101 MHz, DMSO) δ 162.3, 148.0, 145.6, 142.8, 137.0, 135.1, 131.2, 130.8, 126.2, 123.4, 122.4, 120.8, 113.2, 104.8. ESI-HRMS: calculated for $C_{14}H_{10}ClN_2O_2^+$: 273.0425; found: 273.0420.

Kinetic characterization of 10-1, 10-2 and 10-3 in inhibiting M^{Pro}. We performed M^{Pro} inhibition assays of these compounds using with the following assay buffer: 10 mM sodium phosphate, 10 mM NaCl and 0.5 mM EDTA in pH 7.6. We diluted a stock solution of the enzyme to 200 nM with the assay buffer. Stock solutions of inhibitors were prepared in DMSO. The fluorogenic M^{Pro} substrate was diluted to 20 μM in the assay buffer. The final concentrations in the enzymatic assay were 1.25 % DMSO, 2 μM DTT, 10 μM substrate and 20 nM M^{Pro}. To perform

the assays, we mixed 39 μL of the assay buffer, 1 μL inhibitor solution (or DMSO) and 10 μL of 200 nM M^{Pro} thoroughly and then incubated the solution at 37 ºC for 30 min. The reaction was initiated by adding 50 μL of 20 μM substrate and the fluorescence intensity at 455 nm under 336 nm excitation was measured. We performed all experiments at ten different concentrations of three inhibitors in triplicate with both positive and negative controls. The initial rate was calculated according to the fluorescent intensity in the first five minutes by linear regression, which was then normalized according to the initial rate of positive and negative controls. IC_{50} curve was determined by Prism 9 from GraphPad.

Characterization of cellular potency of MPI1-9, GC376, 11a, 10-1, 10-2, and 10-3 in the presence of CP-100356. All cellular M^{Pro} inhibition assays for these fourteen compounds were repeated with the addition of CP-100356 in DMSO to a final concentration of 0.5μM. The overall assay process and analysis were identical to the assays without CP-100356.

Plaque reduction neutralization tests of SARS-CoV-2 by MPI5-8. We seeded 18×10^3 Vero cells per well in flat bottom 96 well plates in a total volume of 200 uL of a culturing medium (DMEM + 10% FBS + glutamine) and incubated cells overnight at 37 ºC and under 5 % CO_2. Next day, we titrated compounds in separate round bottom 96 well plates using the culturing medium. We then discarded the original medium used for cell culturing and replaced it with 50 ul of compound-containing media from round bottom plates. We incubated cells for 2 h at 36 ºC and under 5 % CO_2. After incubation, we added 1000 PFU/50 uL of SARS-COV-2 (USA-WA1/2020) to each well and incubated at 36 ºC and under 5% CO_2 for 1 h. After incubation, we added 100ul of overlay (1:1 of 2% methylcellulose and the culture medium) was added to each well. We incubated plates for 3 days at 36 ºC and under 5% CO_2. Staining was performed by discarding the

supernatant, fixing the plates with 4% paraformaldehyde in the PBS buffer for 30 minutes and staining with crystal violet. Plaques were then counted.

CHAPTER III

A SYSTEMATIC SURVEY OF REVERSIBLY COVALENT DIPEPTIDYL INHIBITORS OF THE SARS-CoV-2 MAIN PROTEASE

INTRODUCTION

Mpro is a cysteine protease which engages a protein substrate in P1, P2, P4 and P1' for binding with its four binding pockets S1, S2, S4 and S1'[23]. One of the components of PAXLOVID^{TM}, Nirmatrelvir, can be classified as a tripeptidyl inhibitor that uses its P1 and P2 residues and N-terminal trifuluoacetyl group to bind S1, S2 and S4 pockets, respectively, in Mpro and an activated nitrile warhead to covalently engage C145, the catalytic cysteine of Mpro (figure 20B)[44]. The P3 part of nirmatrelvir doesn't directly react with Mpro as the same as a protein substrate.

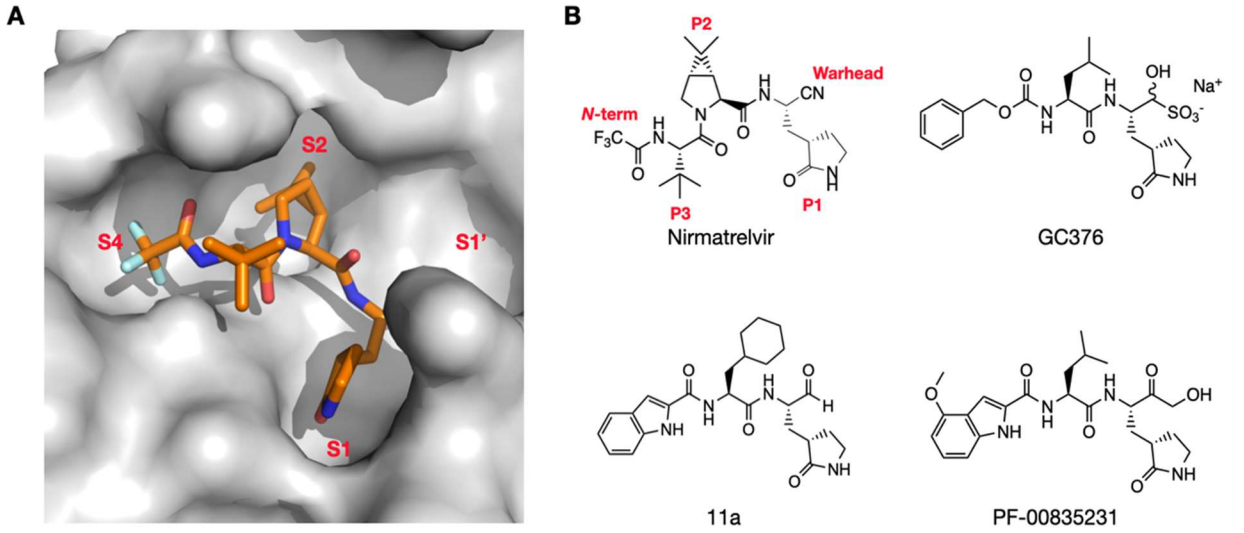

Figure 20. (A) The M^{Pro}-nirmatrelvir complex. The structure is based on the pdb entry 7TE0.[147] The contoured surface of M^{Pro} is shown. Four substrate binding pockets in M^{Pro} are labeled. (B) The structures of nirmatrelvir, GC376, 11a, and PF-00835231. Chemical positions in nirmatrelvir are labeled.

Since P3 is not necessary for an inhibitor to bind Mpro, multiple potent dipeptidyl inhibitors that uses its P1, P2 part and N-terminal residues to bind S1, S2 and S4 pockets and a

covalent warhead to bind the C145 residue of Mpro have been reported. These inhibitors include GC376, 11a and PF-00835231 (figure 20B)[124, 148-152]. However, a systematic study of dipeptidyl M^{Pro} inhibitors on how different chemical identities in P1 and P2 residues, *N*-terminal groups, and warheads influence M^{Pro} inhibition, structural aspects in binding M^{Pro}, cellular and antiviral potency, and metabolic stability has not been reported. Since we have developed the new cellular assay to test inhibition performance of small compounds for Mpro, we're going to combine this method with enzymatic inhibition assay, X-ray structure characterization to systematically study a series of inhibitors that we designed and synthesized.

RESULTS AND DISGUSSION

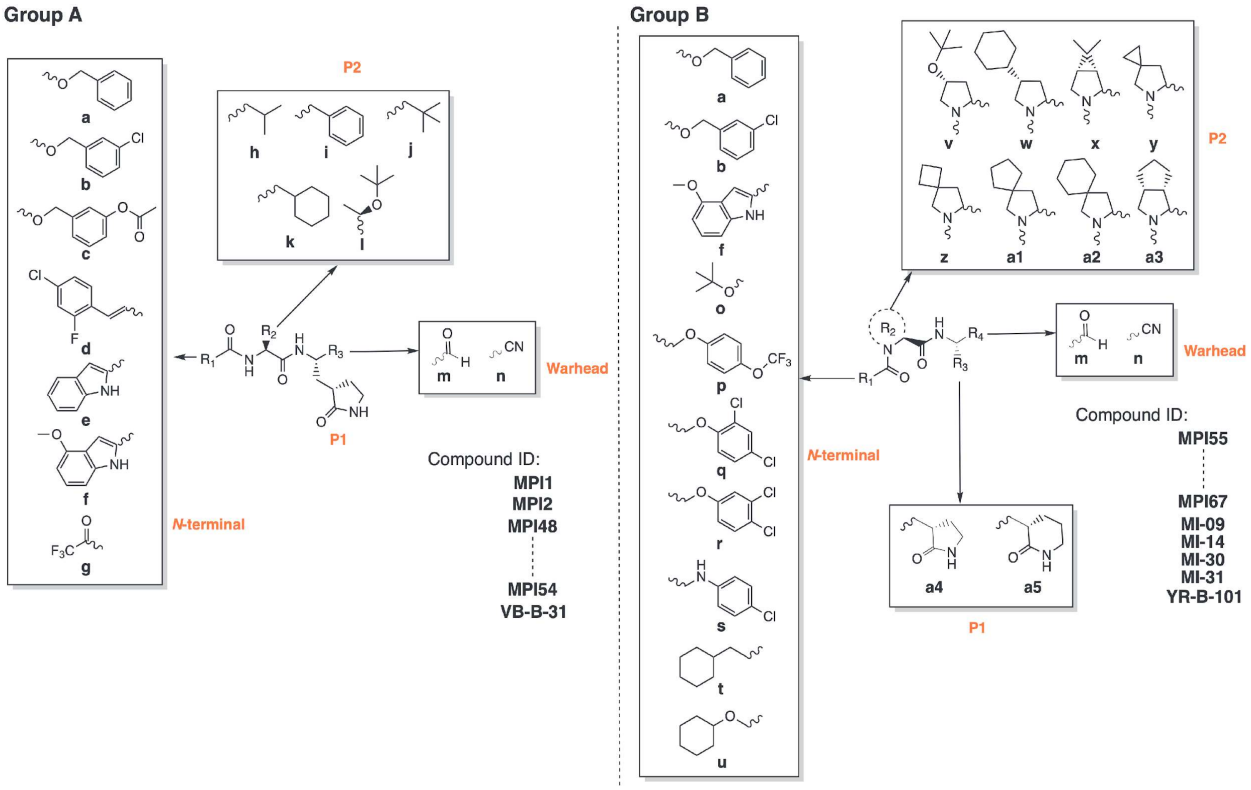

Figure 21. A diagram showing all dipeptidyl compounds that have been synthesized.

The Design and Synthesis of Dipeptidyl M^{Pro} Inhibitors.

We followed two general designs for the design and synthsis of the dipeptidyl Mpro inhibitors. As shown in figure 21. Group A compounds were designed and synthesized during the early stage of the pandemic[139]. They were primary amino-acid based and contained a 3-methylpyrrolidin-2-one side chain at the P1 site, due to its demonstrated high affinity to the S1 pocket of Mpro. Isopropyl (**h**), benzyl (**i**), *t*-butyl (**j**), and cyclohexylmethyl (**k**) were previously tested in the tripeptidyl inhibitors we developed as a side chain at the P2 site, they were included in the group A compounds[153]. Both P1 and P2 residues are in the L configuration. Our previous works show that *O*-*t*-butyl-L-threonine (**l**) as the P3 residue in tripeptidyl Mpro inhibitors resulted in high cellular and antiviral potency[139, 153], so we included this residue at the P2 site as well. We had the N-terminal groups set among carboxybenzyl (CBZ, **a**), 3-chloro-CBZ (**b**), 3-acetoxy-CBZ (**c**), 4-chloro-2-fluorocinnamoyl (**d**), 1*H*-indole-2-carbonyl (**e**), 4-methoxyl-1*H*-indole-2-carbonyl (**f**), and trifluoroacetyl (**g**). some of these groups have been observed in either SARS-CoV or SARS-CoV-2 inhibitors[109, 151, 154-159]. The warhead was chosen from either aldehyde (**m**) or nitrile (**n**) that reversely reacts with the catalytic C145 residue of Mpro to form a hemithioacetal and thioimidate, respectively.

Group B compounds were developed later, and they all have a modified proline at the P2 site. For this group of compounds, at the P1 site, they primarily have 3-methylpyrrolidin-2-one (**a4**). Some inhibitors with 3-methylpiperidin-2-one (**a5**) showed high potency, so we also included this moiety at this position[158]. Proline-based P2 residues in Group B compounds included (*R*)-3-*t*-butyloxyl-L-proline (**v**), (*R*)-3-cyclohexyl-L-proline (**w**), (1*S*, 2*S*, 5*R*)-6,6-dimethyl-3-azabicyclo[3,1,0]hexane-2-carboxylate (**x**) that is the P2 residue in nirmatrelvir, (*S*)-5-azaspiro[2,4]heptane-6-carboxylate (**y**), (*S*)-6-azaspiro[3,4]octane-7-carboxylate (**z**), (*S*)-2-azaspiro[4,4]nonane-3-carboxylate (**a1**), (*S*)-2-azaspiro[4,5]decane-3-carboxylate (**a2**), and (1*S*,

2*S*, 5*R*)-3-azabicyclo[3,3,0]octane-2-carboxylate (**a3**). A study of multiple Mpro-inhibitor complex structure showed that the peptide region aa46-51, which caps the S2 pocket, is highly flexible, as flexible as it allows the flipping of C44 to close 180° to form a Y-shaped, S-O-N-O-S-bridged crosslink with two other residues C22 and K61 in Mpro[160, 161]. This leaves a much more open, potentially large S2 pocket that would probably accommodate a large P2 residue in a dipeptidyl inhibitor. In group B, compounds with proline-based residues were designed for this reason to test how deep and bulky the S2 pocket can open to be. **V** and **W** are 3-substituted prolines, **x** and **a3** are bicyclic compounds, and **y**-**a2** are spiro compounds. They were selected for readily synthetic accessibility. The N-terminal groups for Group B compounds were more diverse than that in Group A. Besides several moieties used in Group A, other N-terminal groups included t-butyloxycarbonyl (Boc, **o**), 4-trifluoromethoxyphenoxycarbonyl (**p**), 2,4-dichlorophenoxycarbonyl (**q**), 3,4- dichlorophenoxycarbonyl (r), 4-chlorophenylcarbamoyl (**s**), 3-cyclohexylpropanoyl (**f**), and 2-cyclohexyloxyacetyl (**u**). Some of these N-terminal groups were previously used in dipeptidyl MPro inhibitors. Others were designed to explore different interactions with the S4 pocket of MPro. The warhead was chosen between aldehyde (**m**) and nitrile (**n**) as well.

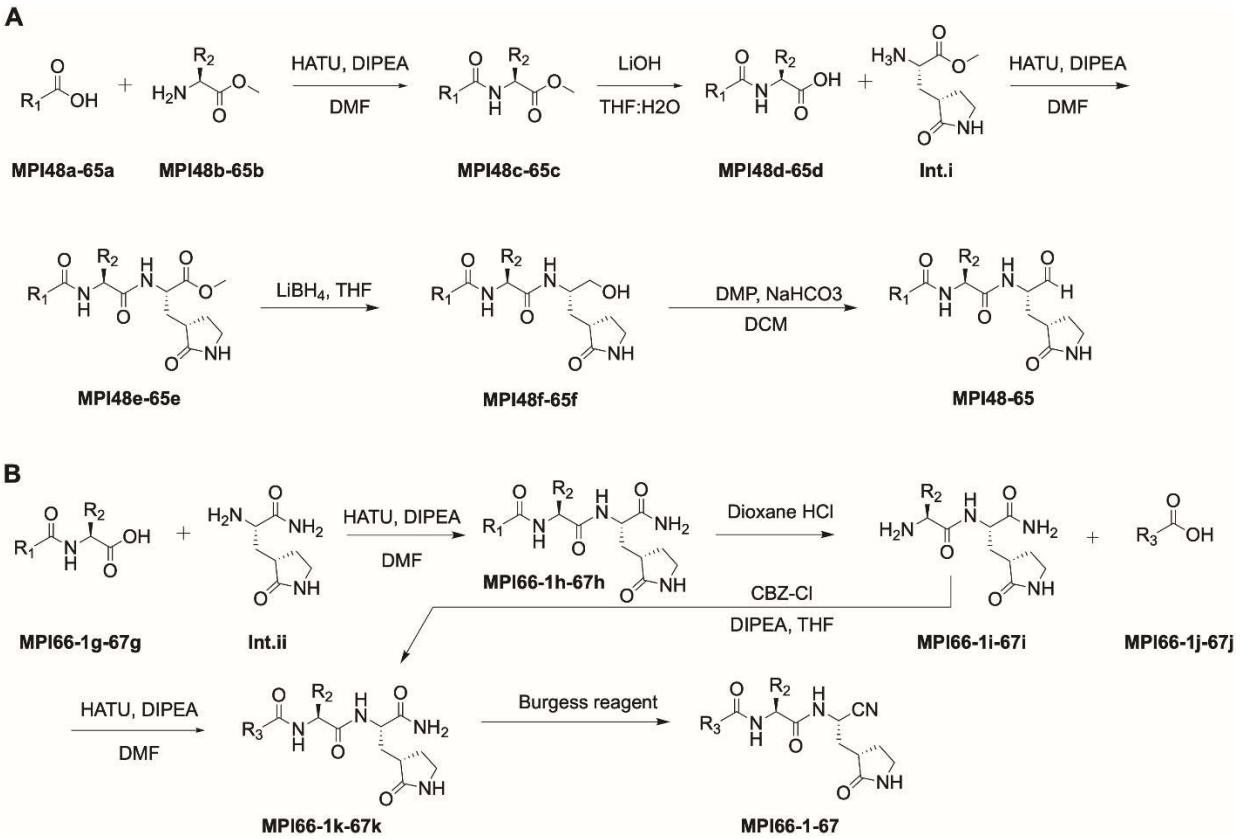

Figure 22. Synthetic routes of dipeptidyl inhibitors

To synthesize dipeptidyl MPro inhibitors, we used two synthetic routes as depicted in figure 22, resulting in the production of 29 inhibitors, including MI-09, MI-14, MI-30, and MI-31, which were developed by a different laboratory and used for comparison. Additionally, we compared the synthesized inhibitors to three previously characterized dipeptidyl MPro inhibitors: MPI1, MPI2, and GC376. Table 2 provides the compositions of all inhibitors, and their chemical structures are illustrated in Figure S8.

Table 2: M^{Pro} inhibitors, their enzymatic IC_{50}, cellular EC_{50}, antiviral EC_{50}, CC_{50},

ID	R1	R2	R3	R4	Enzymatic	Cellular EC_{50}	Antiviral	CC_{50}	CL_{int} (μL	PDB Entry
Group A										
MPI1[a]	*a*	*i*	*m*		*0.100*	*> 10*				*7JPZ*
MPI2[a]	*d*	*i*	*m*		*0.103*	*> 2*				

GC376[a]	*a*	*h*	*m*		*0.030*	*> 2*				*7C6U*
11a	*e*	*k*	*m*		*0.053*	*0.66*				*6LZE*
MPI48	e	j	m		0.029	1.6				7SD9
MPI49	f	j	m		0.074	0.91	1.3			7SDA
MPI50	a	j	m		0.053	0.73	0.75			
MPI51	a	k	m		0.056	0.77	6.7			
MPI52	b	k	m		0.11	0.59	2.6			
MPI53	c	k	m		0.098	3.50				
MPI54	a	l	m		0.40	> 10				
VB-B-31	g	k	n		> 2					
Group B										
MPI55	a	v	a4	m	0.56					
MPI56	a	w	a4	m	0.51					
MPI57	a	x	a4	m	0.025	1.1	1.5			
MPI58	a	y	a4	m	0.025	0.66	3.6			
MPI59	a	z	a4	m	0.030	0.43	0.56			
MPI60	a	a1	a4	m	0.022	0.088	0.37	95	11	
MPI61	a	a2	a4	m	0.049	0.085	0.37	230	45	
MI-09[b]	p	x	a4	m	0.055	0.27				7SDC
MI-14[b]	q	x	a4	m	0.028	0.28				
MI-30[b]	q	a3	a4	m	0.040	0.65				
MI-31[b]	r	a3	a4	m	0.042	2.7				
YR-B-101	o	z	a4	m	> 5					
MPI62	s	x	a4	m	0.99					
MPI63	q	y	a4	m	0.039	2.9				
MPI64	u	x	a4	m	0.025	3.6				
MPI65	t	x	a4	m	0.041	0.56	0.96			
MPI66-1	a	a1	a4	n	2.2					
MPI66-2	b	a1	a4	n	3.6					
MPI66-3	f	a1	a4	m	1.5					
MPI66-4	f	a1	a5	n	6.0					
MPI67	a	a2	a4	n	1.4					

[a]Data were taken from Cao *et al.[162]*

[b]Rechracterized compounds from Qiao *et al.[156]*

The Enzymatic Inhibition Potency of Dipeptidyl M^{Pro} Inhibitors.

Like in chapter II, the enzymatic inhibition potency was firstly tested.

To determine the IC50 values for our synthesized compounds, we used the established Sub3 (Dabcyl-KTSAVLQSGFRKME-Edans) fluorogenic peptide substrate of MPro, following a previously established protocol[163]. We incubated MPro with varying concentrations of each compound for 30 minutes before adding Sub3, and then recorded and analyzed the resulting fluorescent product formation (Ex: 336 nm/Em: 455 nm) to determine the IC50 values. This 30-minute incubation time is a standard procedure used by multiple labs for determining IC50 values for MPro inhibitors[152, 164], and since all of our synthesized compounds are reversible covalent inhibitors, we don't expect the incubation time to significantly affect their determined IC50 values. This has been previously confirmed by a test of a reversible covalent inhibitor at different incubation times (15, 30, and 60 minutes), which resulted in very similar IC50 values. The obtained IC50 values for all compounds are presented in table 2 and all inhibition curves are shown in figure 23. for group A compounds, all of them displayed an IC50 value around or lower than 100nM except for MPI54 and VB-B-31, which is comparable to MPI1, MPI2 and GC376. MPI54 has *O*-*t*-butyl-threonine at the P2 site. It is known that the S2 pocket of Mpro prefers leucine, phenylalanine and their analogs at their P2 site of substrates and inhibitors, so the installation of an *O*-*t*-butyl-threonine resulted in weaker binding is not surprising. However, the *O*-*t*-butyl-threonine moiety didn't significantly distort the binding between MPI54 and Mpro compared MPI1, this is very intriguing, giving the fact that *O*-*t*-butyl-threonine is structurally very different with leucine and phenylalanine. This indicates the S2 pocket could potentially accommodate a large variety of structurally unique and bulky groups which resulted in the design of group B. VB-B-31 has a nitrile warhead and a small N-terminal group. We know that the nitrile warhead reacts to the catalytic C145 very efficiently, so the relatively low inhibition efficiency may arise from the small N-terminal trifluoroacetyl group failing to interact with the S4 pocket. MPI1, GC376, MPI50

and MPI51 differ only at a P2 site with a leucine, phenylalanine, or analog. Their similar IC50 values indicating that the Mpro S2 pocket has similar affinity with a leucine, phenylalanine, or their derivatives. MPI48, MPI49, and MPI50 differ at the *N*-terminal group and have similar IC_{50} values. Compared to CBZ (**a**), 1*H*-indole-2-carbonyl (**e**) and 4-methoxyl-1*H*-indole-2-carbonyl (**f**) are more structurally rigid. Previous works have already shown that these three groups involve different interactions with M^{Pro}.[33, 143] it might be accidental that they contributed to similar binding toward Mpro binding. MPI51, MPI52 and MPI53 are similar in structure. MPI52 and MPI53 have a 3-chloro and 3-acetoxy group on the N-terminal respectively, they didn't significantly alter the inhibition effect to Mpro. The structures of MPro complexed with dipeptidyl inhibitors that have been previously determined showed a loosely bound N-terminal CBZ. This weak binding of CBZ to MPro might explain why substituting CBZ has a relatively weak effect on binding to MPro, and this information is not particularly useful in designing more potent inhibitors. However, it is helpful in designing metabolically stable compounds since adding substitutions to CBZ can significantly alter its metabolic stability.

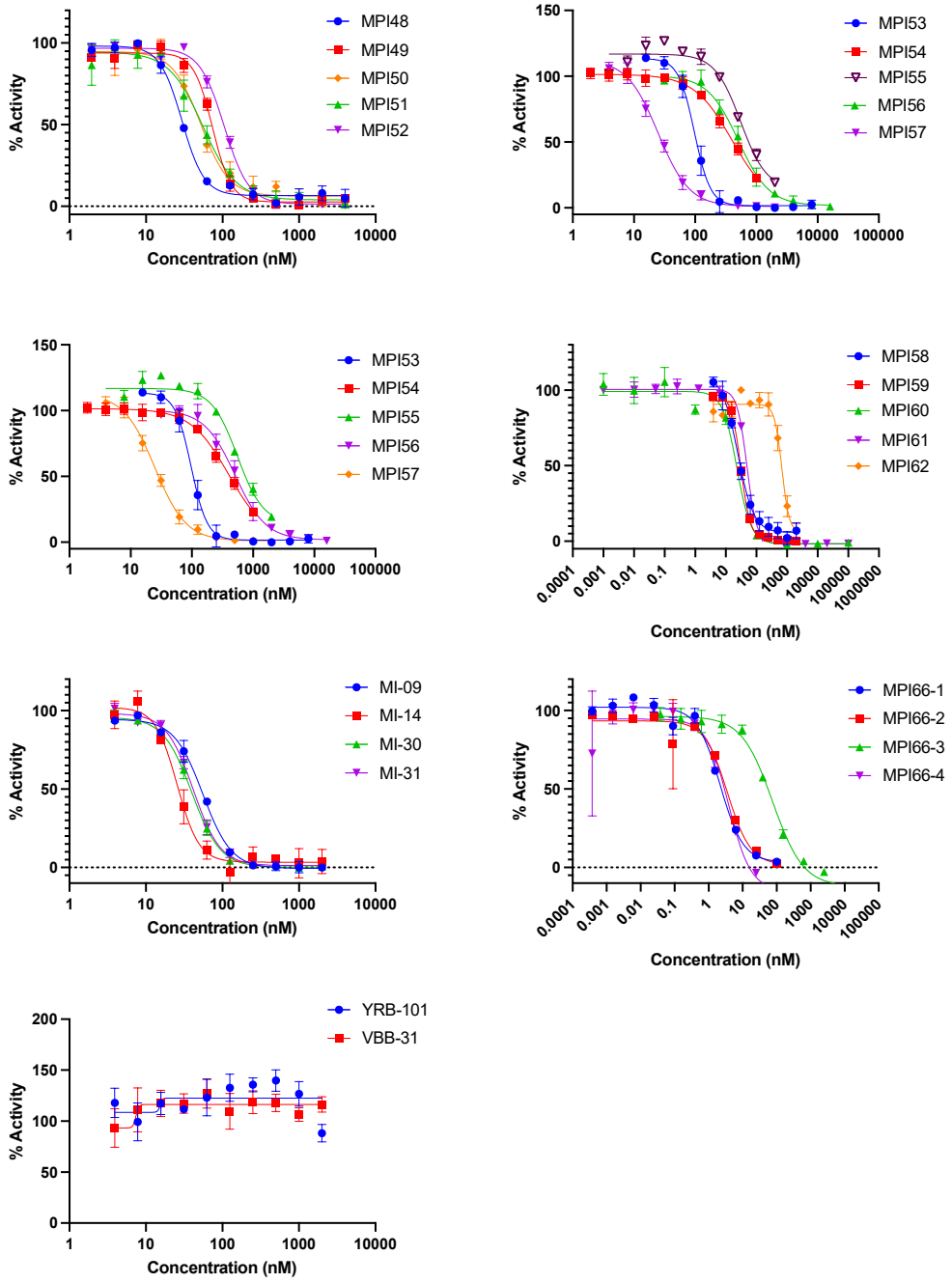

Figure 23. Inhibition curves of compounds on M^{Pro}. Triplicate experiments were performed for each compound. For all experiments, 20 or 10 nM M^{Pro} was incubated with an inhibitor for 30 min before 10 µM Sub3 was added. The M^{Pro}-catalyzed Sub3 hydrolysis rate was determined by measuring linear increase of product fluorescence (Ex: 336 nm/Em: 455 nm) for 5 min.

Based on information gathered from group A compounds and other developments by exploring bicyclic side chains in the P2 residue of M^{Pro} inhibitors such as nirmatrelvir, MI-09, MI-14, and MPI29-MPI47, we designed and synthesized group B compounds. MPI55 and MPI56 has a large 3-substitution at its P2 proline. For MPI56, the P2 (*R*)-4-cyclohexyl-L-proline (**w**) is also highly rigid. Both inhibitors showed only mild inhibition efficiency, even though, compared to other inhibitors, they have an IC50 value a little higher than MPI54, which is around 0.5 μM, this still indicates they can bind Mpro efficiently. (*R*)-4-cyclohexyl-L-proline (**w**) might be the largest P2 residue that has been tested so far. The S2 pocket can adjust itself for bulky P2 residue, which agrees with the findings of the crystal structures mentioned above. Therefore, it's possible to develop large but strong Mpro binding P2 residues. This potential needs further exploration. MPI57-61 are structurally similar, with variations in their P2 sites. They all have a *N*-terminal CBZ (**a**), P1 3-methylpyrrolidin-2-one side chain, and aldehyde warhead. Their P2 side chain varied among bicyclic and spiro moieties **x-a2**. In the inhibition assay, all five compounds obtained very low IC50 values below 50nM. MPI57-60 have an IC50 value at or below 30nM, while MPI60 has the lowest IC50 as 22 in all the compounds in this series. In terms of structure, **w-a2** can be seen as analogues of leucine and phenylalanine that have greater structural stability due to the formation of a proline ring. This greater stability probably contributes to the strong binding of these components to the MPro pocket. We increased the size of the P2 side chain from MPI57 to MPI61. This didn't change the IC50 value among these compounds by much, which confirmed the high structural flexibility of the Mpro S2 pocket. MI-09, MI-14, MI-30, and MI-31 are four previously reported dipeptidyl M^{Pro} inhibitors.[156] we synthesized and tested them to compare them with all the other dipeptidyl Mpro inhibitors. They reported an IC50 value around or below 50 nM. MI-09 and M1-14 have the same P2 **x** residue but they have two different N-terminal groups **p** and **q**,

respectively. The compounds MI-09 and MI-14 bear similarities to MPI57 in terms of structure, with the exception of the N-terminal carbamate oxygen being shifted by one position and extra group(s) added to the N-terminal phenyl group. Despite these differences, both MI-09 and MI-14 have similar, albeit slightly higher, IC50 values compared to MPI57. This may arise from the relatively loosely bound N-terminal CBZ like group to Mpro. MI-30 and MI-31 both feature a P2 **a3** residue, with **q** and **r** being their N-terminal groups, respectively. They have IC50 values that are comparable to other compounds that have a bicyclic or spiro residue at the P2 site. This is likely due to the fact that the size of **a3** is similar to **x**. A compound, YR-B-101, that resembles MPI59 in structure but with a N-terminal BOC (**o**) group was synthesized. This compound, however, showed very limited inhibitory potency against Mpro. With the goal of replicating the strong binding of compound 11a to MPro, which is believed to be due to the hydrogen bond formed by the N-terminal indole imine and the backbone carbonyl oxygen of E66 in MPro, we attempted to achieve this interaction by incorporating s as the N-terminal group for MPI62, a compound similar in structure to MPI57, MI-09, and MI-14. Unfortunately, the IC50 value obtained was significantly higher than the values for the other three compounds. There are two possible reasons for this decrease in affinity. Firstly, the addition of a hydrogen bond donor may make the molecule more soluble in water. Secondly, the proposed hydrogen bond may not form as effectively as anticipated. Since MI-14, which has an N-terminal **q** group, showed a lower IC50 value compared to MI-09, the **q** moiety was incorporated into MPI58 to create MPI63. However, this resulted in a higher IC50 value compared to MPI58. The data collected thus far suggests that the CBZ (**a**) group is the most effective N-terminal group for creating high potency dipeptidyl MPro inhibitors. Since the N-terminal CBZ (**a**) group only has a weak binding to MPro, we hypothesized that replacing it with **t** and **u**, which have a saturated cyclohexane, might result in stronger interactions with

MPro. By replacing the CBZ (**a**) group in MPI57 with **u** and **t**, MPI64 and MPI65 were produced, respectively. The IC50 value of MPI64 was found to be the same as MPI57, while MPI65 showed a slightly higher IC50 value. Although the use of t and u did not result in more potent inhibitors, the results indicate that N-terminal groups other than CBZ (**a**) can still produce equal inhibition potency against Mpro. Based on all the compounds discussed, the optimal P2 residues are two primary amino acids **h** and **j**, as well as all the tested bicyclic and spiro amino acids **x-a3**. Despite the fact that they all showed similar enzymatic inhibition potency, it is difficult to determine which one is the best. However, MPI60, which has a P2 **a1** residue, has the lowest IC50 value among all the tested compounds.

Previous studies on tripeptidyl and dipeptidyl MPro inhibitors showed that even if the aldehyde (**m**) warhead is replaced with nitrile (**n**), potent inhibitors can still be obtained. To test this, two new compounds were synthesized: MPI66-1, which contained the nitrile (**n**) warhead and was structurally different from MPI60 only in this aspect, and MPI66-2, which had an additional 3-chloro group added to the N-terminal group. The potency of both compounds was found to be much weaker than that of MPI60, with an IC50 value higher than 2 μM. It is possible that **a2** at the P2 site introduces unique M^{Pro}-inhibitor interactions that makes the covalent interaction between M^{Pro} C145 and nitrile (**n**) less favorable than that in the M^{Pro}-nirmatrelvir complex. we tried to replicate the strong binding observed in the MPro-11a complex by replacing the N-terminal CBZ (**a**) group in MPI60 with f to form MPI66-3, this attempt was unsuccessful. The IC50 value of MPI66-3 was determined to be above 1 μM, a significant increase compared to that of 11a. This finding supports the hypothesis that the **a2** group at the P2 site creates specific interactions with MPro. An earlier study revealed that a dipeptidyl inhibitor with a 3-methylpiperidin-2-one (**a5**) side chain was more potent in terms of enzymatic inhibition compared to its 3-methylpyrrolidin-

2-one (**a4**) counterpart. In an attempt to restore the effectiveness of MPI66-1, the P1 a4 residue was swapped with a5 to form MPI66-4. However, this change resulted in even lower inhibitory potency, with an IC50 value of 6.0 μM. As will be discussed further, MPI61, which has an **a2** group at its P2 site, demonstrated strong cellular and antiviral potency. Taking these results into account, we synthesized MPI67, a version of MPI61 that contained a nitrile (**b**) group. Unfortunately, MPI67 displayed poor enzymatic inhibition potency with an IC50 value of 1.4 μM. Our series of dipeptidyl MPro inhibitors indicated that the aldehyde (**m**) warhead was more effective than the nitrile (**n**) warhead in producing high enzymatic inhibition potency in dipeptidyl MPro inhibitors.

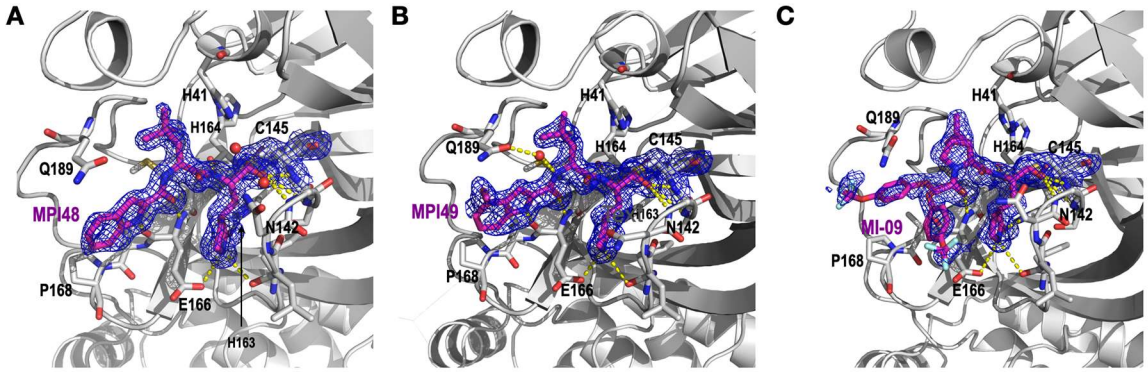

Figure 24. The crystal structures of (A) M^{Pro}-MPI48, (B) M^{Pro}-MPI49, and (C) M^{Pro}-MI-09. The 2fo-fc maps around the inhibitor and C145 in all three structures were contoured at 1σ.

X-Ray Crystallography Analysis of M^{Pro} bound with MPI48, MPI49, and MI-09.

Previously, we obtained the crystal structure of MPro in complex with MPI1, as reported in PDB entry 7JPZ. In this structure, the electron density around the N-terminal CBZ (**a**) group of MPI1 was not well-defined. As the N-terminal group of MPI1 is similar to that found in most Group A compounds, and previous studies have characterized peptidyl MPro inhibitors with various primary amino acid residues at the P2 site, we decided to perform X-ray crystallography analysis on MPro complexed with MPI48 and MPI49, both of which belong to Group A and have

N-terminal groups that differ from CBZ. To perform the X-ray crystallography analysis of MPro complexed with MPI48 and MPI49, we followed a procedure that had been established previously. First, we obtained crystals of the apo form of MPro, and then soaked these crystals with MPI48 or MPI49. The crystals were then mounted on an X-ray diffractometer for data collection, and the collected data were used to refine the structures of MPro bound with MPI48 and MPI49, respectively. The structure of MPro-MPI48 was determined at a resolution of 1.85 Å. As depicted in Figure 24A, the electron density at the active site of MPro-MPI48 was clearly defined, enabling the unambiguous refinement of all non-hydrogen atoms of the bound inhibitor. In the structure of MPro-MPI48, the three methyl groups of the P2 t-butyl group were clearly visible, and there was a continuous electron density that connected the thiolate of MPro C145 with the P1 Cα atom of MPI48, indicating the formation of a covalent bond. The electron density surrounding the P1 Cα of MPI48 enabled the refinement of a hemithioacetal hydroxyl group, which was in a strictly S conformation and pointed directly at the anion hole. This hydroxyl group was positioned with a hydrogen bond distance to three backbone α-amines from MPro residues G143, S144, and C145. The strict S conformation of the hemithioacetal hydroxyl group has been observed in MPro bound with other aldehyde-based inhibitors as well. the lactam side chain at the P1 site formed a hydrogen bond with the H163 imidazole nitrogen and two hydrogen bonds with the E166 side chain carboxylate and the F140 backbone α-amide oxygen using its amide oxygen and nitrogen, respectively. The P1 α-amine also formed a hydrogen bond with the H164 backbone α-amide oxygen. The P2 t-butyl group fit well into the S2 pocket and was in close proximity to the side chains of H41, M165, and E189. M49 is a residue in the aa45-51 region that caps the S2 pocket. Its side chain was observed to fold into the S2 pocket in apo-MPro but typically flipped its position to open the S2 pocket to bind a peptidyl inhibitor. In determined MPro-inhibitor complexes that

were co-crystalized and had a closed active site due to protein packing in crystals, the M49 side chain was usually observed to cap the S2 pocket. The MPro crystals we acquired possessed an active site that was open, thereby enabling structural modifications in the vicinity of the active site. Nevertheless, attempts to immerse them in peptidyl inhibitors consistently resulted in a malleable aa45-51 region whose structure could not be properly resolved. In the case of MPro-MPI48, the structure of the aa45-51 region could not be refined due to the absence of strong electron density, which indicates a high degree of structural flexibility. MPI48, which has an N-terminal 1H-indole-2-carbonyl (e) group, utilized its carbonyl oxygen and indole nitrogen to establish a hydrogen bond with the E166 α-amine and α-carbonyl oxygen, respectively. The hydrogen bond between the MPI48 indole nitrogen and the E166 α-carbonyl oxygen is exclusive to MPI48 and other dipeptidyl inhibitors with an N-terminal 1H-indole-2-carbonyl (e) group or analog. The presence of a similar hydrogen bond has also been detected in MPro that is bound to other comparable dipeptidyl inhibitors, like 11a. The structure of the MPro-MPI49 complex was refined to a resolution of 1.85 Å, as illustrated in Figure 3B. The electron density at the active site allowed the refinement of the chemical compositions of MPI49, except for the O-methyl moiety of its N-terminal group, which could not be defined due to the absence of interactions with MPro that could have stabilized its configuration. MPI49 exhibited covalent interactions and other types of interactions with MPro, which were mostly similar to those observed in the MPro-MPI48 complex. In addition, a new hydrogen bond was detected in the MPro-MPI49 complex between the P2 α-amine and a water molecule. This water molecule was also positioned within hydrogen bond distance of the Q189 side chain amide.

The majority of Group B compounds share a similar structure. To conduct structural characterization, we selected MI-09 as a representative due to its high potency. MI-09 was a

compound that had been previously published for its antiviral efficacy in mice. However, the structure of its complex with MPro was not previously reported. We employed our established soaking method to determine and refine the structure of MPro complexed with MI-09 to a resolution of 1.85 Å. As depicted in Figure 3C, the electron density at the active site of MPro-MI-09 revealed a well-defined configuration for the P1 and P2 residues, as well as the hemithioacetal hydroxide that was formed after the covalent interaction between MI-09 and C145 of MPro. Nevertheless, the N-terminal groups of MI-09 exhibited two distinguishable conformations. While the collected data allowed for refinement of the N-terminal phenyl group, the 4-trifluoromethoxy substituent could not be resolved. Apart from the N-terminal group, MI-09 formed hydrogen bonds with MPro similar to MPI48. The P2 side chain of MI-09 had a rigid configuration that fit nicely into the S2 pocket of MPro. The P2 proline backbone in MI-09 induced a different conformation of the Q189 side chain, unlike in MPro-MPI48. Similar to the other two MPro-inhibitor structures, the aa45-51 region had an undefined conformation.

In all three determined structures, the inhibitors did not fully occupy the S4 pocket. While MPI48 and MPI49 had a rigidly defined N-terminal group in their MPro complexes, it did not interact with the S4 pocket. Similarly, MI-09 exhibited two conformations for its N-terminal group at the active site of MPro, indicating weak interactions with the S4 pocket. Other MPro-dipeptidyl inhibitor complexes have also shown a flexible N-terminal group. Therefore, for the future design of dipeptidyl inhibitors, novel N-terminal groups that can better engage the S4 pocket should be considered to improve binding affinity to MPro. Innovative inputs are required for this purpose.

Cellular M^{Pro} Inhibition and Antiviral Potency of Dipeptidyl Inhibitors.

Due to the observed acute toxicity of MPro to human cells when it was expressed recombinantly, we developed a cell-based assay to evaluate the cellular potency of MPro

inhibitors. The assay involves the use of an MPro-eGFP (enhanced green fluorescent protein) fusion protein that is transiently expressed in 293T cells. An inhibitor with cellular potency can suppress the cytotoxicity of the fusion protein, leading to host cell survival and enhanced overall expression of MPro-eGFP, which can be quantified using flow cytometry. The developed cell-based assay provides a rapid and efficient method for evaluating MPro inhibitors in cells, without the need for time-consuming assessments of cellular permeability and stability. In addition, the assay is more reliable in determining MPro inhibition in cells compared to direct antiviral assays, as compounds may also inhibit host proteases essential for SARS-CoV-2 infection, leading to inaccurate positive results for MPro inhibition. This includes proteases such as TMPRSS2, furin, and cathepsin L, which are critical for viral entry and replication[154, 165, 166]. In the past, we used this system to test various repurposed inhibitors of SARS-CoV-2, and found that some of these inhibitors work through mechanisms that differ from MPro inhibition. We also observed that the inhibitors that showed strong effectiveness in the cellular assay were similarly potent in antiviral tests. In this study, we used the same cellular assay system to assess all the newly synthesized inhibitors that demonstrated enzymatic inhibition with an IC50 value below 0.5 μM. The resulting cellular MPro inhibition EC50 values can be found in Table 1, and the curves that were generated during the characterization process are shown in Figure S3. The Group A compounds with t-butylalanine (**j**) and cyclohexylalanine (**k**) at the P2 site showed significant cellular EC50 values, and four compounds, namely MPI49-MPI52, had cellular EC50 values below 1 μM. Compared to other peptidyl inhibitors that had leucine (**h**) and phenylalanine (**i**) at the P2 site, the compounds with **j** and **k** showed better cellular MPro inhibition potency, suggesting that j and k are the optimal primary amino acid residues at the P2 site for improved cellular MPro inhibition potency. The presence of **j** and **k** at the P2 site is likely to enhance the cellular

permeability or stability of the compounds in cells. However, MPI54, which has a P2 O-t-butylthreonine (**I**), showed very weak cellular potency. In a previous study, we demonstrated that a P3 O-t-butylthreonine (**I**) generally enhances the cellular potency of tripeptidyl MPro inhibitors. The low cellular potency of MPI52 suggests that transferring O-t-butylthreonine (**I**) from P3 to the P2 site does not produce a similar effect.

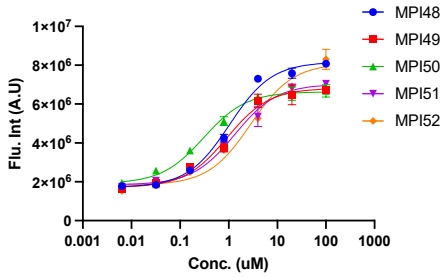

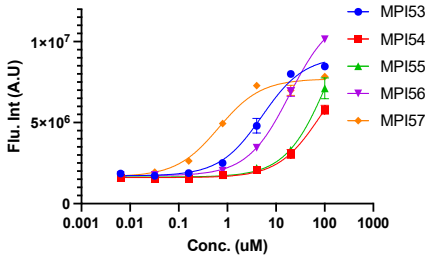

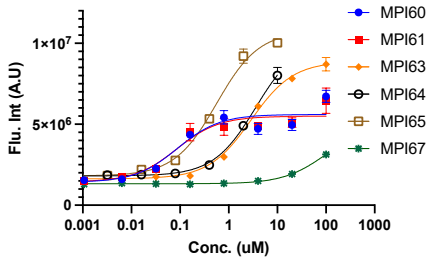

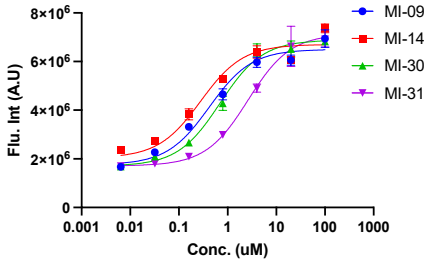

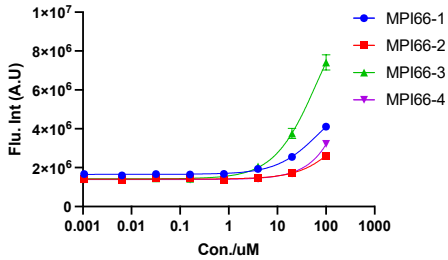

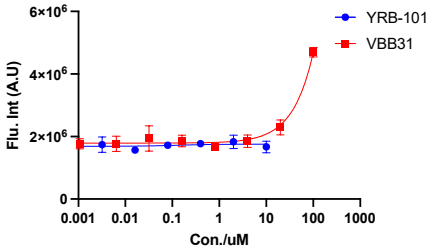

Figure 25. Cellular potency of inhibitors in their inhibition of M^{Pro} to drive host 293T cell survival and overall M^{Pro}-eGFP expression.

For all Group B compounds with an IC50 value below 0.5 μM, measurable cellular Mpro inhibition potency was observed. The two most potent compounds were MPI60 and MPI61, which displayed cellular EC50 values below 100 nM. Notably, among the MPI57-MPI61 compounds, all spiro compounds exhibited superior performance to MPI57, which has a P2 bicyclic residue similar to nirmatrelvir. Furthermore, of all the spiro compounds, MPI58-MPI61, the cellular potency showed a positive correlation with the size of the P2 spiro structure. It is probable that the increased size of the P2 residue enhances the cellular permeability of the corresponding compounds. Of the four previously reported compounds (MI-09, MI-14, MI-30, and MI-31), they demonstrated mild to high cellular potency (> 0.5 μM and < 0.5 μM, respectively), but none of them displayed potency comparable to that of MPI60 and MPI61. In contrast to MPI57, MI-14 displayed better cellular potency, and this improvement may be attributed to q as the N-terminal group. Although q as the N-terminal group in MI-14 led to better cellular potency than MPI57, replacing the N-terminal group with q in MPI58 to form MPI63 resulted in lower cellular potency. Therefore, the effects of N-terminal groups on cellular potency cannot be generalized. For example, replacing the N-terminal CBZ (**a**) group of MPI57 with u in MPI64 and t in MPI65 had opposite effects, with MPI64 displaying worse cellular potency and MPI65 showing better cellular potency. However, even with these modifications, the cellular potency of MPI65 was still notably lower than that of MPI60 and MPI61. Out of all the inhibitors in both Group A and Group B, MPI60 and MPI61 displayed the highest cellular potency. While peptidyl MPro inhibitors with a P2 primary amino acid or bicyclic residue have been widely studied, those with a P2 spiro residue have not been explored as thoroughly. This study is the first of its kind to demonstrate that peptidyl

MPro inhibitors with a P2 **a1** or **a2** residue exhibit superior performance compared to other inhibitors.

Newly developed inhibitors that demonstrated cellular potency with an EC50 value below 1 μM were evaluated for their antiviral potency. To provide a basis for comparison, MPI57 was included in the analysis alongside MPI58-MPI61. However, the antiviral potency of four previously developed compounds (MI-09, MI-14, MI-30, and MI-31) was not assessed in this study as their cellular potency was previously reported to be lower than that of MPI60 and MPI61. To measure the antiviral EC50 values of the inhibitors, plaque reduction neutralization tests were carried out using three SARS-CoV-2 variants, including USA-WA1/2020, in Vero E6 cells. The Vero E6 cells were infected with the virus in the presence of the inhibitors at different concentrations for a period of three days, and the viral plaque reduction was quantified. The antiviral EC50 values for all four inhibitors were determined based on the viral plaque reduction data. The resulting antiviral EC50 values are provided in Table 1, while the antiviral curves can be found in Figure S4. They all had measurable antiviral EC50 values below 10 μM. Five compounds MPI50, MPI59, MPI60, MPI61, and MPI65 had antiviral EC50 values below 1 μM. As same as shown in the cellular potency tests, MPI60 and MPI61 had the highest antiviral potency with a same EC50 value as 0.37 μM. To emphasize the two compounds, their structures are presented again in Figure 26. So, we can conclude that a P2 **a1** or **a2** residue in a dipeptidyl MPro inhibitor leads to optimal antiviral potency and performs better than **x** that has been used in nirmatrelvir.

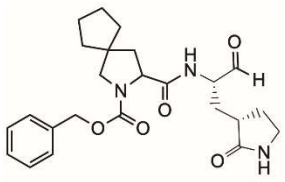

MPI60

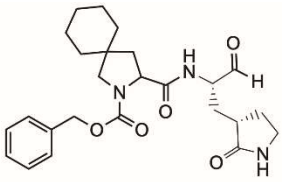

MPI61

Figure 26. Structures of MPI60 and MPI61.

Cytotoxicity and *In Vitro* Metabolic Stability of MPI60 and MPI61.

Because of their potent antiviral properties, MPI60 and MPI61 underwent cytotoxicity and in vitro metabolic stability assessments. To assess cytotoxicity, 293T cells and the MTT assay were employed[167]. The determined CC50 values for MPI60 and MPI61 were 95 and 230 μM, respectively, and are reported in Table 1. Both compounds demonstrated low toxicity, with CC50 values similar to that of nirmatrelvir, leading to high calculated selectivity indices (CC50/antiviral EC50) for both. Human liver microsomes were used to conduct the in vitro metabolic stability analysis for MPI60 and MPI61, and their determined CLint values were 11 and 45 μL/min/kg, respectively, comparable to the literature value for nirmatrelvir of 24.5 μL/min/kg. The collective data indicate that MPI60 and MPI61 possess highly favorable characteristics for progression to animal studies.

CONCLUSION

We have systematically surveyed reversibly covalent dipeptidyl M^{Pro} inhibitors on their characteristics including enzymatic inhibition, crystal structures of their complexes with M^{Pro}, cellular and antiviral potency, cytotoxicity, and *in vitro* metabolic stability. Our results showed that the M^{Pro} S2 pocket is flexible in accommodating large P2 residues in dipeptidyl M^{Pro} inhibitors and inhibitors with two large P2 spiro residues, (*S*)-2-azaspiro[4,4]nonane-3-carboxylate (**a1**) and (*S*)-2-azaspiro[4,5]decane-3-carboxylate (**a2**) are optimal on most characteristics. Two compounds MPI60 and MPI61 displayed the most favorable characteristics, suggesting that they are ready for the next level of preclinical assessment.

MATERIALS AND METHODS

Materials. HEK293T/17 cells were from ATCC; DMEM with high glucose with GlutaMAX supplement, fetal bovine serum, 0.25% trypsin-EDTA, phenol red and dimethyl

sulfoxide were purchased from Thermo Fisher Scientific; linear polyethylenimine MW 25000 was from Polysciences.

In Vitro M^{Pro} inhibition potency characterizations of inhibitors. For most inhibitors, the assay was conducted using 20 nM M^{Pro} and 10 μM Sub3. We dissolved all inhibitors in DMSO as 10 mM stock solutions. Sub3 was dissolved in DMSO as a 1 mM stock solution and diluted 100 times in the final assay buffer containing 10 mM $Na_xH_yPO_4$, 10 mM NaCl, 0.5 mM EDTA, and 1.25% DMSO at pH 7.6. M^{Pro} and an inhibitor were incubated in the final assay buffer for 30 min before adding the substrate to initiate the reaction catalyzed by M^{Pro}. The production format was monitored in a fluorescence plate reader with excitation at 336 nm and emission at 490 nm. More assay details can be found in a previous study.[163]

Cellular M^{Pro} inhibition potency characterizations of inhibitors. Cellular M^{Pro} inhibition potency for all tested inhibitors were characterized according to the protocol shown in a previous report.[162]

Recombinant M^{Pro} protein expression and purification. The expression and purification were conducted according to the procedure in one previous report.[163]

X-Ray Crystallography Analysis. The crystallography analysis of M^{Pro} bound with three inhibitors were conducted according to a previous report.[139]

Compound synthesis. All compounds were synthesized according to the synthetic routes presented in Figure 22 by following the procedures described below.

General procedure A. To a solution of **a** (e.g. MPI48a shown in Scheme 1 and all following **b-k** are named in a same way, 1 eq.) and **b** (1 eq.) in anhydrous DMF was added DIPEA (4 eq.) and the solution was cooled to 0 °C. HATU (1.2 eq.) was added to the solution under 0 °C and then stirred at rt overnight. The reaction mixture was then diluted with ethyl acetate and washed

with saturated $NaHCO_3$ solution (2 times), 1 M HCl solution (2 times), and saturated brine solution (2 times) sequentially. The organic layer was dried over anhydrous Na_2SO_4 and then concentrated *on vacuum*. The residue was then purified with flash chromatography (50-100% EtOAc in hexanes as the eluent) to afford **c** as white solid/gummy solid.

General procedure B. The compound **c** (1 eq.) was dissolved in THF/H_2O (1:1). LiOH (2.5 eq.) was added at 0 °C. The mixture was stirred at rt overnight. Then THF was removed *on vacuum* and the aqueous layer was acidified with 1 M HCl and extracted with dichloromethane (3 times). The organic layer was dried over anhydrous Na_2SO_4 and concentrated to yield **d** as white solid/gummy solid that was proceeded to next step without further purification.

General procedure C. To a solution of **d** (1 eq.) and **Int.i** (1 eq.) in anhydrous DMF was added DIPEA (4 eq.) and the mixture was cooled to 0 °C. HATU (1.2 eq.) was added to the solution under 0 °C and then stirred at rt overnight. The reaction mixture was then diluted with ethyl acetate and washed with saturated $NaHCO_3$ solution (2 times), 1 M HCl solution (2 times), and saturated brine solution (2 times) sequentially. The organic layer was dried over anhydrous Na_2SO_4 and then concentrated *on vacuum*. The residue was then purified with flash chromatography (0-10% MeOH in dichloromethane as the eluent) to afford **e** as white solid/gummy solid.

General procedure D. To a stirred solution of compound **e** (1 eq.) in THF was added $LiBH_4$ (2.0 M in THF, 5 eq.) in several portions at 0 °C under a nitrogen atmosphere. The reaction mixture was stirred at 0 °C for 1 h, allowed to warm up to rt, and then stirred for an additional 2 h. The reaction was quenched by the dropwise addition of 1.0 M HCl (aq.) (1.2 mL) with cooling in an ice bath. The solution was diluted with ethyl acetate and H_2O. The phases were separated, and the aqueous layer was extracted with ethyl acetate (3 times). The organic phases were combined, dried over $MgSO_4$, filtered, and concentrated on a rotorvap to give a yellow oily residue. Column

chromatographic purification of the residue (2-10% MeOH in CH_2Cl_2 as the eluent) afforded **f** as white solid/gummy solid.

General procedure E. To a solution of **f** in CH_2Cl_2 was added $NaHCO_3$ (4 eq.) and the Dess-Martin reagent (3 eq.). The resulting mixture was stirred at rt for 12 h. Then the reaction was quenched with a saturated $NaHCO_3$ solution containing 10 % $Na_2S_2O_3$. The layers were separated. The organic layer was then washed with saturated brine solution, dried over anhydrous Na_2SO_4, and concentrated *on vacuum*. The residue was then purified with flash chromatography afford a final inhibitor compound as white solid.

General procedure F. Intermediate **h** was synthesized according to General Procedure C from **g** and **int.ii**. **h** was used to make **i**. To a stirred solution of **h** (1 eq.) in 1,4-Dioxane at 0 °C was added 4N HCl (10 eq). Reaction mixture was stirred at rt for 3 h. After completion of reaction, solvent was concentrated in a vacuum. The residue **i** was used in the next step without further purification.

General procedure G. There were two routes used to generate intermediate **k**. One was to follow General Procedure A to synthesize **k** from **i** and **j**. The other was to follow the procedure described below. To a stirred solution of **i** (1 eq.) in THF at 0 °C was added DIPEA (2 eq.). After 15 min, Cbz-Cl (1.2 eq) was added, and the mixture was stirred at rt for 3 h. The reaction was quenched with water (5 mL), and the mixture was concentrated in a vacuum. The residue was partitioned between EtOAc (10 mL) and H_2O (5 mL). The aqueous layer was extracted with EtOAc (2 times). The combined organic layer was washed with brine, dried over $MgSO_4$, and concentrated in a vacuum. The residue was then purified with flash chromatography (0-10% MeOH in CH_2Cl_2 as the eluent) to afford **k** as a yellow liquid.

General procedure H. To a stirred solution of **K** (1 eq.) in DCM (10 mL) at 0 °C was added Burgess reagent (2.5 eq.) and the mixture was stirred at rt for 2 h. The reaction was quenched with saturated $NaHCO_3$ solution (5 mL) and extracted with DCM (2 × 10 mL). The combined organic layer was washed with brine, dried over $MgSO_4$, and concentrated in a vacuum. The residue was then purified with flash chromatography (0-10% MeOH in Dichloromethane as the eluent) to afford MPI66-1-67 as a white solid.

CHAPTER IV

A RECURRING CHEMOGENETIC SWITCH FOR CHIMERIC ANTIGEN RECEPTOR T CELLS*

INTRODUCTION

Chimeric antigen receptors (CARs) are engineered T cell receptors that recognize cancer cell surface antigens and activate T cells, then result in cancer cell elimination. Since the appearance of the CAR-T cell therapy technique, the clinical intervention for cancer especially for hematological malignancies has been revolutionized[168-171]. In clinical practice, T cells are extracted from patients' own blood, manufactured with a gene encoding the CAR through virus or non-virus methods, proliferated, and then infused back to patients' body[172-174]. Typically, the CAR structure contains an extracellular antigen binding domain, a transmembrane domain and intracellular signaling domains for an enhanced response for antigen recognition. After infused back to patients' body, they proliferate, recognize the cancer cells targeted and generate a robust immune reaction to eliminate them. CAR-T cell therapy has demonstrated great potential in therapeutics of hematopoietic tumors including different types of leukemia, lymphoma, and myeloma. CAR-T cell therapeutics that have been approved by the U.S. Food and Drug Administration for clinical uses include Kymriah, Yescarta and Tecartus and a lot more are on clinical trials[65, 175-177]. Even though that CAR-T cell therapy can be very powerful, it bears a lot of potential safety concerns. Activation of T cells out of control can cause clinically significant release of inflammatory cytokines, which is also known as cytokine release syndrome (CRS), encephalopathy, multi-organ failure and eventual death[83, 178-180].

*This chapter is reprinted with permission of Wenyue Cao, Zhi Zachary Geng, Na Wang, Quan Pan, Shaodong Guo, Shiqing Xu, Jianfeng Zhou and Wenshe Ray Liu Angewandte Chemie International Edition 2022, 61, e202109550. DOI 10.1002/anie.202109550. Copyright 2022 The Authors.

Thus, developing a CAR-T cell therapy that can be better controlled in clinic would benefit patients profoundly. Also, a controllable CAR-T cell therapy would also help to solve the T cell exhaustion arouse from chronical antigen stimulation, which results in progressive loss of T cell function[181].

A number of methods and designs have been tested to control the activation of T cells in CAR-T cell therapy. For example, proapoptotic safety switch, like suicide genes, have been designed. However, introduction of suicide genes results in irreversible elimination of CAR-T cells[97, 182]. Another strategy that has been developed is to use small molecules or protein adaptors to control cellular functions[88, 92, 183-185]. The small molecule can also be used as CAR expression inducers. However, a lot of these small molecules and protein adaptors are not clinically tested[84, 186, 187]. The administration of them bears significant safety concerns. Another downside, most of the switches designed make the CAR to be turned on when the switch is on. When the switch is turned off, the designs don't have any effect on existing CARs expressed on the cell surface, which makes the turning off effect inefficient. In this chapter, we report a switch that allows recurring turning-on and off of CARs on same T cells, controlled by a small molecule Asunaprevir (ASV).

RESULTS AND DISCUSSION

Design, preparation, and characterization of a recurring chemogenetic CAR switch.

To achieve both on and off effects of a switch in a same CAR-T cell, we set our sights on chemogenetic control of protein functions for our switch design. As stated above, one of the drawbacks of formerly developed switch designs is that the chemical switch hasn't passed clinical tests, so we made sure the molecule used in the chemogenetic design has passed all clinical trials thus wouldn't have any safety concerns. This would also fasten the clinical approval of the

switchable CAR-T therapy designed because one element in this therapy has already eliminated all the safety concerns. We deemed that the hepatitis C virus nonstructural protein 3 protease (HCV-NS3) and its clinically approved inhibitors such as ASV fulfill the requirements necessary as a safe chemogenetic switch[188, 189]. HCV-NS3 is a polypeptide domain of a much larger HCV polypeptide translate which undergoes autoproteolysis. It hydrolyses its both ends to generate the protease protein, the inhibition of this domain by ASV have been used to develop stabilized polypeptide linkages to control proteasome-based degradation of a protein target[77, 99, 190, 191]. In order to build a chemogenetic switch that based on HCV-NS3, for which when ASV is present the complete CAR would be expressed on T cell surface and when ASV is absent the CAR would be degraded, we followed a CAR designed showed in figure 27. firstly, a vector that expresses a standard anti-human CD19 CAR (CAR19) was constructed. This structure was based on a third generation CAR design, which contains an anti-CD19 single chain variable fragment (scFv) generated from a murine monoclonal antibody against human CD19, with the same amino acid sequence as the FDA-approved CAR-T therapy Kymriah, a CD8 hinge domain, a CD28 transmembrane (TM) domain, two costimulatory domains CD28 and 4-1BB (or CD137) for a strong antigen response, and an intracellular CD3ζ tail for homodimer formation and T cell activation. This construct was cloned into a pLVX-EF1α vector to afford plasmid pLVX-EF1α-CAR19. Combined with two other plasmids psPAX2 and PMD2.G, we used these three plasmids to transfect HEK 293T/17 cells to package lentivirus particles (described in chapter II), the lentivirus particles were then used to infect human T cells extracted from leukocytes of human donors to produce CAR19 T cells. To introduce the chemogenetic switch we designed based on HCV-NS3, we cloned HCV-NS3 between anti-human CD19 scFv and CD8 hinge domain in plasmid pLVX-EF1α-CAR19 to make plasmid pLVX-EF1α-sCAR19 to express switchable

CAR19. In sCAR19, we introduced a T54A mutation to HCV-NS3 to improve the sensitivity for ASV. Two HCV-NS3 cleavage sites were inserted in the construct, one between anti-human CD19 scFv and HCV-NS3, one between CD8 hinge domain and CD28 TM domain. To improve the autoproteolysis activity of HCV-NS3, we followed a previous design by fusing an HCV NS4 cofactor fragment at the HCV-NS3 N-terminal side. Plasmid pLVX-EF1 α -CAR19 was then used to generate sCAR19 T cells by following the same procedure described for the construction of CAR19 T cells.

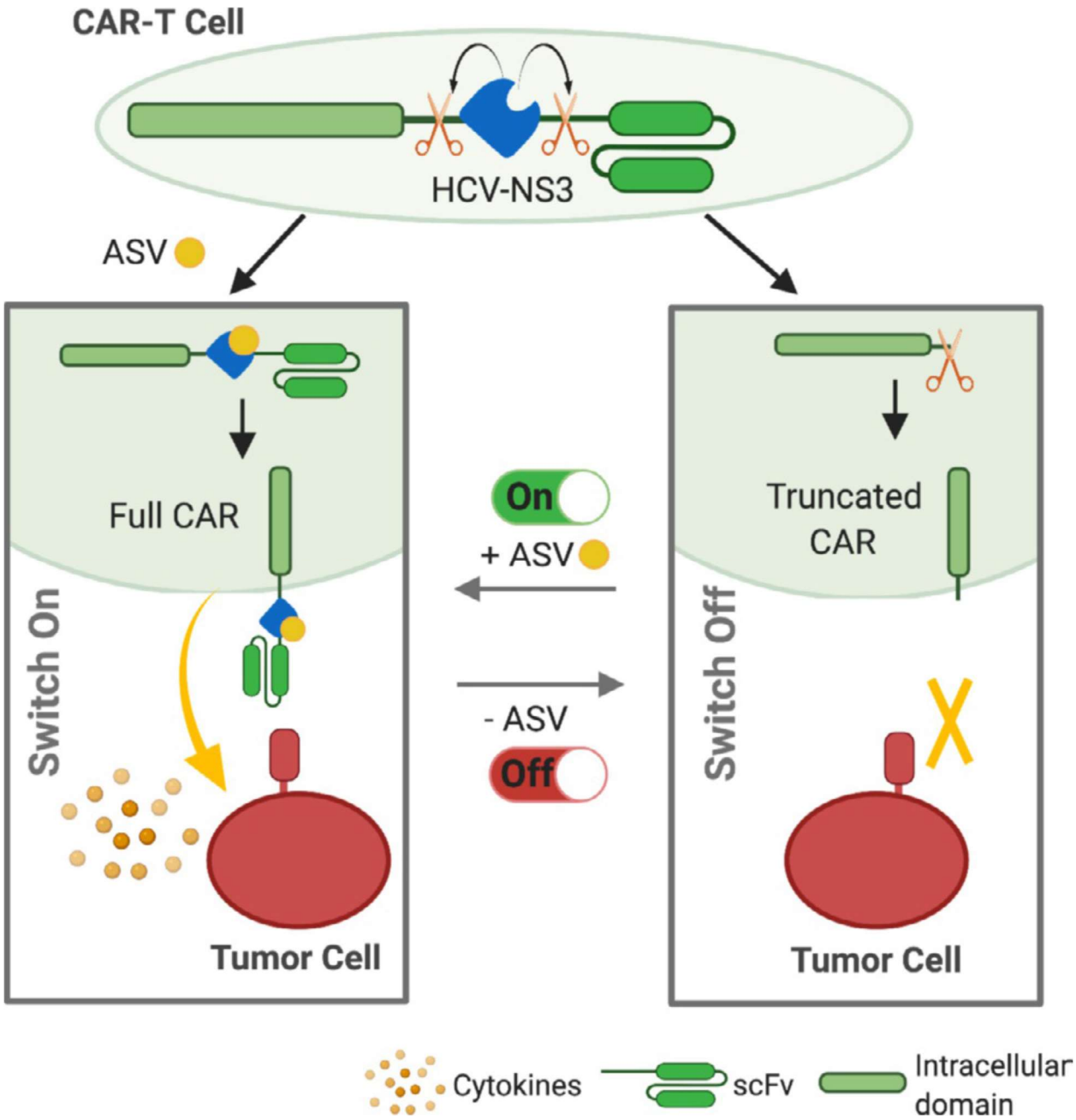

Figure 27. Graphic illustration of a reversible chemogenetic switch that uses asunaprevir (ASV) in coordination with the hepatitis C virus NS3 protease (HCV-NS3) to regulate CAR presentation on the T cell surface. In the absence of ASV, T cells undergo proliferation without turning active while the presence of ASV triggers full CAR display to activate T cells for immunogenic elimination of tumor cells along with cytokine release and potential T cell exhaustion. Removal of ASV switches off active CAR-T cells by cleaving the displayed CAR. (The Figure was developed using the online service provided by BioRender.com).

We tested the expression of CAR on the transduced T cells using Alexa Fluor 647-anti-mouse $F(ab)^2$ antibody. Un-transduced T cells expressed no CAR19, standard CAR19 T cells

expressed CAR19 with or without ASV, while the sCAR19 T cells expressed full-length sCAR19 with a positive correlation to the presence of ASV in the growth media. Without ASV, there was close to no detectable level of sCAR19 displayed on the T cells. However, the addition of 1 μM ASV to the growth media resulted in the display of full-length sCAR19 on the cell surface (24% of all sorted cells). When we wash out ASV from sCAR19 T cell culture medium, the expression level of sCAR19 on the surface of the cells declined gradually. After 24h, the expression level dropped to 1%; after 48h, it's almost undetectable. Meanwhile, we cultured sCAR19 T cells under 1 μM ASV for the same time range, and the expression level of CAR showed no difference. Collectively, our data establish that the display of full-length sCAR19 on sCAR19 T cells can be recurrently regulated by the presence of ASV and withdrawing ASV can effectively lead to total cleavage of full-length sCAR19 on all sCAR19 T cells.

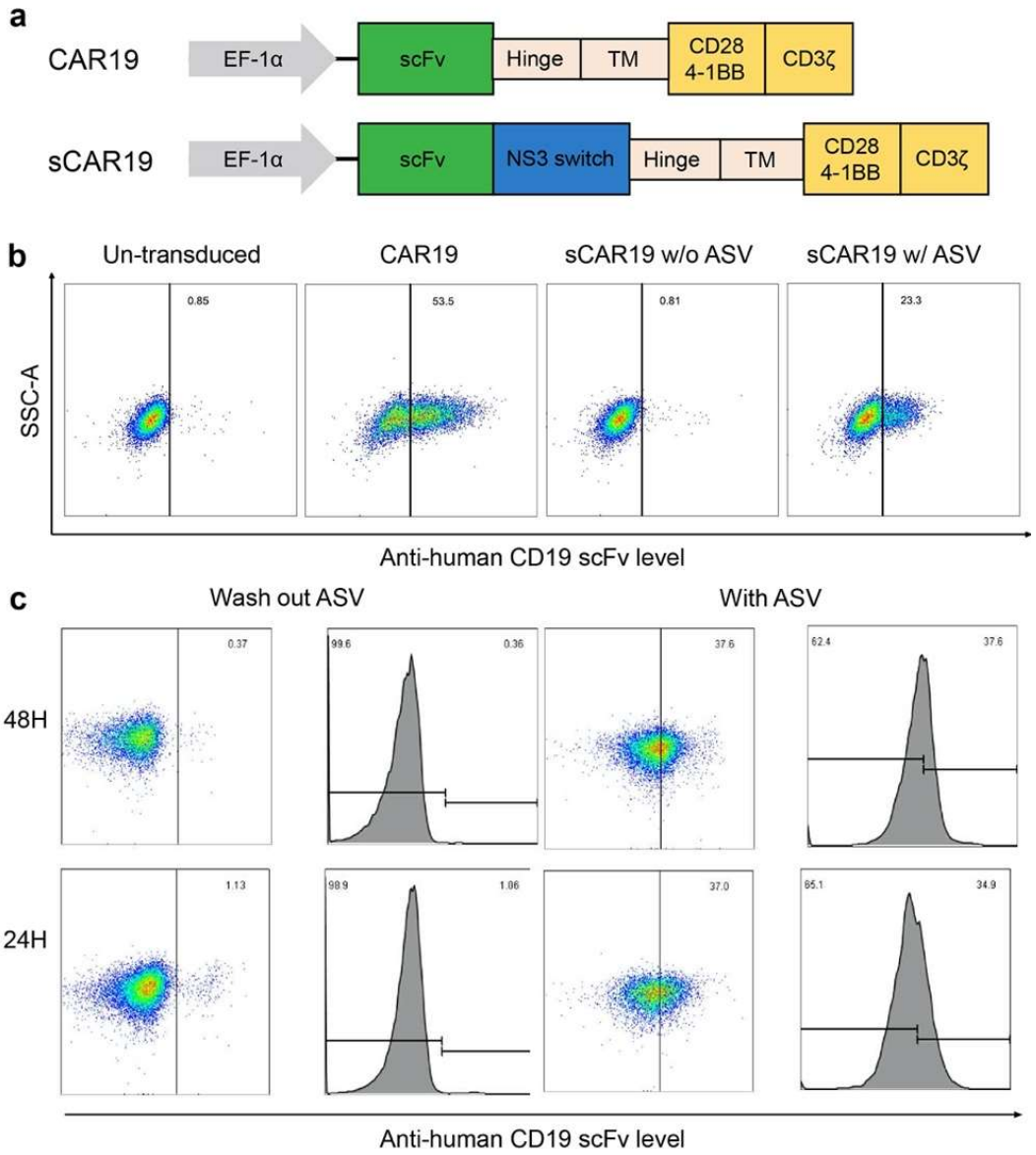

Figure 28. The recurring chemogenetic switch demonstrates both on and off effects in the regulation of CAR display on the T cell surface. (a) Schematic representation of expression vector designs for a standard CAR19 and a switchable CAR19 (sCAR19) containing an HCV-NS3-based recurring switch. Both CARs are under control of an EF1α promoter. (b) Density plots showing distinct anti-human CD19 scFv presentation on un-transduced T cells, CAR19 T cells, and sCAR19 T cells cultured under two conditions, one with a DMSO vehicle and the other with 1 μM ASV. The display of anti-human CD19 scFv was determined by flow cytometry using Alexa Fluor 647-anti-mouse F(ab)^2 antibody. sCAR19 T cells were cultured with the vehicle or ASV for 24 h before the flow cytometry analysis. (c) The cleavage of anti-human CD19 scFv from sCAR19 T cells that were cultured originally with 1 μM ASV to display full-length sCAR19 and then with ASV withdrawn for 24 and 48 h. sCAR19 T cells that were cultured continuously with 1 μM ASV were used as

controls. Alexa Fluor 647-anti-mouse F(ab)^2 antibody was used to label cells for the flow cytometry analysis.

To test whether the level of displayed full-length sCAR19 would be regulated by the dosage of ASV, we cultured sCAR19T cells with a serial of concentrations of ASV ranging from 10nM to 5 μM for 10 h. At 5 μM of ASV, the full-length Scar19 had a highest expression level, and it decreased as the concentration of the compound declined. Normalization of the data indicates that at 10nM, the expression level is equivalent to 50% of that at 5 μM. however, when ASV was absent, almost no full-length sCAR19 was detected. These data indicated that the designed chemogenetic switch is very sensitive to the presence of ASV. To get an insight into how the switch works along with time, we cultured sCAR19 T cells in the presence of different concentrations of ASV for different periods of time with 2 h intervals from 0 to 10 h as well as for 24 h. Expression level of full-length sCAR19 was also determined by anti-mouse F(ab)^2 antibody. From 0 to 10h, the expression level increased steadily and reached a plateau after 10h. interestingly, the expression level of sCAR19 with 5 μM ASV after 10h was almost the same with that of the one with 100nM ASV after 24h, indicating lower dosage of ASV can achieve efficient display of full-length sCAR19 as well.

Effects of the recurring chemogenetic switch on CAR-T characteristics.

the nature of HCV-NS3 being a protease makes its expression on CAR-T cells susceptible for undesired phenotypical consequences. We analyzed the effects on both the switch and ASV on the T cell subset distribution and apoptosis to diffuse this concern. The sCAR19 T cells were cultured with or without ASV for 72 h and then sorted subsets of T cells with antibodies of CD4 and CD8 labelled with different colors. Cell proliferation and early and late apoptotic cells were also analyzed. We also analyzed un-transduced T cells and standard CAR19 T cells as controls. For sCAR19 T cells, the distribution between $CD4^+$ and $CD8^+$ T cells didn't change because of the existence of 5 μM ASV, they maintained around 53% and 43% respectively of the total cells. For the un-transduced cells and standard CAR19 cells, there was no significant difference either. For sCAR19 T cells that were grown with and without 5μM ASV, their early and late apoptotic cell levels were almost identically around 2-3% and 8-9% respectively of the total cells. Both un-transduced and CAR19 T cells also had an early apoptotic level around 2% and late apoptotic cells around 10% (Figure S13). Collectively, data presented here approve that the recurring chemogenetic switch and ASV do not significantly alter T cell characteristics such as CD4+/CD8+ cell distribution and apoptotic cell rates in comparison to a standard CAR design.

We have also analyzed T cell activation in sCAR19 T cells that were grown in the presence of 5 μM ASV in comparison to un-transduced and CAR19 T cells. The constitutively expressed CD25 was detected in 82-85% of the total cells in all three cell types. Similarly, in both switchable sCAR19 and unswitchable CAR19 T cells, CD69, a T cell activation marker exhibited close to an

identical detection level as in un-transduced T cells (figure S14). No significant difference was found between the un-transduced and switchable sCAR T cells ($P > 0.05$).

ASV-regulated cytotoxicity of switchable CAR-T cells *in vitro*.

After we demonstrated controllable T cell activation for sCAR19 T cells when cultured with ASV, we the tested ASV-regulated cytotoxic effects of sCAR19 T cells in killing tumor cells. The tumor cell line we chose was CD19+ Raji cells, which was derived from Burkitt's lymphoma. sCAR19 T cells were cultured with 1μM of ASV for 24h and then mixed with Raji cells with a ratio of 10:1, 5:1, 1:1, respectively. The Raji cells were pre-labelled with calcein AM. 4h later, we measured the amount of calcein AM released to the culture medium, quantifying the amount of Raji cells going through cytolysis. Three control experiments using un-transduced T cells, CAR19 T cells, and sCAR19 T cells cultured in the absence of ASV were also set up as comparisons. As shown in figure. both un-transduced cells and sCAR19 T cells cultured without ASV showed very little cytotoxic effect on Killing Raji cells, at all three different effector-to-target ratios. Both standard CAR19 T cells and sCAR19 T cells cultured with ASV showed very strong killing effect, and its positively correlated to the effector-to-target ratio. At a 10:1 ratio, CAR19 T cells led to cytolysis of around 80% Raji cells in comparison to around 60% Raji cell cytolysis caused by sCAR19 T cells cultured in the presence of ASV. The slightly lower cytotoxic effect from sCAR19 T cells cultured in the presence of ASV is expected since residual HCV-NS3 activity at 1 μM ASV will lead to a low level of sCAR19 cleavage. Also, the HCV-NS3 structure may influence the cytotoxicity.

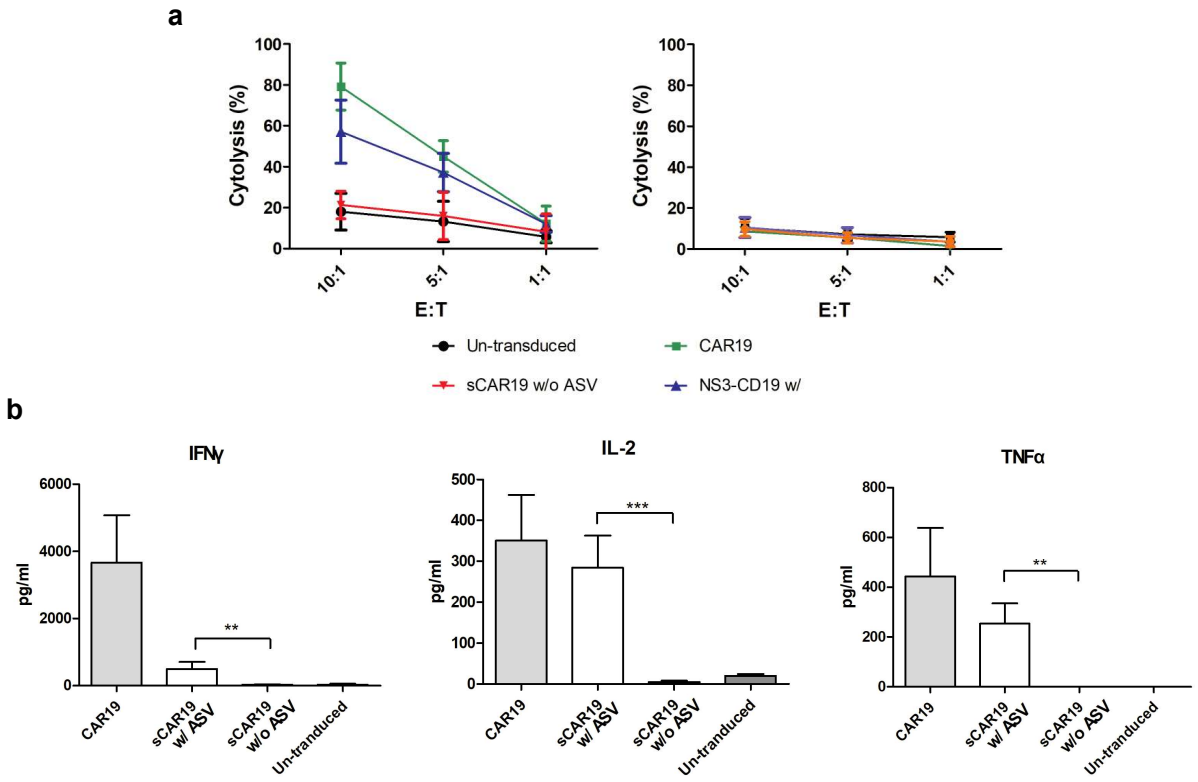

Figure 29. sCAR19 T cells exhibit cytotoxicity *in vitro*. (a) Cytotoxicity of un-transduced T cells, CAR19 T cells and sCAR19 T cells cultured in two conditions, one with the DMSO vehicle and the other with 1 μM ASV toward CD19^{+} Raji (the left graph) and CD19^{-} K562 cells (the right graph). Both Raji and K562 cells were labeled with calcein-AM before they were cocultured with four groups of T cells with ratios of effector to target tumor cells (E:T) as indicated in the figures for 4 h. Lysis of target cells was analyzed by detecting released calcein-AM in media. Data are representative of three independent experiments and normalized against total lysis of calcein-AM-labeled Raji and K562 cells. (b) The release of cytokines including IFN-γ, IL-2 and TNFα from un-transduced T cells, CAR19 T cells and sCAR19 T cells cultured in two conditions, one with the DMSO vehicle and the other with 1 μM ASV when they were cocultured with Raji cells with a E:T ratio as 1:1 for 24 h. Cytokine levels were detected using ELISA.

T cell degranulation is an immune reaction process in response to a detected antigen. To study the impact of the recurring chemogenetic switch on this process, we cocultured sCAR19 T cells and Raji cells with and without 1μM ASV for 4h and then tested the expression level of CD107a, a T cell degranulation marker on T cell surface. Un-transduced T cells and standard

CAR19 T cells were set as negative and positive controls. As the negative control, when tested with phycoerythrin (PE)-conjugated antibody for CD107a, un-transduced T cells showed only 3% detectable labelling. As the positive control, on the other hand, the standard CAR19 T cells displayed about 32% detectable CD107a labelling. For sCAR19 T cells, when cultured with and without ASV, it showed 24% and 5% labelling respectively. These two degranulation levels that were similar to positive and negative controls respectively corresponded to active and inactive T cell antigen-response states pretty well. We then replaced Raji cells with K562(CD19-) cells, which led to no T cell degranulation for sCAR19 T cells cultured under the presence of 1 μM ASV.

To determine when at a low effector-to-target cell ratio, whether the sCAR19 T cells display ASV-regulated long-term anti-tumor effects, we pre-labeled Raji cells with carboxyfluorescein succinimidyl ester (CFSE) and then cocultured the cells with sCAR19 T cells at a 1:10 effector-to-target cell ratio with and without 1 μM ASV for 72 h. after 72h, cells were analyzed to calculate proportion of CFSE+ Raji cells. Experiments were also set up for un-transduced T cells and standard CAR19 T cells as negative and positive controls, respectively. After 3 days of coculturing, the proportion of CFSE+ Raji cells in the un-transduced, CAR19, ASV-absent sCAR19, and ASV-present sCAR19 T group were around 56%, 18%, 53%, and 15% respectively (figure S16). Correspondingly, T cell proportions in the four groups were 42%, 81%, 44%, and 84% respectively. This result shows that ASV-treated sCAR19 T cells can induce a long-term anti-tumor effect even at a lower effector-to-target ratio, comparable to standard CAR19 T cells, and when ASV is absent, the T cells are inert similar to un-transduced T cells. Collectively, data in this section demonstrate that the recurring chemogenetic switch can shift the sCAR19 T

cells between active and inactive T cell states for implementing controllable long-term cytotoxicity effects in eliminating tumor cells in vitro.

ASV-controlled anti-tumor effect of switchable CAR-T cells in mice.

With the clear ASV-regulated anti-tumor effect of sCAR19 T cells *in vitro*, we continued oustudy in an animal model to study the effect *in vivo.* 9. 5×10^5 Raji-Luc cells that stably express luciferase for bioluminescent imaging were infused into 40 mice via intravenous tail injection to induce a lymphoma tumor phenotype. We raised these mice for 7 days and then separated them into 3 groups in which they were intravenously infused with un-transduced T cells, CAR19 T cells, and sCAR19 T cells. We further separate mice in the sCAR19 T group into three subgroups for gavage feeding with three different daily doses of ASV as 0 (a 9:1 PEG400: ethanol vehicle), 2, and 15 mg/kg. to determine whether ASV alone deliver a tumor eradication effect, we gavage fed mice infused with un-transduced T cells with a daily ASV dose as 15 mg/kg. to evaluate tumor engraftment and antitumor activity of different T cells, we measure tumor growth in each mouse by detecting luciferase-catalyzed bioluminescence in its body in different days and use anti-human CD3 and CD19 antibodies to detect human T and Raji cells each week. In the group of mice infused with standard CAR19 T cells, 3 out of 4 mice survived beyond day 28. Tumor cell prevalence climaxed around day 16 after the Raji cell injection and decreased significantly after day 20 indicating a strong antitumor effect from the infused CAR19 T cells. Without ASV, mice infused with sCAR19 T cells all died at day 20. When fed with 2mg/kg ASV daily, the mortality rate of sCAR19 T cells infused mice significantly decreased and 2 mice survived beyond day 20. When the fed ASV was increased to 15mg/kg daily, all four mice survived beyond day 20 and two survived beyond day 28, the tumor cells were also significantly lower at day 20. Mice infused with un-transduced T cells and fed with 15mg/kg ASV daily all died at day 20, indicating ASV alone

doesn't offer an effect of tumor cell eradication. Analysis of tumor cell and T cell proportion in the blood from mice infused with different T cells showed that without ASV, mice infused with sCAR19 T cells had similar level of Raji cells and human T cells as the group pf mice treated with un-transduced human T cells. This indicated that both Raji tumor cells and human T cells proliferated at a similar rate in the groups of mice treated with un-transduced human T cells and ASV-untreated sCAR19 T cells, and both groups of T cells didn't have significant tumor killing effect. The tumor killing effect was significantly improved when ASV was gavage-fed to Raji-grafted mice at a 2 mg/kg daily dose and reached to a level close to the positive-control CAR19 T cells when the ASV dose reached 15 mg/kg. The activation of sCAR19 T cell proliferation was also observed when ASV was injected to Raji-grafted mice and reached to a level close to that from the positive control CAR19 T cells when the ASV dose reached 15 mg/kg (figure 30c and figure S18). The analysis of lentiviral copy numbers per ug of DNA isolated from the blood of mice in different groups also indicated strong ASV-induced sCAR19 T proliferation in mice. Collectively, our results support strongly a robust ASV-controlled anti-tumor effect of sCAR19 T cells in vivo.

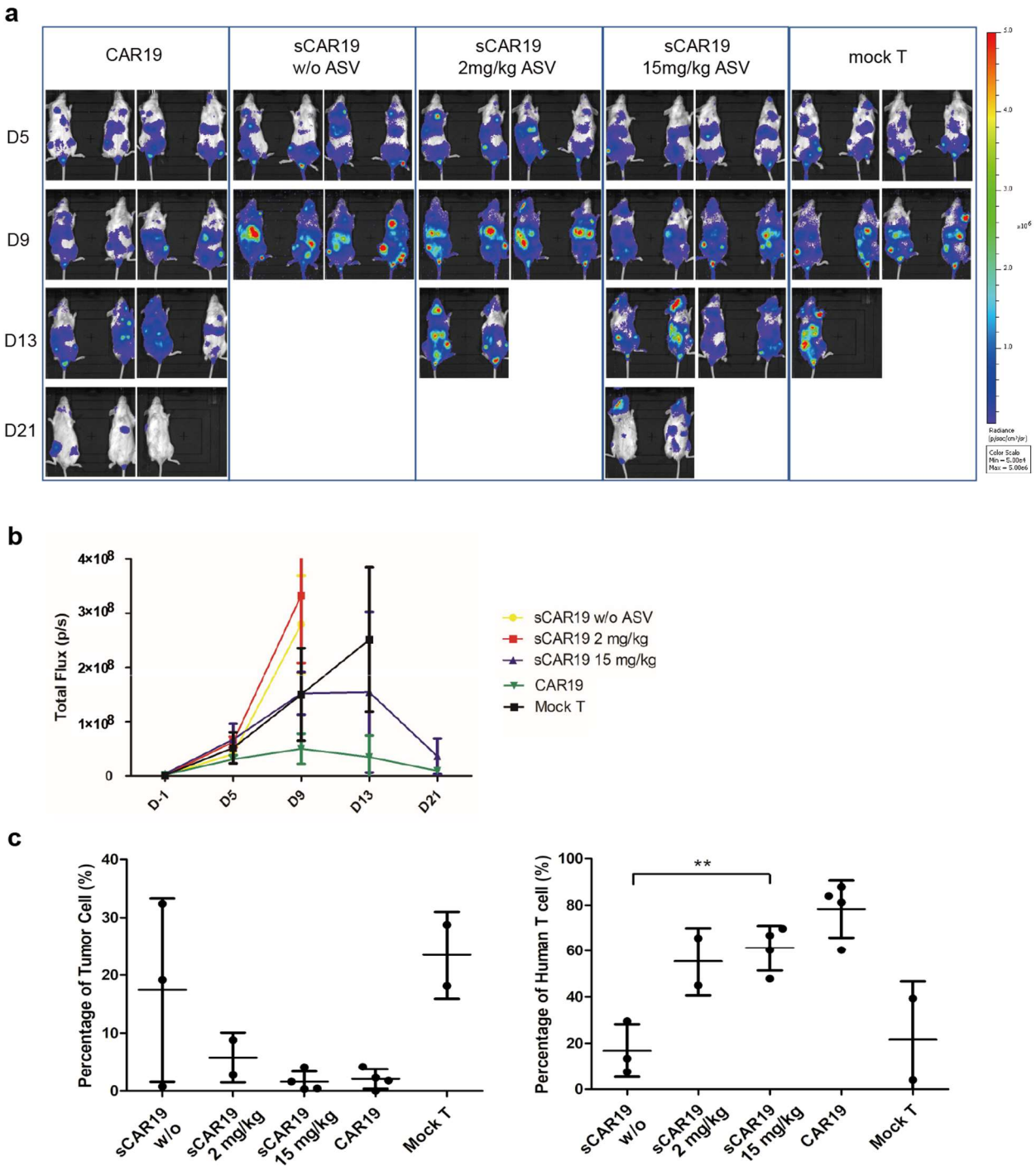

Figure 30. Switchable CAR-T cells in combination with ASV are effective in eliminating human CD19$^+$ tumor cells in mice. (a) Tumor growth in mice that were monitored by bioluminescent imaging. Mice were infused with Raji-Luc cells (5×10^5 cells per mouse) at day 0 and then treated with un-transduced human T cells, CAR19 T cells and sCAR19 T cells (5×10^6 cells per mouse) at day 7. Mice treated with un-transduced T cells were fed daily with 15 mg/kg ASV, mice treated with CAR19 T cells were fed daily with a vehicle (PEG400:ethanol as 9:1) and mice treated with sCAR19 T cells were fed daily with the

vehicle, 2 mg/kg ASV and 15 mg/kg ASV. To image tumor growth, mice were anesthetized and then injected with D-luciferin to undergo whole body bioluminescent imaging. (b) Tumor cell growth and elimination indicated by luciferase-catalyzed bioluminescence. Whole body bioluminescence for each survived mouse that was detected from the ventral side was used for the calculation. Y axis indicates the average bioluminescent signals for each survived mouse. (c) Raji and human T cell counts in blood from mice with different treatments at day 18. The percentages were determined with respect to all leukocytes in collected blood.

CONCLUSION

Unlike small molecules with well-defined pharmacokinetic/pharmacodynamic features, the unpredictability of CAR-T cell therapeutics faces unique treatment challenges regarding the dose control. The ability to regulate the activity and survival of these live drugs has dual benefits of promoting efficacy without abandoning safety33, 34. By introducing a recurring chemogenetic switch into the CAR that can be regulated through a small molecule, the problem turns into control of the dosage of the small molecule, which in the current work is a well-studied FDA approved HCV-NS3 inhibitor ASV. Using ASV to regulate activity of HCV-NS3 embedded in sCAR19, we show that full-length sCAR19 was displayed on its host CAR-T cell surface in an ASV-dose dependent manner. More importantly, we found that the removal of ASV resulted in gradual elimination of the CAR, and as fast as in 24 h the CAR level decreased to an insignificant level. Most biological characterization results prove that CAR-T cells with this recurring chemogenetic switch behave similarly to standard CAR-T cells and ASV regulates, with a dose dependent manner, the antitumor effect of switchable CAR-T cells both in vitro at the cellular level and in vivo in mice. Due to its recurring control nature, we believe this novel chemogenetic CAR switch will find critical applications in CAR-T cell therapy in mitigating serious side effects such as cytokine release syndromes and T cell exhaustion. Since ASV is an FDA-approved medication and sCAR19 in the current work was derived from an approved CAR-T therapeutic, the combined

use of ASV and sCAR19 as a therapeutic can be potentially advanced quickly to undergo clinical investigations in the treatment of hematopoietic tumors such as B-cell lymphoblastic leukemia.

MATERIALS AND EXPERIMENT

Plasmid construction

We ordered two DNA fragments, one coding anti-human CD19 scFv and the other coding CAR domains including the hinge, transmembrane domain and cytoplasmic regions of human CD28, 4-1BB, and CD3ζ from IDT DNA Inc. Sequence information of the two fragments can be found in Supplementary Table 1. We did overlap PCR to ligate the two DNA fragments to make the full-length CAR19 DNA using primers CAR19-F and CAR19-R (primer sequences can be found in table S4), digested the amplified DNA using restriction enzymes EcoRI and MluI, and ligated the digested DNA into the lentiviral plasmid pLVX-EF1α-IRES-puro between sites EcoRI and MluI to afford pLVX-EF1α-CAR19. The plasmid map of pLVX-EF1α-CAR19 is shown in Supplementary Fig. 1. We acquired pLVX-EF1α-IRES-puro from Takara Bio Inc. Its digestion by enzymes EcoRI and MluI removed the coding regions for IRES and the puromycin resistance gene. To add the HCV-NS3 coding sequence into the CAR region of pLVX-EF1α-CAR19, we ordered its DNA fragment from IDT DNA Inc., amplified it using primers NS3-F and NS3-R (table S4), digested it with SpeI and XbaI, and then cloned the digested DNA into pLVX-EF1α-CAR19 between SpeI and XbaI to afford plasmid pLVX-EF1α-sCAR19. In order to build a tumor cell line that stably expresses luciferase, we constructed another plasmid pLVX-puro-Luc. We ordered a DNA fragment coding firefly luciferase (its sequence in table S3), amplified it using primers Luc-F and Luc-R (table S4), digested it with EcoRI and XbaI, and then cloned into pLVX-EF1α-IRES-puro between restriction sites EcoRI and XbaI. We confirmed all constructed plasmids using DNA sequencing services provided by Eton Bioscience Inc.

Cell line culture

We purchased K562, Raji and HEK 293T/17 from American Type Culture Collection. We maintained K562 and Raji cell lines using RPMI 1640 medium with 10% fetal bovine serum (FBS). We cultured HEK 293T/17 with high glucose DMEM medium with 10% FBS. Both media and FBS were acquired from Gibco Inc. All cells were cultured at 37 °C with 5% CO2. Cells at logarithmic growth phase were used for following experiments.

Lentivirus packaging and concentration

We prepared all plasmids for lentivirus packaging using the EndoFree Plasmid Midi Kits from Omega Bio-tek Inc. according to the manufacturer's protocol. For packaging unswitchable CAR19 lentivirus particles, we grew HEK293T/17 cells in ThermoFisher 10 cm dishes to 70-80% confluency and then co-transfected cells with three plasmids pLVX-EF1α-CAR19, psPAX2 and PMD2.G using polyethyleneimine (Polysciences, Inc.) as described previously1. We acquired psPAX2 encoding lentiviral packaging proteins and PMD2.G encoding a lentiviral envelop protein from Addgene (plasmid no. 12260 and 12259 respectively). We grew the transfected cells for 2 days and collected supernatants (10 mL) to isolate viral particles. Additional medium (10 mL) was provided to transfected cells for growing one more day and subsequently we collected supernatants. We centrifuged the collected supernatants at 4000× g at 4 °C to remove cell debris, filtrated the residual supernatants through a 0.45 μm membrane, and then centrifuge at 30,000× g at 4 °C to precipitate viral particles. We then removed the supernatants and resuspended the lentiviral pellets in DMEM medium (200 μL for a total of 200 mL collected supernatant volume). We aliquoted resuspended lentiviral particles as 200 μL/each and stored them at -80 °C. We

detected p24 on lentiviral particles using Lenti-X GoStix Plus Kits provided by Takara Inc. to confirm successful production of lentivirus and titered collected lentiviral particle-containing solutions using 293T cells following standard protocols and detecting CAR19 expression on infected 293T cells using Alexa Fluor 647-labeled rabbit anti-mouse $F(ab)_2$. To package switchable CAR lentiviral particles, we followed the exact same protocol except replacing plasmid pLVX-EF1α-CAR19 with plasmid pLVX-EF1α-sCAR19. We also produced lentiviral particles for transduce Raji cells to make stable Raji cells expressing luciferase. We followed the same protocol by replacing plasmid pLVX-EF1α-CAR19 with plasmid pLVX-puro-Luc.

T cell isolation, transduction and culture

We purchased leukocyte products from the Gulf Coast Regional Blood Center. In order to isolate T cells, we typically added 20 mL leukocyte products on top of 20 mL Ficoll-Paque solution for density gradient centrifugation from GE Healthcare in a 50 mL Falcon tube and then centrifuged at 800× g at room temperature for 20 min to separate different leukocyte cells. We then collected peripheral blood mononuclear cells (PBMCs) and washed collected cells with a 40 mL sorting buffer containing 1× phosphate buffer saline (PBS) and 2 mM EDTA at pH 7.2 twice and spun down the cells. To isolate T cells from PBMCs, we suspended pelleted PBMCs in the sorting buffer (80 μL for 10^7 cells) with CD3 magnetic microbeads (20μL for 10^7 cells) from Miltenyi Biotec for 15 min at 4 °C according to the capacity of the microbeads. Cell numbers were determined using the standard cell counting approach. We centrifugated the mixture to remove the supernatants and then washed the microbead pellets once with the sorting buffer. We suspended microbead pellets in additional sorting buffer (500 μL for 10^8 cells) and then loaded the suspended microbeads to a LS column (Miltenyi Biotec). We washed the column that was attached to a

magnetic MidiMACS™ separator from Miltenyi Biotec for retaining CD3 magnetic microbeads with the sorting buffer three times to remove CD3-negative cells and then transferred the beads bound with T cells to a 15 mL falcon tube. Cells were washed with the sorting buffer once and suspended in ThermoFisher CTS™ OpTmizer™ medium (Gibco) supplemented with 2 mM L-glutamine (Gibco) in the presence of 200 IU/ml human IL-2 (PeproTech). We then stimulated T cells with Dynabeads™ Human T-Activator CD3/CD28 from ThermoFisher overnight with a ratio of beads to cells as 1:3. To transduce T cells, we incubated them with suspended lentiviral solutions (MOI 3-5) for 24 h with 4 μg/mL polybrene (Sigma-Aldrich) before we replaced the medium with refresh culture medium. T cells were maintained at a density of $0.5\text{-}2\times10^6$/mL at all times.

CAR detection on transduced T cells

For anti-human CD19 scFv detection, we labeled transduced T cells with Alexa Fluor 647-labeled rabbit anti-mouse $F(ab)_2$ antibody from Jackson ImmunoResearch Laboratories Inc. or FITC-labeled human CD19 from AcroBiosystems following the manufacture's protocols. All antibodies and their providers that we used in the current study are listed in table S5. We sorted labeled cells using a CytoFLEX flow cytometer (Beckman Coulter). CAR-positive cells were gated using un-transduced cells as controls. By subtracting the percentage of positive cells in control samples from the percentage of positive cells in CAR19 transduced samples, the background was eliminated. For sCAR19 T cells, we cultured them in various concentrations of ASV for different times before labeling and sorting.

T cell proliferation, subset and apoptosis

To test the proliferation of CAR-T cells, we used carboxyfluorescein diacetate succinimidyl ester (CFSE, ThermoFisher) to label the cells according to the manufacturer's instruction. The apoptosis assay was conducted using an Annexin V Apoptosis Detection Kit (BD Biosciences) according to the manufacturer's instruction. To analyze T cell subsets, we stained T cells with three different color-labeled anti-CD4 and anti-CD8 antibodies from BioLegend Inc. and sorted them using the CytoFLEX flow cytometer. Flow cytometry data analysis was performed using FlowJo software from TreeStar.

The characterization of T cell cytotoxicity by detecting Calcein-AM release

The Calcein-AM release assay was conducted according to a previously reported method3. Briefly, the positive target cells (Raji) and negative target cells (K562) were labeled with Calcein-AM (Biolegend) and then cocultured with effector cells (CAR19 and sCAR19 cells) in 96-well plates at different ratios with PBS + 5% FBS. Spontaneous release wells were set as cocultured target cells and PBS + 5% FBS, and maximum release wells were target cells and lysis solution. After 4 h incubation at 37 °C, the plate was centrifuged at 500× g for 10 min and the supernatants were transferred to another 96-well plate. The fluorescence value of each well (R) was measured with the microplate reader, and the tumor-killing efficiency was calculated by the following formula: Lysis% = (Rexperimental well - Rspontaneous release)/(Rmaximum release - Rspontaneous release) × 100%.

The characterization of T cell cytotoxicity by detecting CD107a expression on the T cell surface

To characterize CD107a expression on T cells, they were cultured together with Raji and K562 cells at 37 °C for 4 h in 24-well plates. For each culture, we added 20 μL original PE-conjugated anti-CD107a solution purchased from ThermoFisher and 1 μL of Golgi Stop (monesin) from BD Biosciences to 500 μL culture medium. For sCAR19 T cells, various concentrations of ASV were provided. We then stained T cells with FITC-conjugated anti-CD3 and sorted them using the CytoFLEX flow cytometer. We analyzed Collected data using FlowJo.

The characterization of cytokines including IFN-α, TNF-α, and IL-2 released to the growth media using ELISAs

We co-cultured 5×105 effector T cells with the same number of target cells, both Raji and K562 cells, in 24-well plates. The plates were incubated at 37 °C for 24 h. After that, we transferred supernatants and characterized their IFN-λ, TNF-α, and IL-2 using ELISA kits provided by ThermoFisher. The characterizations followed the manufacturer's protocols. When two CARs were compared, cytokine release was normalized for CAR expression by dividing the cytokine levels by the fraction of CAR expression. For sCAR19 T cells, various concentrations of ASV were provided to the growth media.

The establishment of Raji-Luc cells

To establish Raji-Luc cells that stably express luciferase, we used lentivirus particles that were packaged from the use of pLVX-puro-Luc to infect Raji cells and cultured the infected cells in the presence of 2 μg/mL puromycin from Gibco Inc. for a week to select stable cells. We verified luciferase expression in selected stable cells after providing 150 ug/ml D-luciferin to the growth media and detecting bioluminescence using an IVIS In Vivo Imaging System (PerkinElmer).

Murine lymphoma experiments

Animal studies were approved by the Texas A&M's Institutional Animal Care and Use Committees. We purchased 5-week-old female NSG mice (NOD.Cg-Prkdcscid Il2rgtm1Wjl/SzJ) from JAX laboratory. We built a CD19 positive tumor model in these mice by engrafting 5×10^5 Raji-Luc cells through tail vein injection. Tumors were allowed to grow for 6 days, and then we infused the mice with 5×10^6 un-transduced, CAR19 or sCAR19 T cells. ASV at two doses as 2 and 15 mg/kg or a vehicle (PEG400 to ethanol as 9:1) was given by oral gavage once a day after the sCAR19 T cell infusion. For the un-transduced T cell control group of mice, 15 mg/kg ASV was given by oral gavage once a day and for the positive CAR19 T control group, the vehicle was given by oral gavage once a day. We evaluated in vivo tumor growth through bioluminescent imaging using the IVIS In Vivo Imaging System twice a week. Before bioluminescent imaging, we anesthetized mice with isoflurane and gave them by intraperitoneal injection 150 mg/kg D-Luciferin potassium salt from MedChemExpress. Bioluminescent images of whole mice were taken 10 minutes after D-luciferin injection and these mice were recorded. Once in two weeks, we collected blood cells from these mice, stained them with FITC-conjugated anti-human CD3 for the detection of human T cells and PE-conjugated anti-human CD19 for the detection of survival Raji-Luc cells, and then sorted them using the CytoFLEX flow cytometer. Percentages of human T cells and tumor cells in all sorted leukocytes were then determined. We also extracted DNA from collected mouse blood and quantified their lentiviral levels by running real-time PCR using primers Lenti-F and Lenti-S. Lentiviral DNA copies per µg overall extracted DNA were then determined. Survived mice were counted every day and the mortality was calculated.

Statistical analysis

The results are presented as the means ± the standard deviations. Student's t-tests were used for data comparisons as indicated in the figure legends. GraphPad Prism 7 were used for all statistical analyses. The number of samples in each experiment is indicated in the figure legends. $P < 0.05$ was considered statistically significant.

REFERENCES

1. Tyrrell, D.A. and M.L. Bynoe, *CULTIVATION OF A NOVEL TYPE OF COMMON-COLD VIRUS IN ORGAN CULTURES.* Br Med J, 1965. **1**(5448): p. 1467-70.
2. Andersen, K.G., et al., *The proximal origin of SARS-CoV-2.* Nature Medicine, 2020. **26**(4): p. 450-452.
3. Peiris, J.S.M., et al., *The Severe Acute Respiratory Syndrome.* New England Journal of Medicine, 2003. **349**(25): p. 2431-2441.
4. Su, S., et al., *Epidemiology, Genetic Recombination, and Pathogenesis of Coronaviruses.* Trends in Microbiology, 2016. **24**(6): p. 490-502.
5. Zumla, A., D.S. Hui, and S. Perlman, *Middle East respiratory syndrome.* The Lancet, 2015. **386**(9997): p. 995-1007.
6. Zaki, A.M., et al., *Isolation of a novel coronavirus from a man with pneumonia in Saudi Arabia.* N Engl J Med, 2012. **367**(19): p. 1814-20.
7. Wu, F., et al., *A new coronavirus associated with human respiratory disease in China.* Nature, 2020. **579**(7798): p. 265-269.
8. Zhou, P., et al., *A pneumonia outbreak associated with a new coronavirus of probable bat origin.* Nature, 2020. **579**(7798): p. 270-273.
9. Saif, L.J., *Coronavirus immunogens.* Vet Microbiol, 1993. **37**(3-4): p. 285-97.
10. Weiss, S.R. and J.L. Leibowitz, *Coronavirus pathogenesis.* Adv Virus Res, 2011. **81**: p. 85-164.
11. Xu, Z., et al., *Pathological findings of COVID-19 associated with acute respiratory distress syndrome.* Lancet Respir Med, 2020. **8**(4): p. 420-422.

12. Zhu, N., et al., *A Novel Coronavirus from Patients with Pneumonia in China, 2019.* New England Journal of Medicine, 2020. **382**(8): p. 727-733.

13. Thiel, V., et al., *Infectious RNA transcribed in vitro from a cDNA copy of the human coronavirus genome cloned in vaccinia virus.* J Gen Virol, 2001. **82**(Pt 6): p. 1273-1281.

14. van der Hoek, L., et al., *Identification of a new human coronavirus.* Nat Med, 2004. **10**(4): p. 368-73.

15. Kim, D., et al., *The Architecture of SARS-CoV-2 Transcriptome.* Cell, 2020. **181**(4): p. 914-921.e10.

16. Chen, Y., Q. Liu, and D. Guo, *Emerging coronaviruses: Genome structure, replication, and pathogenesis.* J Med Virol, 2020. **92**(4): p. 418-423.

17. Lan, J., et al., *Structure of the SARS-CoV-2 spike receptor-binding domain bound to the ACE2 receptor.* Nature, 2020. **581**(7807): p. 215-220.

18. Phan, T., *Genetic diversity and evolution of SARS-CoV-2.* Infect Genet Evol, 2020. **81**: p. 104260.

19. Pillaiyar, T., et al., *An Overview of Severe Acute Respiratory Syndrome-Coronavirus (SARS-CoV) 3CL Protease Inhibitors: Peptidomimetics and Small Molecule Chemotherapy.* J Med Chem, 2016. **59**(14): p. 6595-628.

20. Zhang, L., et al., *α-Ketoamides as Broad-Spectrum Inhibitors of Coronavirus and Enterovirus Replication: Structure-Based Design, Synthesis, and Activity Assessment.* Journal of Medicinal Chemistry, 2020. **63**(9): p. 4562-4578.

21. Low, Z.Y., et al., *SARS coronavirus outbreaks past and present—a comparative analysis of SARS-CoV-2 and its predecessors.* Virus Genes, 2021. **57**(4): p. 307-317.

22. Belouzard, S., V.C. Chu, and G.R. Whittaker, *Activation of the SARS coronavirus spike protein via sequential proteolytic cleavage at two distinct sites.* Proc Natl Acad Sci U S A, 2009. **106**(14): p. 5871-6.

23. Morse, J.S., et al., *Learning from the Past: Possible Urgent Prevention and Treatment Options for Severe Acute Respiratory Infections Caused by 2019-nCoV.* ChemBioChem, 2020. **21**(5): p. 730-738.

24. Hu, Q., et al., *The SARS-CoV-2 main protease (M(pro)): Structure, function, and emerging therapies for COVID-19.* MedComm (2020), 2022. **3**(3): p. e151.

25. Abe, K., et al., *Pro108Ser mutation of SARS-CoV-2 3CLpro reduces the enzyme activity and ameliorates the clinical severity of COVID-19.* Scientific Reports, 2022. **12**(1): p. 1299.

26. Denesyuk, A.I., et al., *Structural and functional significance of the amino acid differences Val(35)Thr, Ser(46)Ala, Asn(65)Ser, and Ala(94)Ser in 3C-like proteinases from SARS-CoV-2 and SARS-CoV.* Int J Biol Macromol, 2021. **193**(Pt B): p. 2113-2120.

27. Akbulut, E., *Investigation of changes in protein stability and substrate affinity of 3CL-protease of SARS-CoV-2 caused by mutations.* Genet Mol Biol, 2022. **45**(2): p. e20210404.

28. Yang, H., et al., *The crystal structures of severe acute respiratory syndrome virus main protease and its complex with an inhibitor.* Proc Natl Acad Sci U S A, 2003. **100**(23): p. 13190-5.

29. Mishra, B., et al., *An in silico discovery of potential 3CL protease inhibitors of SARS-CoV-2 based upon inactivation of the cysteine 145-Histidine 41 catalytic dyad.* J Biomol Struct Dyn, 2022: p. 1-20.

30. Noske, G.D., et al., *A Crystallographic Snapshot of SARS-CoV-2 Main Protease Maturation Process.* J Mol Biol, 2021. **433**(18): p. 167118.

31. Rathnayake, A.D., et al., *3C-like protease inhibitors block coronavirus replication in vitro and improve survival in MERS-CoV–infected mice.* Science Translational Medicine, 2020. **12**(557): p. eabc5332.

32. Lu, I.L., et al., *Structure-based drug design and structural biology study of novel nonpeptide inhibitors of severe acute respiratory syndrome coronavirus main protease.* J Med Chem, 2006. **49**(17): p. 5154-61.

33. Dai, W., et al., *Structure-based design of antiviral drug candidates targeting the SARS-CoV-2 main protease.* Science, 2020. **368**(6497): p. 1331-1335.

34. Chen, S., et al., *Residues on the dimer interface of SARS coronavirus 3C-like protease: dimer stability characterization and enzyme catalytic activity analysis.* J Biochem, 2008. **143**(4): p. 525-36.

35. Webber, S.E., et al., *Tripeptide aldehyde inhibitors of human rhinovirus 3C protease: design, synthesis, biological evaluation, and cocrystal structure solution of P1 glutamine isosteric replacements.* J Med Chem, 1998. **41**(15): p. 2786-805.

36. Yin, J., et al., *A mechanistic view of enzyme inhibition and peptide hydrolysis in the active site of the SARS-CoV 3C-like peptidase.* J Mol Biol, 2007. **371**(4): p. 1060-74.

37. Shi, J., Z. Wei, and J. Song, *Dissection study on the severe acute respiratory syndrome 3C-like protease reveals the critical role of the extra domain in dimerization of the enzyme: defining the extra domain as a new target for design of highly specific protease inhibitors.* J Biol Chem, 2004. **279**(23): p. 24765-73.

38. Shi, J. and J. Song, *The catalysis of the SARS 3C-like protease is under extensive regulation by its extra domain.* Febs j, 2006. **273**(5): p. 1035-45.

39. Needle, D., G.T. Lountos, and D.S. Waugh, *Structures of the Middle East respiratory syndrome coronavirus 3C-like protease reveal insights into substrate specificity.* Acta Crystallogr D Biol Crystallogr, 2015. **71**(Pt 5): p. 1102-11.

40. Kneller, D.W., et al., *Room-temperature X-ray crystallography reveals the oxidation and reactivity of cysteine residues in SARS-CoV-2 3CL M(pro): insights into enzyme mechanism and drug design.* IUCrJ, 2020. **7**(Pt 6): p. 1028-35.

41. Ramos-Guzmán, C.A., J.J. Ruiz-Pernía, and I. Tuñón, *Unraveling the SARS-CoV-2 Main Protease Mechanism Using Multiscale Methods.* ACS Catalysis, 2020. **10**(21): p. 12544-12554.

42. Beigel, J.H., et al., *Remdesivir for the Treatment of Covid-19 - Preliminary Report.* N Engl J Med, 2020.

43. Fischer, W.A., 2nd, et al., *A phase 2a clinical trial of molnupiravir in patients with COVID-19 shows accelerated SARS-CoV-2 RNA clearance and elimination of infectious virus.* Sci Transl Med, 2022. **14**(628): p. eabl7430.

44. Owen, D.R., et al., *An oral SARS-CoV-2 M(pro) inhibitor clinical candidate for the treatment of COVID-19.* Science, 2021. **374**(6575): p. 1586-1593.

45. Beigel, J.H., et al., *Remdesivir for the Treatment of Covid-19-Final Report.* New England Journal of Medicine, 2020. **383**(19): p. 1813-1826.

46. Jayk Bernal, A., et al., *Molnupiravir for Oral Treatment of Covid-19 in Nonhospitalized Patients.* N Engl J Med, 2022. **386**(6): p. 509-520.

47. Rock, B.M., et al., *Characterization of ritonavir-mediated inactivation of cytochrome P450 3A4.* Mol Pharmacol, 2014. **86**(6): p. 665-74.

48. Staud, F., et al., *Expression and function of p-glycoprotein in normal tissues: effect on pharmacokinetics.* Methods Mol Biol, 2010. **596**: p. 199-222.

49. Lee, D.W., et al., *T cells expressing CD19 chimeric antigen receptors for acute lymphoblastic leukaemia in children and young adults: a phase 1 dose-escalation trial.* Lancet, 2015. **385**(9967): p. 517-528.

50. Abramson, J.S., et al., *Pivotal Safety and Efficacy Results from Transcend NHL 001, a Multicenter Phase 1 Study of Lisocabtagene Maraleucel (liso-cel) in Relapsed/Refractory (R/R) Large B Cell Lymphomas.* Blood, 2019. **134**(Supplement_1): p. 241-241.

51. Nastoupil, L.J., et al., *Standard-of-Care Axicabtagene Ciloleucel for Relapsed or Refractory Large B-Cell Lymphoma: Results From the US Lymphoma CAR T Consortium.* J Clin Oncol, 2020. **38**(27): p. 3119-3128.

52. Park, J.H., et al., *Long-Term Follow-up of CD19 CAR Therapy in Acute Lymphoblastic Leukemia.* N Engl J Med, 2018. **378**(5): p. 449-459.

53. Maude, S.L., et al., *Tisagenlecleucel in Children and Young Adults with B-Cell Lymphoblastic Leukemia.* N Engl J Med, 2018. **378**(5): p. 439-448.

54. Hay, K.A., et al., *Factors associated with durable EFS in adult B-cell ALL patients achieving MRD-negative CR after CD19 CAR T-cell therapy.* Blood, 2019. **133**(15): p. 1652-1663.

55. Schuster, S.J., et al., *Tisagenlecleucel in Adult Relapsed or Refractory Diffuse Large B-Cell Lymphoma.* N Engl J Med, 2019. **380**(1): p. 45-56.

56. Locke, F.L., et al., *Long-term safety and activity of axicabtagene ciloleucel in refractory large B-cell lymphoma (ZUMA-1): a single-arm, multicentre, phase 1-2 trial.* Lancet Oncol, 2019. **20**(1): p. 31-42.

57. Turtle, C.J., et al., *CD19 CAR-T cells of defined CD4+:CD8+ composition in adult B cell ALL patients.* J Clin Invest, 2016. **126**(6): p. 2123-38.

58. Lei, W., et al., *Treatment-Related Adverse Events of Chimeric Antigen Receptor T-Cell (CAR T) in Clinical Trials: A Systematic Review and Meta-Analysis.* Cancers (Basel), 2021. **13**(15).

59. Leahy, A.B., et al., *CD19-targeted chimeric antigen receptor T-cell therapy for CNS relapsed or refractory acute lymphocytic leukaemia: a post-hoc analysis of pooled data from five clinical trials.* Lancet Haematol, 2021. **8**(10): p. e711-e722.

60. Raymakers, A.J.N., et al., *Health-related quality of life data collected in chimeric antigen receptor T-cell (CAR-T) therapy clinical trials.* J Cancer Policy, 2021. **30**: p. 100304.

61. Li, J., Y. Tang, and Z. Huang, *Efficacy and safety of chimeric antigen receptor (CAR)-T cell therapy in the treatment of relapsed and refractory multiple myeloma: a systematic-review and meta-analysis of clinical trials.* Transl Cancer Res, 2022. **11**(3): p. 569-579.

62. Zhang, T., et al., *Efficiency of CD19 chimeric antigen receptor-modified T cells for treatment of B cell malignancies in phase I clinical trials: a meta-analysis.* Oncotarget, 2015. **6**(32): p. 33961-71.

63. Jena, B., et al., *Chimeric antigen receptor (CAR)-specific monoclonal antibody to detect CD19-specific T cells in clinical trials.* PLoS One, 2013. **8**(3): p. e57838.

64. Han, S., et al., *Recent clinical trials utilizing chimeric antigen receptor T cells therapies against solid tumors.* Cancer Lett, 2017. **390**: p. 188-200.

65. Locke, F.L., et al., *Phase 1 Results of ZUMA-1: A Multicenter Study of KTE-C19 Anti-CD19 CAR T Cell Therapy in Refractory Aggressive Lymphoma.* Mol Ther, 2017. **25**(1): p. 285-295.

66. Wu, L., et al., *Signaling from T cell receptors (TCRs) and chimeric antigen receptors (CARs) on T cells.* Cell Mol Immunol, 2020. **17**(6): p. 600-612.

67. Guedan, S., et al., *Engineering and Design of Chimeric Antigen Receptors.* Mol Ther Methods Clin Dev, 2019. **12**: p. 145-156.

68. Cappell, K.M. and J.N. Kochenderfer, *A comparison of chimeric antigen receptors containing CD28 versus 4-1BB costimulatory domains.* Nature Reviews Clinical Oncology, 2021.

69. Duong, C.P., et al., *Cancer immunotherapy utilizing gene-modified T cells: From the bench to the clinic.* Mol Immunol, 2015. **67**(2 Pt A): p. 46-57.

70. Louis, C.U., et al., *Antitumor activity and long-term fate of chimeric antigen receptor-positive T cells in patients with neuroblastoma.* Blood, 2011. **118**(23): p. 6050-6.

71. van der Stegen, S.J., M. Hamieh, and M. Sadelain, *The pharmacology of second-generation chimeric antigen receptors.* Nat Rev Drug Discov, 2015. **14**(7): p. 499-509.

72. Carpenito, C., et al., *Control of large, established tumor xenografts with genetically retargeted human T cells containing CD28 and CD137 domains.* Proceedings of the National Academy of Sciences, 2009. **106**(9): p. 3360-3365.

73. Milone, M.C., et al., *Chimeric Receptors Containing CD137 Signal Transduction Domains Mediate Enhanced Survival of T Cells and Increased Antileukemic Efficacy In Vivo.* Molecular Therapy, 2009. **17**(8): p. 1453-1464.

74. Brentjens, R.J., et al., *Safety and persistence of adoptively transferred autologous CD19-targeted T cells in patients with relapsed or chemotherapy refractory B-cell leukemias.* Blood, 2011. **118**(18): p. 4817-4828.

75. Park, J.H., et al., *Long-Term Follow-up of CD19 CAR Therapy in Acute Lymphoblastic Leukemia.* New England Journal of Medicine, 2018. **378**(5): p. 449-459.

76. Fraietta, J.A., et al., *Determinants of response and resistance to CD19 chimeric antigen receptor (CAR) T cell therapy of chronic lymphocytic leukemia.* Nature Medicine, 2018. **24**(5): p. 563-571.

77. Hong, M., J.D. Clubb, and Y.Y. Chen, *Engineering CAR-T Cells for Next-Generation Cancer Therapy.* Cancer Cell, 2020. **38**(4): p. 473-488.

78. Lee, D.W., et al., *Current concepts in the diagnosis and management of cytokine release syndrome.* Blood, 2014. **124**(2): p. 188-95.

79. Santomasso, B.D., et al., *Clinical and Biological Correlates of Neurotoxicity Associated with CAR T-cell Therapy in Patients with B-cell Acute Lymphoblastic Leukemia.* Cancer Discov, 2018. **8**(8): p. 958-971.

80. Howard, S.C., et al., *Tumor lysis syndrome in the era of novel and targeted agents in patients with hematologic malignancies: a systematic review.* Ann Hematol, 2016. **95**(4): p. 563-73.

81. Bonifant, C.L., et al., *Toxicity and management in CAR T-cell therapy.* Mol Ther Oncolytics, 2016. **3**: p. 16011.

82. Schubert, M.L., et al., *Side-effect management of chimeric antigen receptor (CAR) T-cell therapy.* Ann Oncol, 2021. **32**(1): p. 34-48.

83. Wang, N., et al., *Efficacy and safety of CAR19/22 T-cell cocktail therapy in patients with refractory/relapsed B-cell malignancies.* Blood, 2020. **135**(1): p. 17-27.

84. Moghimi, B., et al., *Preclinical assessment of the efficacy and specificity of GD2-B7H3 SynNotch CAR-T in metastatic neuroblastoma.* Nature Communications, 2021. **12**(1): p. 511.

85. Shen, J., et al., *Assessment of folate receptor alpha and beta expression in selection of lung and pancreatic cancer patients for receptor targeted therapies.* Oncotarget, 2018. **9**(4): p. 4485-4495.

86. Zhang, E., et al., *Accurate control of dual-receptor-engineered T cell activity through a bifunctional anti-angiogenic peptide.* Journal of Hematology & Oncology, 2018. **11**(1): p. 44.

87. Pellegrino, C., et al., *Impact of Ligand Size and Conjugation Chemistry on the Performance of Universal Chimeric Antigen Receptor T-Cells for Tumor Killing.* Bioconjugate Chemistry, 2020. **31**(7): p. 1775-1783.

88. Lee, Y.G., et al., *Use of a Single CAR T Cell and Several Bispecific Adapters Facilitates Eradication of Multiple Antigenically Different Solid Tumors.* Cancer Research, 2019. **79**(2): p. 387-396.

89. Cao, Y., et al., *Design of Switchable Chimeric Antigen Receptor T Cells Targeting Breast Cancer.* Angew Chem Int Ed Engl, 2016. **55**(26): p. 7520-4.

90. Ma, J.S., et al., *Versatile strategy for controlling the specificity and activity of engineered T cells.* Proc Natl Acad Sci U S A, 2016. **113**(4): p. E450-8.

91. Zheng, Y., K.S. Nandakumar, and K. Cheng, *Optimization of CAR-T Cell-Based Therapies Using Small-Molecule-Based Safety Switches.* Journal of Medicinal Chemistry, 2021. **64**(14): p. 9577-9591.

92. Wu, C.Y., et al., *Remote control of therapeutic T cells through a small molecule-gated chimeric receptor.* Science, 2015. **350**(6258): p. aab4077.

93. Romano, S., et al., *The emerging role of large immunophilin FK506 binding protein 51 in cancer.* Curr Med Chem, 2011. **18**(35): p. 5424-9.

94. Dumont, F.J. and Q. Su, *Mechanism of action of the immunosuppressant rapamycin.* Life Sci, 1996. **58**(5): p. 373-95.

95. Marin, V., et al., *Comparison of different suicide-gene strategies for the safety improvement of genetically manipulated T cells.* Hum Gene Ther Methods, 2012. **23**(6): p. 376-86.

96. Ciceri, F., et al., *Infusion of suicide-gene-engineered donor lymphocytes after family haploidentical haemopoietic stem-cell transplantation for leukaemia (the TK007 trial): a non-randomised phase I-II study.* Lancet Oncol, 2009. **10**(5): p. 489-500.

97. Philip, B., et al., *A highly compact epitope-based marker/suicide gene for easier and safer T-cell therapy.* Blood, 2014. **124**(8): p. 1277-87.

98. Juillerat, A., et al., *Modulation of chimeric antigen receptor surface expression by a small molecule switch.* BMC Biotechnol, 2019. **19**(1): p. 44.

99. Jacobs, C.L., R.K. Badiee, and M.Z. Lin, *StaPLs: versatile genetically encoded modules for engineering drug-inducible proteins.* Nat Methods, 2018. **15**(7): p. 523-526.

100. Weber, E.W., et al., *Pharmacologic control of CAR-T cell function using dasatinib.* Blood Advances, 2019. **3**(5): p. 711-717.

101. Mestermann, K., et al., *The tyrosine kinase inhibitor dasatinib acts as a pharmacologic on/off switch for CAR T cells.* Science Translational Medicine, 2019. **11**(499): p. eaau5907.

102. Wu, B.X., et al., *Development of molecular and pharmacological switches for chimeric antigen receptor T cells.* Experimental Hematology & Oncology, 2019. **8**(1): p. 27.

103. Weichsel, R., et al., *Profound inhibition of antigen-specific T-cell effector functions by dasatinib.* Clin Cancer Res, 2008. **14**(8): p. 2484-91.

104. Blake, S., et al., *The Src/ABL kinase inhibitor dasatinib (BMS-354825) inhibits function of normal human T-lymphocytes in vitro.* Clin Immunol, 2008. **127**(3): p. 330-9.

105. Forni, G., et al., *COVID-19 vaccines: where we stand and challenges ahead.* Cell Death & Differentiation, 2021. **28**(2): p. 626-639.

106. Guruprasad, L., *Human SARS CoV-2 spike protein mutations.* Proteins: Structure, Function, and Bioinformatics, 2021. **89**(5): p. 569-576.

107. Jangra, S., et al., *SARS-CoV-2 spike E484K mutation reduces antibody neutralisation.* The Lancet Microbe, 2021. **2**(7): p. e283-e284.

108. Zhang, L., et al., *Crystal structure of SARS-CoV-2 main protease provides a basis for design of improved α-ketoamide inhibitors.* Science, 2020. **368**(6489): p. 409-412.

109. Jin, Z., et al., *Structure of Mpro from SARS-CoV-2 and discovery of its inhibitors.* Nature, 2020. **582**(7811): p. 289-293.

110. Qiao, J., et al., *SARS-CoV-2 Mpro inhibitors with antiviral activity in a transgenic mouse model.* Science, 2021. **371**(6536): p. 1374-1378.

111. Günther, S., et al., *X-ray screening identifies active site and allosteric inhibitors of SARS-CoV-2 main protease.* Science, 2021. **372**(6542): p. 642-646.

112. Dai, W., et al., *Structure-based design of antiviral drug candidates targeting the SARS-CoV-2 main protease.* Science, 2020. **368**(6497): p. 1331-1335.

113. Hoffmann, M., et al., *SARS-CoV-2 Cell Entry Depends on ACE2 and TMPRSS2 and Is Blocked by a Clinically Proven Protease Inhibitor.* Cell, 2020. **181**(2): p. 271-280.e8.

114. Zhao, M.-M., et al., *Cathepsin L plays a key role in SARS-CoV-2 infection in humans and humanized mice and is a promising target for new drug development.* Signal Transduction and Targeted Therapy, 2021. **6**(1): p. 134.

115. Pišlar, A., et al., *The role of cysteine peptidases in coronavirus cell entry and replication: The therapeutic potential of cathepsin inhibitors.* PLOS Pathogens, 2020. **16**(11): p. e1009013.

116. Cheng, Y.-W., et al., *Furin Inhibitors Block SARS-CoV-2 Spike Protein Cleavage to Suppress Virus Production and Cytopathic Effects.* Cell Reports, 2020. **33**(2): p. 108254.

117. Ma, C., et al., *Boceprevir, GC-376, and calpain inhibitors II, XII inhibit SARS-CoV-2 viral replication by targeting the viral main protease.* Cell Research, 2020. **30**(8): p. 678-692.

118. Yang, K.S., et al., *A Quick Route to Multiple Highly Potent SARS-CoV-2 Main Protease Inhibitors**.* ChemMedChem, 2021. **16**(6): p. 942-948.

119. Ma, X.R., et al., *MPI8 is Potent against SARS-CoV-2 by Inhibiting Dually and Selectively the SARS-CoV-2 Main Protease and the Host Cathepsin L.* ChemMedChem, 2022. **17**(1): p. e202100456.

120. Song, Y., et al., *A Genetically Encoded FRET Sensor for Intracellular Heme.* ACS Chemical Biology, 2015. **10**(7): p. 1610-1615.

121. Resnick Samuel, J., et al., *Inhibitors of Coronavirus 3CL Proteases Protect Cells from Protease-Mediated Cytotoxicity.* Journal of Virology, 2021. **95**(14): p. e02374-20.

122. Kim, Y., et al., *Broad-Spectrum Antivirals against 3C or 3C-Like Proteases of Picornaviruses, Noroviruses, and Coronaviruses.* Journal of Virology, 2012. **86**(21): p. 11754-11762.

123. Baker, J.D., et al., *A drug repurposing screen identifies hepatitis C antivirals as inhibitors of the SARS-CoV2 main protease.* PLOS ONE, 2021. **16**(2): p. e0245962.

124. Fu, L., et al., *Both Boceprevir and GC376 efficaciously inhibit SARS-CoV-2 by targeting its main protease.* Nature Communications, 2020. **11**(1): p. 4417.

125. Mellott, D.M., et al., *A Clinical-Stage Cysteine Protease Inhibitor blocks SARS-CoV-2 Infection of Human and Monkey Cells.* ACS Chemical Biology, 2021. **16**(4): p. 642-650.

126. Jin, Z., et al., *Structural basis for the inhibition of SARS-CoV-2 main protease by antineoplastic drug carmofur.* Nature Structural & Molecular Biology, 2020. **27**(6): p. 529-532.

127. Vatansever, E.C., et al., *Bepridil is potent against SARS-CoV-2 in vitro.* Proceedings of the National Academy of Sciences, 2021. **118**(10): p. e2012201118.

128. Li, Z., et al., *Identify potent SARS-CoV-2 main protease inhibitors via accelerated free energy perturbation-based virtual screening of existing drugs.* Proceedings of the National Academy of Sciences, 2020. **117**(44): p. 27381-27387.

129. Verschueren, K.H.G., et al., *A Structural View of the Inactivation of the SARS Coronavirus Main Proteinase by Benzotriazole Esters.* Chemistry & Biology, 2008. **15**(6): p. 597-606.

130. Wu, C.-Y., et al., *Stable Benzotriazole Esters as Mechanism-Based Inactivators of the Severe Acute Respiratory Syndrome 3CL Protease.* Chemistry & Biology, 2006. **13**(3): p. 261-268.

131. Ghosh, A.K., et al., *Design, synthesis and antiviral efficacy of a series of potent chloropyridyl ester-derived SARS-CoV 3CLpro inhibitors.* Bioorganic & Medicinal Chemistry Letters, 2008. **18**(20): p. 5684-5688.

132. Pillaiyar, T., et al., *An Overview of Severe Acute Respiratory Syndrome–Coronavirus (SARS-CoV) 3CL Protease Inhibitors: Peptidomimetics and Small Molecule Chemotherapy.* Journal of Medicinal Chemistry, 2016. **59**(14): p. 6595-6628.

133. Hoffman, R.L., et al., *Discovery of Ketone-Based Covalent Inhibitors of Coronavirus 3CL Proteases for the Potential Therapeutic Treatment of COVID-19.* Journal of Medicinal Chemistry, 2020. **63**(21): p. 12725-12747.

134. Sacco, M.D., et al., *Structure and inhibition of the SARS-CoV-2 main protease reveal strategy for developing dual inhibitors against Mpro and cathepsin L.* Science Advances. **6**(50): p. eabe0751.

135. Mellott, D.M., et al., *A Clinical-Stage Cysteine Protease Inhibitor blocks SARS-CoV-2 Infection of Human and Monkey Cells.* ACS Chem Biol, 2021. **16**(4): p. 642-650.

136. Yao, X., et al., *In Vitro Antiviral Activity and Projection of Optimized Dosing Design of Hydroxychloroquine for the Treatment of Severe Acute Respiratory Syndrome Coronavirus 2 (SARS-CoV-2).* Clinical Infectious Diseases, 2020. **71**(15): p. 732-739.

137. Ou, T., et al., *Hydroxychloroquine-mediated inhibition of SARS-CoV-2 entry is attenuated by TMPRSS2.* PLOS Pathogens, 2021. **17**(1): p. e1009212.

138. Ma, C. and J. Wang, *Dipyridamole, chloroquine, montelukast sodium, candesartan, oxytetracycline, and atazanavir are not SARS-CoV-2 main protease inhibitors.* Proceedings of the National Academy of Sciences, 2021. **118**(8): p. e2024420118.

139. Yang, K.S., et al., *A Quick Route to Multiple Highly Potent SARS-CoV-2 Main Protease Inhibitors.* ChemMedChem, 2021. **16**(6): p. 942-948.

140. Ma, C., et al., *Boceprevir, GC-376, and calpain inhibitors II, XII inhibit SARS-CoV-2 viral replication by targeting the viral main protease.* Cell Res, 2020. **30**(8): p. 678-692.

141. Jin, Z., et al., *Structural basis for the inhibition of SARS-CoV-2 main protease by antineoplastic drug carmofur.* Nat Struct Mol Biol, 2020. **27**(6): p. 529-532.

142. Jin, Z., et al., *Structure of M(pro) from SARS-CoV-2 and discovery of its inhibitors.* Nature, 2020. **582**(7811): p. 289-293.

143. Fu, L., et al., *Both Boceprevir and GC376 efficaciously inhibit SARS-CoV-2 by targeting its main protease.* Nat Commun, 2020. **11**(1): p. 4417.

144. Vatansever, E.C., et al., *Bepridil is potent against SARS-CoV-2 in vitro.* Proc Natl Acad Sci U S A, 2021. **118**(10).

145. Li, Z., et al., *Identify potent SARS-CoV-2 main protease inhibitors via accelerated free energy perturbation-based virtual screening of existing drugs.* Proc Natl Acad Sci U S A, 2020. **117**(44): p. 27381-27387.

146. Yao, X., et al., *In Vitro Antiviral Activity and Projection of Optimized Dosing Design of Hydroxychloroquine for the Treatment of Severe Acute Respiratory Syndrome Coronavirus 2 (SARS-CoV-2).* Clin Infect Dis, 2020. **71**(15): p. 732-739.

147. Yang, K.S., et al., *Evolutionary and Structural Insights about Potential SARS-CoV-2 Evasion of Nirmatrelvir.* J Med Chem, 2022. **65**(13): p. 8686-8698.

148. Boras, B., et al., *Discovery of a Novel Inhibitor of Coronavirus 3CL Protease as a Clinical Candidate for the Potential Treatment of COVID-19.* bioRxiv, 2020: p. 2020.09.12.293498.

149. Dampalla, C.S., et al., *Postinfection treatment with a protease inhibitor increases survival of mice with a fatal SARS-CoV-2 infection.* Proc Natl Acad Sci U S A, 2021. **118**(29).

150. Iketani, S., et al., *Lead compounds for the development of SARS-CoV-2 3CL protease inhibitors.* Nat Commun, 2021. **12**(1): p. 2016.

151. Dai, W., et al., *Design, Synthesis, and Biological Evaluation of Peptidomimetic Aldehydes as Broad-Spectrum Inhibitors against Enterovirus and SARS-CoV-2.* J Med Chem, 2022. **65**(4): p. 2794-2808.

152. Ma, C., et al., *Discovery of Di- and Trihaloacetamides as Covalent SARS-CoV-2 Main Protease Inhibitors with High Target Specificity.* J Am Chem Soc, 2021. **143**(49): p. 20697-20709.

153. Ma, Y., et al., *A multi-pronged evaluation of aldehyde-based tripeptidyl main protease inhibitors as SARS-CoV-2 antivirals.* Eur J Med Chem, 2022. **240**: p. 114570.

154. Hoffmann, M., et al., *SARS-CoV-2 Cell Entry Depends on ACE2 and TMPRSS2 and Is Blocked by a Clinically Proven Protease Inhibitor.* Cell, 2020. **181**(2): p. 271-280.

155. Rathnayake, A.D., et al., *3C-like protease inhibitors block coronavirus replication in vitro and improve survival in MERS-CoV-infected mice.* Sci Transl Med, 2020. **12**(557): p. eabc5332.

156. Qiao, J., et al., *SARS-CoV-2 M(pro) inhibitors with antiviral activity in a transgenic mouse model.* Science, 2021. **371**(6536): p. 1374-1378.

157. Zhang, L., et al., *Crystal structure of SARS-CoV-2 main protease provides a basis for design of improved alpha-ketoamide inhibitors.* Science, 2020. **368**(6489): p. 409-412.

158. Bai, B., et al., *Peptidomimetic nitrile warheads as SARS-CoV-2 3CL protease inhibitors.* RSC Med Chem, 2021. **12**(10): p. 1722-1730.

159. Vuong, W., et al., *Improved SARS-CoV-2 M(pro) inhibitors based on feline antiviral drug GC376: Structural enhancements, increased solubility, and micellar studies.* Eur J Med Chem, 2021. **222**: p. 113584.

160. Rabe von Pappenheim, F., et al., *Widespread occurrence of covalent lysine-cysteine redox switches in proteins.* Nat Chem Biol, 2022. **18**(4): p. 368-375.

161. Yang, K.S., et al., *A Novel Y-Shaped, S-O-N-O-S-Bridged Cross-Link between Three Residues C22, C44, and K61 Is Frequently Observed in the SARS-CoV-2 Main Protease.* ACS Chem Biol, 2023.

162. Cao, W., et al., *Evaluation of SARS-CoV-2 Main Protease Inhibitors Using a Novel Cell-Based Assay.* ACS Cent Sci, 2022. **8**(2): p. 192-204.

163. Vatansever, E.C., et al., *Bepridil is potent against SARS-CoV-2 in vitro.* Proc Natl Acad Sci U S A, 2021. **118**(10): p. e2012201118.

164. Zhang, C.H., et al., *Potent Noncovalent Inhibitors of the Main Protease of SARS-CoV-2 from Molecular Sculpting of the Drug Perampanel Guided by Free Energy Perturbation Calculations.* ACS Cent Sci, 2021. **7**(3): p. 467-475.

165. Cheng, Y.W., et al., *Furin Inhibitors Block SARS-CoV-2 Spike Protein Cleavage to Suppress Virus Production and Cytopathic Effects.* Cell Rep, 2020. **33**(2): p. 108254.

166. Zhao, M.M., et al., *Cathepsin L plays a key role in SARS-CoV-2 infection in humans and humanized mice and is a promising target for new drug development.* Signal Transduct Target Ther, 2021. **6**(1): p. 134.

167. Kumar, P., A. Nagarajan, and P.D. Uchil, *Analysis of Cell Viability by the MTT Assay.* Cold Spring Harb Protoc, 2018. **2018**(6): p. 469-471.

168. Maude, S.L., et al., *Chimeric Antigen Receptor T Cells for Sustained Remissions in Leukemia.* New England Journal of Medicine, 2014. **371**(16): p. 1507-1517.

169. Crump, M., et al., *Outcomes in refractory diffuse large B-cell lymphoma: results from the international SCHOLAR-1 study.* Blood, 2017. **130**(16): p. 1800-1808.

170. Neelapu, S.S., et al., *Axicabtagene ciloleucel CAR T-cell therapy in refractory large B-cell lymphoma.* New England Journal of Medicine, 2017. **377**(26): p. 2531-2544.

171. Turtle, C.J., et al., *CD19 CAR-T cells of defined CD4+:CD8+ composition in adult B cell ALL patients.* The Journal of clinical investigation, 2016. **126**(6): p. 2123-2138.

172. Boyiadzis, M.M., et al., *Chimeric antigen receptor (CAR) T therapies for the treatment of hematologic malignancies: clinical perspective and significance.* Journal for ImmunoTherapy of Cancer, 2018. **6**(1): p. 137.

173. Pan, J., et al., *High efficacy and safety of low-dose CD19-directed CAR-T cell therapy in 51 refractory or relapsed B acute lymphoblastic leukemia patients.* Leukemia, 2017. **31**(12): p. 2587-2593.

174. Turtle, C.J., et al., *Immunotherapy of non-Hodgkin's lymphoma with a defined ratio of CD8+ and CD4+ CD19-specific chimeric antigen receptor–modified T cells.* Science translational medicine, 2016. **8**(355): p. 355ra116-355ra116.

175. Majzner, R.G. and C.L. Mackall, *Clinical lessons learned from the first leg of the CAR T cell journey.* Nat Med, 2019. **25**(9): p. 1341-1355.

176. Wang, D., et al., *A Phase I Study of a Novel Fully Human BCMA-Targeting CAR (CT103A) in Patients with Relapsed/Refractory Multiple Myeloma.* Blood, 2021.

177. Schuster, S.J., et al., *Tisagenlecleucel in Adult Relapsed or Refractory Diffuse Large B-Cell Lymphoma.* N Engl J Med, 2019. **380**(1): p. 45-56.

178. Lee, D.W., et al., *Current concepts in the diagnosis and management of cytokine release syndrome.* Blood, 2014. **124**(2): p. 188-195.

179. Santomasso, B.D., et al., *Clinical and Biological Correlates of Neurotoxicity Associated with CAR T-cell Therapy in Patients with B-cell Acute Lymphoblastic Leukemia.* Cancer Discovery, 2018. **8**(8): p. 958-971.

180. Shimabukuro-Vornhagen, A., et al., *Cytokine release syndrome.* J Immunother Cancer, 2018. **6**(1): p. 56.

181. Kasakovski, D., L. Xu, and Y. Li, *T cell senescence and CAR-T cell exhaustion in hematological malignancies.* Journal of Hematology & Oncology, 2018. **11**(1): p. 91.

182. Gargett, T. and M.P. Brown, *The inducible caspase-9 suicide gene system as a "safety switch" to limit on-target, off-tumor toxicities of chimeric antigen receptor T cells.* Front Pharmacol, 2014. **5**: p. 235.

183. Moghimi, B., et al., *Preclinical assessment of the efficacy and specificity of GD2-B7H3 SynNotch CAR-T in metastatic neuroblastoma.* Nat Commun, 2021. **12**(1): p. 511.

184. Duong, M.T., et al., *Two-Dimensional Regulation of CAR-T Cell Therapy with Orthogonal Switches.* Mol Ther Oncolytics, 2019. **12**: p. 124-137.

185. Rodgers, D.T., et al., *Switch-mediated activation and retargeting of CAR-T cells for B-cell malignancies.* Proceedings of the National Academy of Sciences, 2016. **113**(4): p. E459-E468.

186. Giordano-Attianese, G., et al., *A computationally designed chimeric antigen receptor provides a small-molecule safety switch for T-cell therapy.* Nat Biotechnol, 2020.

187. Kim, M.S., et al., *Redirection of genetically engineered CAR-T cells using bifunctional small molecules.* Journal of the American Chemical Society, 2015. **137**(8): p. 2832-2835.

188. Raney, K.D., et al., *Hepatitis C virus non-structural protein 3 (HCV NS3): a multifunctional antiviral target.* J Biol Chem, 2010. **285**(30): p. 22725-31.

189. Mosure, K.W., et al., *Preclinical Pharmacokinetics and In Vitro Metabolism of Asunaprevir (BMS-650032), a Potent Hepatitis C Virus NS3 Protease Inhibitor.* J Pharm Sci, 2015. **104**(9): p. 2813-23.

190. Yu, S., et al., *Next generation chimeric antigen receptor T cells: safety strategies to overcome toxicity.* Molecular Cancer, 2019. **18**(1): p. 125.

191. Butko, M.T., et al., *Fluorescent and photo-oxidizing TimeSTAMP tags track protein fates in light and electron microscopy.* Nat Neurosci, 2012. **15**(12): p. 1742-51.

APPENDIX

CHAPTER II

Figure S1. The plasmid map of pECFP-MPro-EYFP

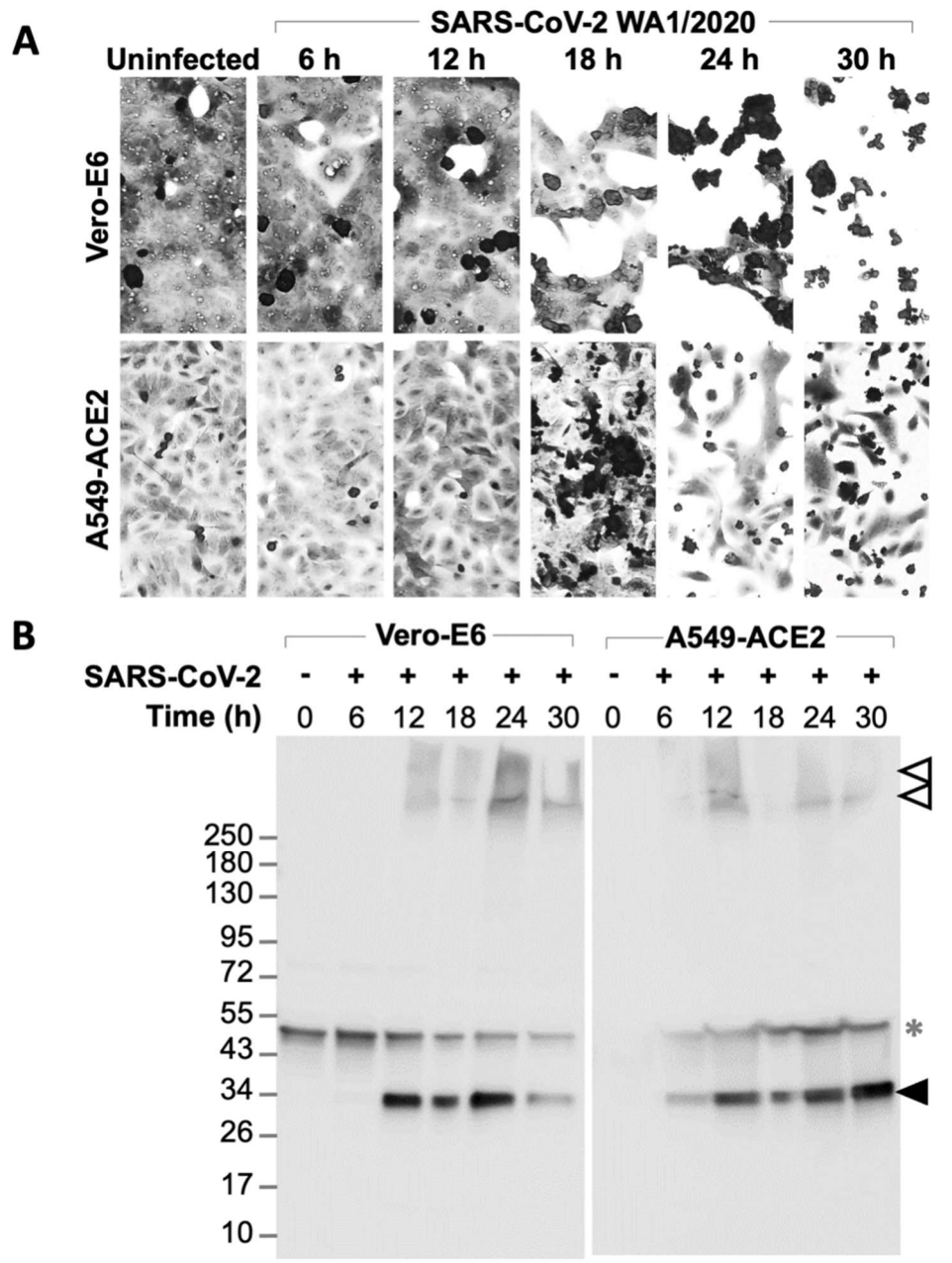

Figure S2 Association of Mpro expression with SARS-CoV-2 cytopathic effects. lines were inoculated with SARS-CoV-2 at different times. For each timepoint, one replicate was fixed and stained with crystal violet (A) and a second replicate was lysed for western blot with anti-Mpro antibody detection (B). Virus-induced cytopathic effects included extensive cell rounding (small, condensed staining) and detachment from the monolayer. Positions of viral polyprotein precursors (white triangles), ~33.7 kDa fully processed Mpro (black triangle) and a nonspecific staining product (asterisk) are indicated.

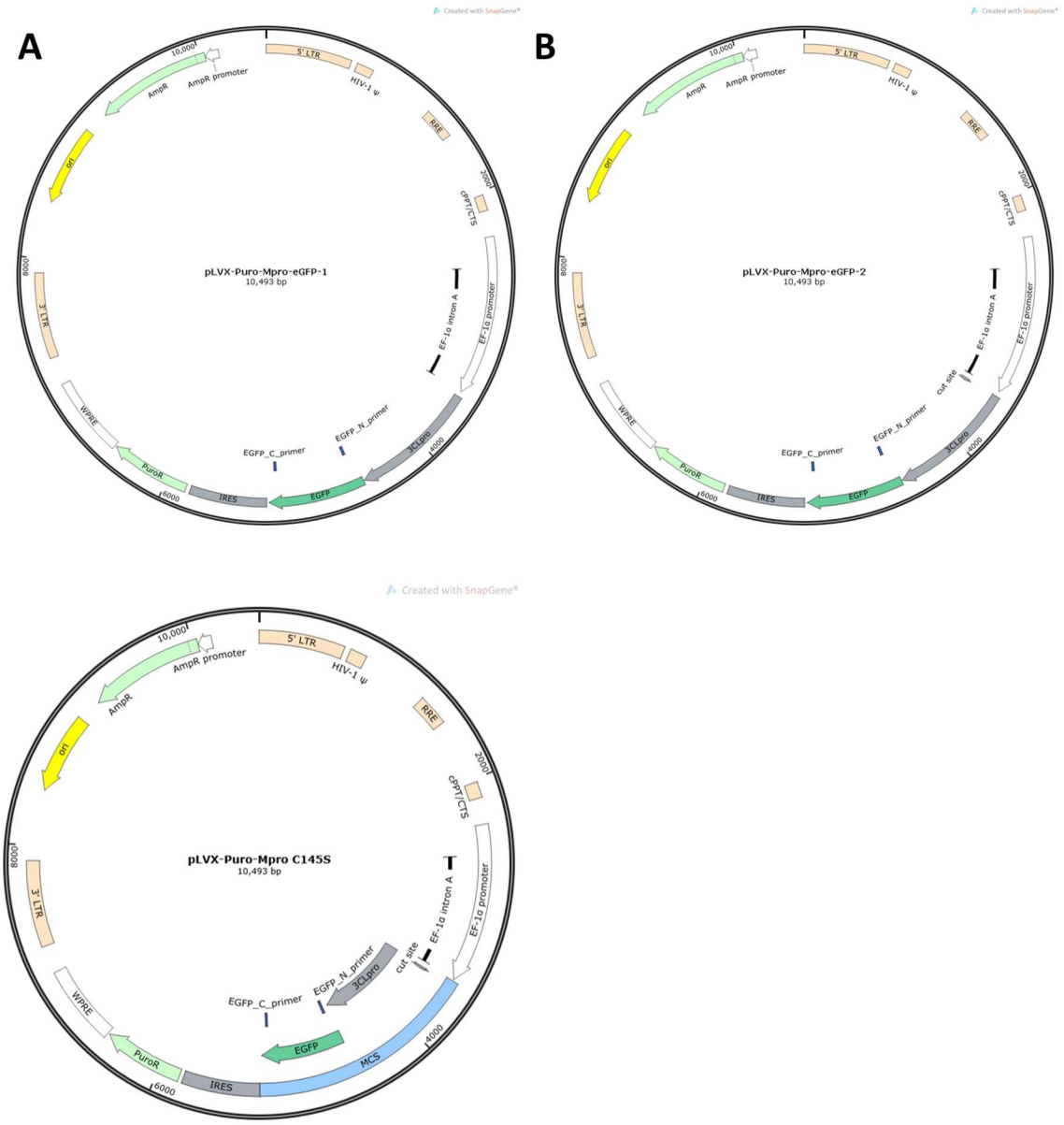

Figure S3 Plasmid maps of pLVX-MPro-eGFP-1 (A), pLVX-MPro-eGFP-2 (B) and pLVX-MProC145S-eGFP

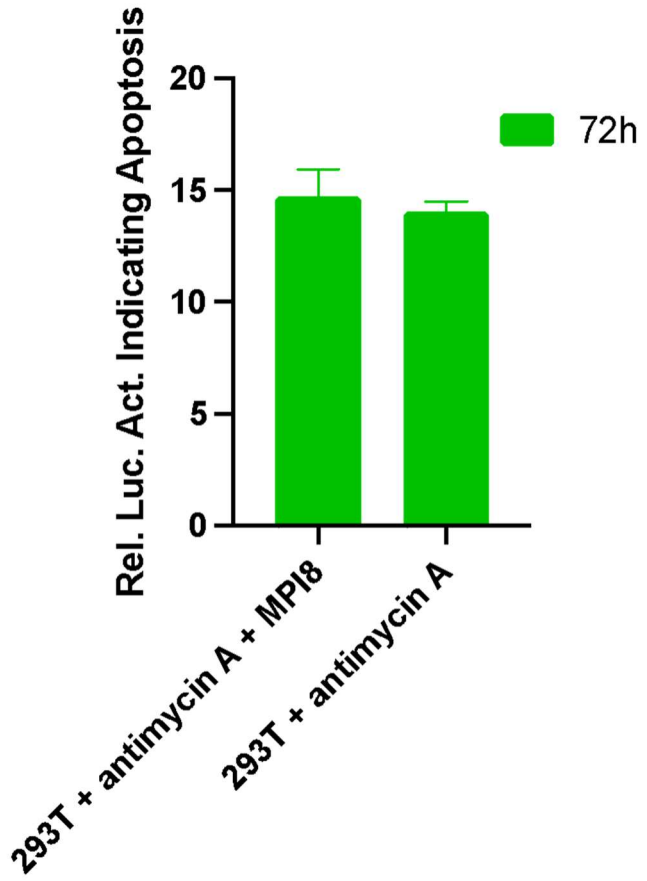

Figure S4 293T cell apoptosis induced by 1 μM antimycin A is not influenced by the addition of 1 μM MPI8.

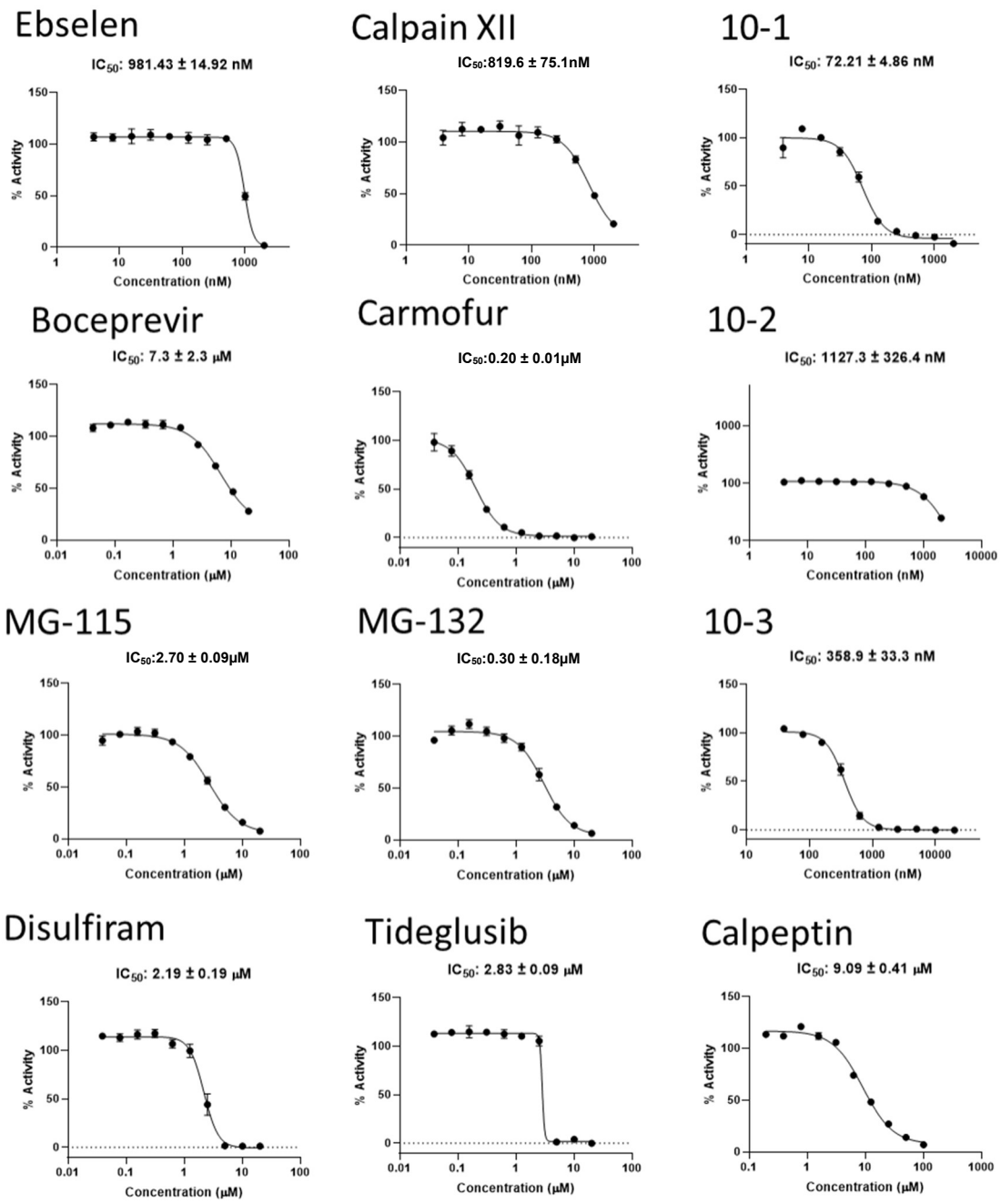

Figure S5. The recharacterization of MPro inhibition.

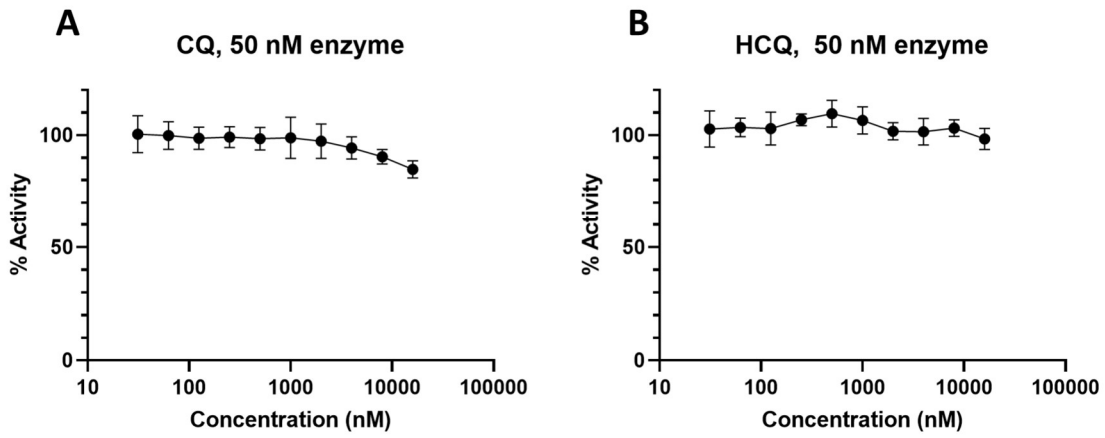

Figure S6. The recharacterization of MPro inhibition by (A) chloroquine and (B) hydroxychloroquine

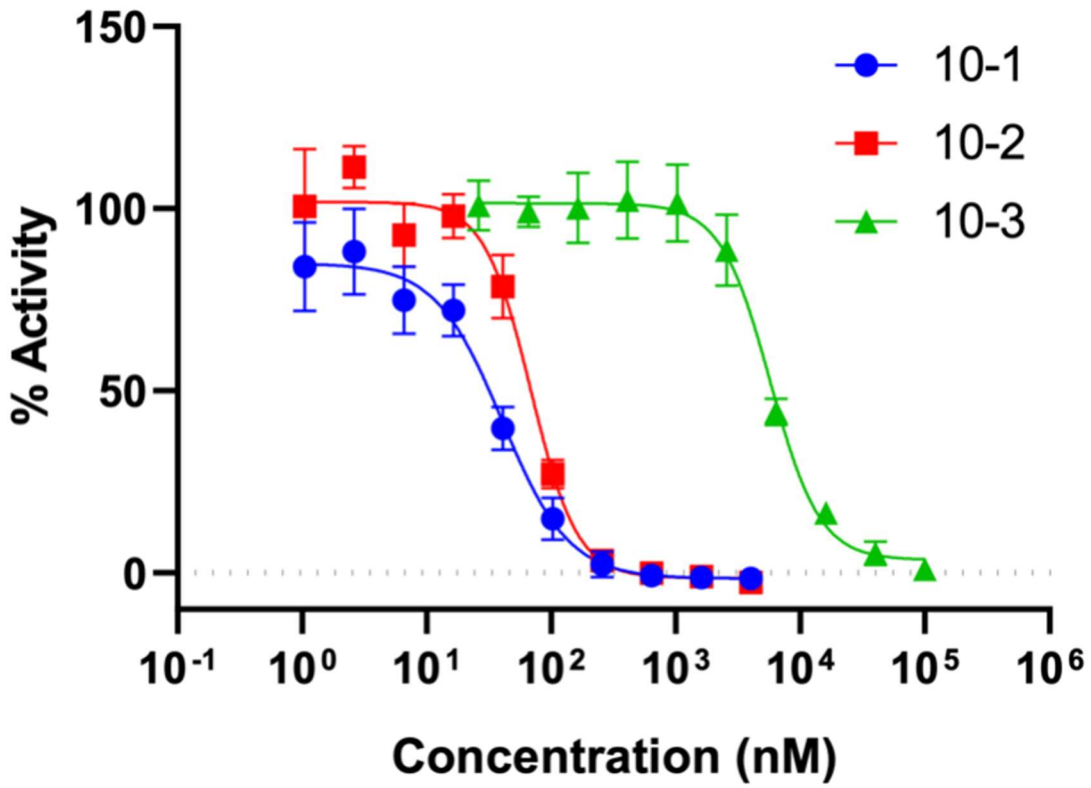

Figure S7. The kinetic characterization of 10-1, 10-2, and 10-3 in their inhibition of MPro.

Primer	Primer
FRET-Mpro-for	AGATCTCGAGTCAAAACAAGCGCGGTGC
FRET-Mpro-rev	TTCGAAGCTTGCTGAAAAGTTACGCCGGAAC
XbaI-Mpro-f	TAGTTCTAGAATGTCAGGGTTTCGCAAG
Mpro-HindIII-r	CCATAAGCTTGCCAAAAGTTACGCCGGAACAC
HinIII-eGFP-f	TGGCAAGCTTATGGTGAGCAAGGGC
eGFP-NotI-r	ATCCGCGGCCGCTTACTTGTACAGCTCGTCCATG
XbaI-Cut-Mpro-f	TAGTTCTAGAATGAAAACAAGCGCGGTGCTCCAGTCAG GGTTTCGCAAGATG
Mpro C145S-f	GAACTTCACAATCAAGGGATCGTTCCTGAATGGGAGTAG CGGTTCGGTTGGATTCAATAT
Mpro C145S-r	AAGAGACGCAGTCGTAGTCGATATTGAATCCAACCGAA CCGCTACTCCCATTCAGGAACG

Table S1 The primers and their sequences used in the construction of plasmids.

	Sequence
siRNA	UUUCCUUCAAGAUCGGUCCCG

Table S2 siRNA sequence used to knock down Mpro expression.

CHAPTER III

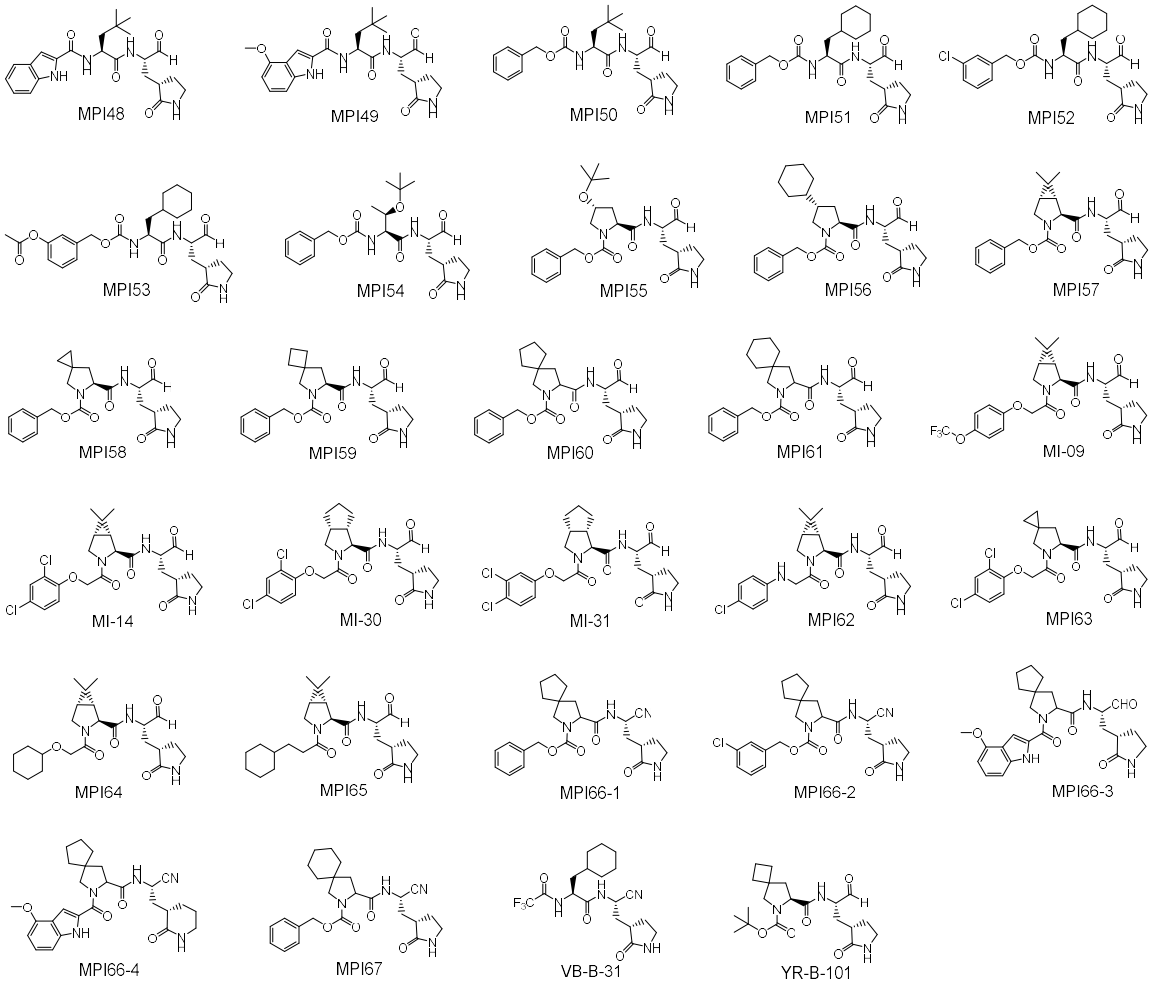

Figure S8. Structures of dipeptidyl M^{Pro} inhibitors.

Table S3. Data Collection and Refinement Statistics

	MPI48 (7SD9)	**MPI49 (7SDA)**	**MI-09 (7SDC)**
Resolution Range	24.28 - 1.85 (1.916 - 1.85)	24.32 - 1.85 (1.916 - 1.85)	24.35 - 1.85 (1.916 - 1.85)
Space Group	I 1 2 1	I 1 2 1	I 1 2 1
Unit Cell	51.661 80.8574 89.6971 90 96.6634 90	51.6838 81.3006 89.2993 90 97.0934 90	54.3646 80.9874 87.8118 90 97.2942 90
Unique Reflections	29850 (2976)	31237 (3071)	31726 (3108)
Completeness (%)	95.31 (95.05)	99.37 (97.93)	98.23 (96.40)

Wilson B-factor	10.94	17.17	20.72
Reflections used in refinement	29849 (2975)	31128 (3069)	31696 (3104)
Reflections used for R-free	1508 (161)	1561 (165)	1542 (151)
R-work	0.2192 (0.3465)	0.2124 (0.3151)	0.2600 (0.4761)
R-free	0.2483 (0.3864)	0.2378 (0.3362)	0.3006 (0.5238)
Number of non-hydrogen atoms	2610	2629	2566
Macromolecules	2360	2360	2360
Ligands	31	33	36
Solvent	219	236	170
Protein Residues	301	301	301
RMS(bonds)	0.010	0.010	0.016
RMS(angles)	1.21	1.22	1.59

Supplementary Synthesis and Characterization of Compounds

Methyl (S)-2-(1H-Indole-2-carboxamido)-4,4-dimethylpentanoate (MPI48c). MPI48c was prepared with methyl (S)-2-amino-4,4-dimethylpentanoate hydrochloride (MPI48b) and 1H-indole-2-carboxylic acid (MPI48a) as a white solid following a general procedure **A** (yield 70%).

(S)-2-(1H-Indole-2-carboxamido)-4,4-dimethylpentanoic acid (MPI48d). MPI48d was prepared as a white solid following a general procedure **B**.

Methyl (S)-2-((S)-2-(1H-indole-2-carboxamido)-4,4-dimethylpentanamido)-3-((S)-2-oxopyrrolidin-3-yl)propanoate (MPI48e). MPI48e was prepared with Int.i and 1H-indole-2-carboxylic acid (MPI48d) as a white solid following a general procedure **C** (yield 60%). ^{1}H NMR (400 MHz, DMSO-d6) δ 11.57 (s, 1H), 8.48 (dd, J = 21.5, 8.1 Hz, 2H), 7.70 – 7.58 (m, 2H), 7.42 (d, J = 8.2 Hz, 1H), 7.23 (s, 1H), 7.17 (t, J = 7.6 Hz, 1H), 7.03 (t, J = 7.4 Hz, 1H), 4.68 – 4.55 (m, 1H), 4.38 – 4.28 (m, 1H), 3.61 (s, 3H), 3.17 – 3.02 (m, 2H), 2.38 – 2.27 (m, 1H), 2.16 – 2.02 (m, 2H), 1.82 – 1.52 (m, 4H), 0.94 (s, 9H).

N-((S)-1-(((S)-1-Hydroxy-3-((S)-2-oxopyrrolidin-3-yl)propan-2-yl)amino)-4,4-dimethyl-1-oxopentan-2-yl)-1H-indole-2-carboxamide (MPI48f). **MPI48f** was prepared as a white solid following a general procedure **D** (yield 60%). ^{1}H NMR (400 MHz, DMSO-d6) δ 11.57 (s, 1H), 8.48 (dd, J = 21.5, 8.1 Hz, 2H), 7.70 – 7.58 (m, 2H), 7.42 (d, J = 8.2 Hz, 1H), 7.23 (s, 1H), 7.17 (t,

J = 7.6 Hz, 1H), 7.03 (t, J = 7.4 Hz, 1H), 4.68 – 4.55 (m, 1H), 4.38 – 4.28 (m, 1H), 3.61 (s, 3H), 3.17 – 3.02 (m, 2H), 2.38 – 2.27 (m, 1H), 2.16 – 2.02 (m, 2H), 1.82 – 1.52 (m, 4H), 0.94 (s, 9H).

(S)-Methyl 2-(4-methoxy-1H-indole-2-carboxamido)-4,4-dimethylpentanoate (MPI49c). MPI49c was prepared with methyl (S)-2-amino-4,4-dimethylpentanoate hydrochloride (MPI48b) and 4-methoxy-1H-indole-2-carboxylic acid (MPI49a) as a white solid following general procedure **A** (yield 79%). ^{1}H NMR (400 MHz, Chloroform-d) δ 10.02 (s, 1H), 7.18 (t, J = 8.0 Hz, 1H), 7.09 – 7.03 (m, 2H), 6.77 (d, J = 8.6 Hz, 1H), 6.48 (d, J = 7.7 Hz, 1H), 4.94 (td, J = 8.9, 3.6 Hz, 1H), 3.93 (s, 3H), 3.76 (s, 3H), 1.89 (dd, J = 14.4, 3.6 Hz, 1H), 1.68 (dd, J = 14.4, 9.1 Hz, 1H), 1.02 (s, 9H). ^{13}C NMR (101 MHz, CDCl3): δ 173.99, 161.39, 154.13, 138.11, 128.91, 125.47, 118.84, 105.32, 100.55, 99.53, 60.44, 55.26, 52.51, 50.14, 30.80, 29.67.

(S)-2-(4-Methoxy-1H-indole-2-carboxamido)-4,4-dimethylpentanoic acid (MPI49d). MPI49d was prepared as a white solid following a general procedure **B** (290 mg, 86%). ^{1}H NMR (400 MHz, DMSO-d6) δ 12.60 (s, 1H), 11.58 (s, 1H), 8.53 (d, J = 8.3 Hz, 1H), 7.33 (d, J = 5.2 Hz, 1H), 7.17 – 6.93 (m, 2H), 6.51 (t, J = 6.2 Hz, 1H), 4.52 (t, J = 8.4 Hz, 1H), 3.89 (s, 3H), 1.93 – 1.80 (m, 1H), 1.78 – 1.70 (m, 1H), 0.95 (s, 9H). 13C NMR (101 MHz, DMSO). δ 175.06, 161.16, 154.08, 138.29, 130.48, 124.89, 118.54, 105.88, 101.34, 99.65, 60.23, 55.50, 49.95, 44.16, 30.89, 29.84.

(S)-Methyl 2-((S)-2-(4-methoxy-1H-indole-2-carboxamido)-4,4-dimethylpentanamido)-3-((S)-2-oxopyrrolidin-3-yl)propanoate (MPI49e). MPI49e was prepared with Int.i and MPI49d as a white gummy solid following general procedure **C** (yield 72%). ^{1}H NMR (400 MHz, Methanol-d4) δ 8.47 (dd, J = 28.2, 7.9 Hz, 1H), 8.22 (dd, J = 17.4, 8.1 Hz, 1H), 7.14 (d, J = 2.8 Hz, 1H), 7.03 (td, J = 8.0, 2.7 Hz, 1H), 6.92 (dd, J = 8.3, 4.9 Hz, 1H), 6.39 (dd, J = 7.8, 2.7 Hz, 1H), 4.68 – 4.59 (m, 1H), 4.48 – 4.35 (m, 1H), 3.81 (s, 3H), 3.60 (s, 2H), 3.16 – 3.02 (m, 2H), 2.51 – 2.39 (m, 1H), 2.26 – 2.02 (m, 2H), 1.86 – 1.55 (m, 4H), 0.92 (s, 9H). ^{13}C NMR (101 MHz, MeOD): δ 180.37, 174.37, 172.27, 162.14, 154.24, 138.41, 129.05, 124.97, 118.71, 104.89, 104.81, 101.53, 98.93, 54.32, 51.47, 51.15, 50.69, 44.44, 40.03, 38.18, 30.13, 30.07, 28.81, 27.29.

N-((S)-1-(((S)-1-Hydroxy-3-((S)-2-oxopyrrolidin-3-yl)propan-2-yl)amino)-4,4-dimethyl-1-oxopentan-2-yl)-4-methoxy-1H-indole-2-carboxamide (MPI49f). MPI49f was prepared as a white solid following a general procedure **D** (yield 58%). ^{1}H NMR (400 MHz, Chloroform-d) δ 10.39 (s, 1H), 8.06 (d, J = 8.0 Hz, 1H), 7.20 – 7.12 (m, 1H), 7.10 – 6.98 (m, 2H), 6.91 (s, 1H), 6.55 – 6.37 (m, 1H), 5.92 (s, 1H), 4.81 – 4.63 (m, 1H), 4.10 – 3.98 (m, 1H), 3.93 (s, 3H), 3.72 – 3.58

(m, 2H), 3.24 – 2.90 (m, 2H), 2.45 – 2.33 (m, 1H), 2.28 – 2.17 (m, 1H), 2.13 – 1.92 (m, 3H), 1.63 (dd, J = 13.8, 8.8 Hz, 2H), 1.03 (s, 3H), 0.96 (s, 6H).

(S)-2-(((Benzyloxy)carbonyl)amino)-4,4-dimethylpentanoic acid (MPI50d). MPI50d was prepared as a white solid following a general procedure **G** (yield 84%). ^{1}H NMR (400 MHz, Chloroform-d) δ 7.15 (s, 5H), 5.71 (s, 1H), 5.08 (d, J = 12.5 Hz, 1H), 4.75 (d, J = 12.6 Hz, 1H), 4.10 (s, 1H), 1.67 (d, J = 14.3 Hz, 1H), 1.29 (dd, J = 14.4, 9.1 Hz, 1H), 0.79 (s, 9H). ^{13}C NMR (100 MHz, Chloroform-d) δ 156.70, 136.50, 128.40, 127.89, 66.77, 30.53, 29.68.

Methyl (S)-2-((S)-2-(((benzyloxy)carbonyl)amino)-4,4-dimethylpentanamido)-3-((S)-2-oxopyrrolidin-3-yl)propanoate (MPI50e). MPI50e was prepared with Int.i and MPI50d as a white gummy solid following general procedure **C** (yield 67%). ^{1}H NMR (400 MHz, Chloroform-d) δ 7.74 (d, J = 7.8 Hz, 1H), 7.32 – 7.22 (m, 5H), 6.78 (s, 1H), 5.46 (d, J = 9.2 Hz, 1H), 5.01 (s, 2H), 4.64 – 4.52 (m, 1H), 4.52 – 4.40 (m, 1H), 3.94 – 3.85 (m, 1H), 3.62 (s, 3H), 3.30 – 3.15 (m, 2H), 2.29 (dd, J = 7.1, 3.2 Hz, 2H), 2.23 – 2.10 (m, 1H), 2.10 – 2.00 (m, 1H), 1.80 – 1.68 (m, 3H), 0.85 (s, 9H). ^{13}C NMR (100 MHz, Chloroform-d) δ 179.83, 173.02, 172.00, 170.90, 156.52, 136.22, 128.54, 128.18, 128.00, 67.07, 60.41, 52.33, 50.90, 46.48, 40.54, 30.95, 30.56, 29.55, 27.95, 21.06, 19.20, 18.08, 14.20.

Benzyl ((S)-1-(((S)-1-hydroxy-3-((S)-2-oxopyrrolidin-3-yl)propan-2-yl)amino)-4,4-dimethyl-1-oxopentan-2-yl)carbamate (MPI50f). MPI50f was prepared as a white solid following a general procedure **D** (yield 51%). ^{1}H NMR (400 MHz, Chloroform-d) δ 7.41 – 7.22 (m, 5H), 6.50 (d, J = 6.3 Hz, 1H), 5.93 (s, 1H), 5.41 (s, 1H), 5.07 (d, J = 4.1 Hz, 2H), 4.17 (d, J = 2.9 Hz, 1H), 3.97 (s, 1H), 3.60 (dd, J = 11.8, 3.4 Hz, 1H), 3.50 (dd, J = 11.7, 6.7 Hz, 1H), 3.26 – 3.05 (m, 2H), 2.40 – 2.29 (m, 1H), 2.29 – 2.19 (m, 1H), 2.08 (d, J = 15.7 Hz, 1H), 1.97 – 1.77 (m, 2H), 1.77 – 1.61 (m, 1H), 0.86 (s, 9H). 13C NMR (100 MHz, Chloroform-d) δ 180.44, 173.62, 173.42, 156.25, 135.91, 128.67, 128.46, 128.37, 67.62, 65.70, 63.37, 53.04, 50.63, 45.79, 40.33, 38.10, 35.36, 32.36, 30.69, 29.69, 28.37, 17.45, 17.11, 17.00.

Methyl (S)-2-((S)-2-(((benzyloxy)carbonyl)amino)-3-cyclohexylpropanamido)-3-((S)-2-oxopyrrolidin-3-yl)propanoate (MPI51e). MPI51e was prepared with Int.i and (S)-2-(((benzyloxy)carbonyl)amino)-3-cyclohexylpropanoic acid (MPI51d) as a white gummy solid following general procedure **C** (yield 67%). ^{1}H NMR (400 MHz, Chloroform-d) δ 7.69 (d, J = 7.0 Hz, 1H), 7.42 – 7.29 (m, 5H), 5.92 (s, 1H), 5.29 (d, J = 8.7 Hz, 1H), 5.18 – 5.04 (m, 2H), 4.50 (s,

1H), 4.29 (d, J = 6.3 Hz, 1H), 3.73 (s, 3H), 3.39 – 3.25 (m, 2H), 2.42 (s, 2H), 2.19 – 2.10 (m, 1H), 1.97 – 1.57 (m, 4H), 1.57 – 1.33 (m, 3H), 1.32 – 1.05 (m, 4H), 1.05 – 0.76 (m, 4H).

(S)-Methyl 2-((((3-chlorobenzyl)oxy)carbonyl)amino)-3-cyclohexylpropanoate (MPI52c). To 3,5-dichlorobenzyl alcohol (0.201 g, 1.39 mmol) in THF (5 mL) were added K_2CO_3 (193 mg, 1.39 mmol) and Triphosgene (166 mg, 0.56 mmol) and the mixture was stirred at rt for 1 h. The mixture was then poured into water (10 mL) and extracted with ethyl acetate (2×20 mL), Combine organic layers and dried over Na_2SO_4. The organic phase was evaporated to dryness and the crude material was used directly in the next step. 3,5-Dichlorobenzyl Chloroformate in THF (5 mL) was added to drop wise to a mixture of methyl (S)-2-amino-3-cyclohexylpropanoate (320 mg,1.39mmol) and DIPEA (0.3 ml, 2.78mmol).The reaction mixture stirred for 12 h. The mixture was then poured into water (30 mL) and extracted with ethyl acetate (4×20 mL). The organic layer was washed with aqueous hydrochloric acid 10% v/v (2×20 mL), saturated aqueous $NaHCO_3$ (2×20 mL), brine (2×20 mL) and dried over Na_2SO_4. The organic phase was evaporated to dryness and the crude material purified by silica gel column chromatography (15-50% EtOAc in n-hexane as the eluent) to afford **MPI52c** white solid (280 mg, 59%). ^{1}H NMR (400 MHz, Chloroform-d) δ 7.45 – 7.05 (m, 4H), 5.22 – 4.86 (m, 2H), 4.34 (td, J = 9.0, 5.1 Hz, 1H), 3.66 (s, 3H), 1.79 – 1.67 (m, 1H), 1.67 – 1.49 (m, 5H), 1.49 – 1.37 (m, 1H), 1.33 – 1.24 (m, 1H), 1.22 – 1.01 (m, 3H), 0.94 – 0.74 (m, 2H).

(S)-2-((((3-Chlorobenzyl)oxy)carbonyl)amino)-3-cyclohexylpropanoic acid (MPI52d). **MPI52d** was prepared as a white solid following a general procedure **B**. ^{1}H NMR (400 MHz, Chloroform-d) δ 8.13 (s, 1H), 7.27 (s, 1H), 7.21 (d, J = 4.4 Hz, 2H), 7.15 (d, J = 4.6 Hz, 1H), 5.28 – 4.79 (m, 2H), 4.44 – 4.16 (m, 1H), 1.82 – 1.70 (m, 1H), 1.69 – 1.53 (m, 5H), 1.51 – 1.42 (m, 1H), 1.38 – 1.28 (m, 1H), 1.22 – 1.02 (m, 3H), 0.95 – 0.77 (m, 2H).

(S)-Methyl 2-((S)-2-((((3-chlorobenzyl)oxy)carbonyl)amino)-3-cyclohexylpropanamido)-3-((S)-2-oxopyrrolidin-3-yl)propanoate (MPI52e). MPI50e was prepared with Int.i and MPI52d as a white gummy solid following general procedure **C** (yield 54%). ^{1}H NMR (400 MHz, Chloroform-d) δ 7.87 (d, J = 6.7 Hz, 1H), 7.37 (s, 1H), 7.29 (d, J = 2.8 Hz, 2H), 7.24 (t, J = 4.1 Hz, 1H), 6.01 (s, 1H), 5.39 (d, J = 8.6 Hz, 1H), 5.10 (s, 2H), 4.50 (s, 1H), 4.34 (d, J = 6.7 Hz, 1H), 3.75 (s, 3H), 3.45 – 3.30 (m, 2H), 2.52 – 2.34 (m, 2H), 2.23 – 2.00 (m, 3H), 1.99 – 1.81 (m, 3H), 1.76 – 1.68 (m, 4H), 1.56 – 1.49 (m, 1H), 1.31 – 1.13 (m, 3H), 1.06 – 0.90 (m, 2H).

3-Chlorobenzyl ((S)-3-cyclohexyl-1-(((S)-1-hydroxy-3-((S)-2-oxopyrrolidin-3-yl)propan-2-yl)amino)-1-oxopropan-2-yl)carbamate (MPI52f). MPI52f was prepared as a white solid following a general procedure **D** (yield 80%). ^{1}H NMR (400 MHz, Chloroform-d) δ 7.75 (d, J = 7.2 Hz, 1H), 7.27 (s, 1H), 7.24 (s, 2H), 7.14 (t, J = 4.6 Hz, 1H), 6.16 (s, 1H), 5.52 (d, J = 8.2 Hz, 1H), 5.00 (s, 2H), 4.39 – 4.10 (m, 1H), 4.03 – 3.82 (m, 1H), 3.65 – 3.46 (m, 2H), 3.32 – 3.16 (m, 2H), 2.44 – 2.25 (m, 2H), 2.02 – 1.89 (m, 1H), 1.79 – 1.69 (m, 2H), 1.64 – 1.50 (m, 6H), 1.50 – 1.39 (m, 2H), 1.27 (s, 1H), 1.17 – 1.01 (m, 3H), 0.95 – 0.73 (m, 2H). ^{13}C NMR (101 MHz, $CDCl_3$) δ 181.09, 173.72, 155.96, 138.55, 134.37, 129.82, 128.20, 127.77, 125.82, 65.91, 53.29, 51.21, 40.67, 38.46, 34.12, 33.71, 32.52, 32.03, 30.96, 28.81, 26.38, 26.24, 26.05.

3-(((((S)-3-Cyclohexyl-1-(((S)-1-hydroxy-3-((S)-2-oxopyrrolidin-3-yl)propan-2-yl)amino)-1-oxopropan-2-yl)carbamoyl)oxy)methyl)phenyl acetate (MPI53f). To a stirred solution of 3-(hydroxymethyl)phenyl acetate (100 mg, 0.599 mmol) and DIPEA (0.31 mL, 1.79 mmol) in dry CH_2Cl_2 (10 mL) was added N,N'-disuccinimidyl carbonate (214 mg, 0.838 mmol) at 0 °C. After 10 h at rt, (S)-2-amino-3-cyclohexyl-N-((S)-1-hydroxy-3-((S)-2-oxopyrrolidin-3-yl)propan-2-yl)propanamide (186 mg, 0.599 mmol) was added one portion at 0 °C. After 10 h at rt, the reaction mixture was evaporated in vacuo. Purification by silica gel chromatography (Dichloromethane/MeOH = 9:1). 150 mg of compound isolated. Yield 50%. ^{1}H NMR (400 MHz, Chloroform-d) δ 7.68 (d, J = 8.3 Hz, 1H), 7.33 (t, J = 7.8 Hz, 1H), 7.18 (d, J = 7.6 Hz, 1H), 7.07 (s, 1H), 7.01 (dd, J = 8.0, 2.3 Hz, 1H), 6.43 (d, J = 17.5 Hz, 1H), 5.70 (t, J = 10.0 Hz, 1H), 5.07 (s, 2H), 4.25 (dd, J = 8.9, 5.3 Hz, 1H), 4.02 – 3.90 (m, 1H), 3.57 (q, J = 8.4, 5.4 Hz, 2H), 3.24 (t, J = 8.4 Hz, 2H), 2.45 – 2.30 (m, 2H), 2.28 (s, 3H), 1.99 (ddd, J = 14.2, 11.0, 5.2 Hz, 1H), 1.81 – 1.73 (m, 2H), 1.64 (td, J = 11.0, 8.6, 4.8 Hz, 6H), 1.49 (td, J = 8.9, 8.3, 4.5 Hz, 1H), 1.33 (s, 1H), 1.16 (ddd, J = 25.5, 16.6, 10.9 Hz, 3H), 0.98 – 0.84 (m, 2H). 13C NMR (101 MHz, CDCl3) δ 181.06, 173.63, 169.52, 156.03, 150.76, 138.20, 129.53, 125.15, 121.26, 120.94, 66.09, 65.78, 53.28, 50.75, 40.68, 40.61, 38.37, 34.10, 33.70, 32.52, 32.15, 28.61, 26.40, 26.24, 26.05, 21.13.

Methyl (1R,2S,5S)-3-(2-(2,4-dichlorophenoxy)acetyl)-6,6-dimethyl-3-azabicyclo[3.1.0]hexane-2-carboxylate (MPI55c). MPI55c was prepared with methyl (1R,2S,5S)-6,6-dimethyl-3-azabicyclo[3.1.0]hexane-2-carboxylate hydrogen chloride (MPI55b) and 2-(2,4-dichlorophenoxy)acetic acid (MPI55a) as a white solid following a general procedure **A** (yield 54%). ^{1}H NMR (400 MHz, Chloroform-d) δ 7.29 (d, J = 2.5 Hz, 1H), 7.14 – 7.02 (m, 1H), 6.79 (dd, J = 8.9, 7.5 Hz, 1H), 4.64 – 4.41 (m, 2H), 4.37 (s, 1H), 3.82 (dd, J = 10.5, 5.3 Hz,

1H), 3.67 (d, J = 1.5 Hz, 1H), 3.64 (d, J = 4.3 Hz, 3H), 1.45 (dd, J = 7.4, 5.1 Hz, 1H), 1.37 (d, J = 7.5 Hz, 1H), 0.98 (d, J = 4.1 Hz, 3H), 0.84 (s, 2H), 0.76 (s, 1H). 13C NMR (100MHz, Chloroform-d) δ 171.82, 171.57, 166.18, 165.75, 152.24, 130.15, 130.10, 127.78, 127.67, 126.72, 123.56, 123.47, 114.52, 114.32, 69.33, 68.48, 59.91, 59.03, 52.75, 52.44, 47.35, 46.25, 32.28, 29.89, 27.61, 26.18, 24.69, 19.53, 19.45, 12.52, 12.33.

Synthesis of (1R,2S,5S)-3-(2-(2,4-dichlorophenoxy)acetyl)-6,6-dimethyl-3-azabicyclo[3.1.0]hexane-2-carboxylic acid (MPI55d). MPI55d was prepared as a white solid following a general procedure **B**. ^{1}H NMR (400 MHz, Methanol-d4) δ 7.30 (dd, J = 4.3, 2.6 Hz, 1H), 7.10 (dd, J = 8.9, 2.6 Hz, 1H), 6.83 (dd, J = 8.9, 6.9 Hz, 1H), 4.82 – 4.69 (m, 2H), 4.24 (s, 1H), 3.79 (dd, J = 10.6, 5.3 Hz, 1H), 3.65 – 3.48 (m, 1H), 1.49 (dd, J = 7.5, 5.2 Hz, 1H), 1.45 – 1.35 (m, 1H), 0.97 (d, J = 3.6 Hz, 3H), 0.87 (s, 2H), 0.81 (s, 1H). ^{13}C NMR (100 MHz, Methanol-d_4) δ 173.04, 166.78, 129.44, 127.41, 126.07, 123.24, 114.71, 67.18, 59.79, 48.29, 48.08, 47.87, 47.65, 47.44, 47.23, 47.01, 45.66, 29.95, 27.21, 25.07, 19.10, 11.54.

Methyl (S)-2-((1R,2S,5S)-3-(2-(2,4-dichlorophenoxy)acetyl)-6,6-dimethyl-3-azabicyclo[3.1.0]hexane-2-carboxamido)-3-((S)-2-oxopyrrolidin-3-yl)propanoate (MPI55e). MPI55e was prepared with Int.i and (MPI55d) as a white gummy solid following general procedure **C.** ^{1}H NMR (400 MHz, Chloroform-d) δ 7.27 (dd, J = 4.6, 2.5 Hz, 1H), 7.13 – 6.97 (m, 1H), 6.79 (dd, J = 22.5, 8.9 Hz, 1H), 4.65 – 4.55 (m, 2H), 4.51 – 4.39 (m, 1H), 4.34 – 4.28 (m, 1H), 3.87 – 3.68 (m, 2H), 3.65 (d, J = 11.1 Hz, 3H), 3.35 – 3.05 (m, 2H), 2.52 – 2.35 (m, 1H), 2.35 – 2.23 (m, 1H), 2.09 – 1.95 (m, 1H), 1.95 – 1.71 (m, 3H), 1.65 – 1.48 (m, 3H), 1.39 – 1.27 (m, 1H), 0.98 (d, J = 4.5 Hz, 3H), 0.81 (d, J = 10.9 Hz, 3H).

(1R,2S,5S)-3-(2-(2,4-Dichlorophenoxy)acetyl)-N-((S)-1-hydroxy-3-((S)-2-oxopyrrolidin-3-yl)propan-2-yl)-6,6-dimethyl-3-azabicyclo[3.1.0]hexane-2-carboxamide (MPI55f). MPI55f was prepared as a white solid following a general procedure **D** (yield 63%). ^{1}H NMR (400 MHz, Chloroform-d) δ 7.34 – 7.24 (m, 1H), 7.15 – 7.02 (m, 1H), 6.88 – 6.60 (m, 1H), 4.64 – 4.51 (m, 2H), 4.05 (dd, J = 5.1, 3.9 Hz, 1H), 4.00 – 3.76 (m, 3H), 3.70 – 3.43 (m, 5H), 3.32 – 3.08 (m, 2H), 2.48 – 2.32 (m, 1H), 2.34 – 2.17 (m, 1H), 2.03 – 1.84 (m, 1H), 1.82 – 1.63 (m, 2H), 1.59 – 1.49 (m, 1H), 0.98 (s, 3H), 0.80 (d, J = 14.5 Hz, 3H). ^{13}C NMR (100 MHz, Chloroform-d) δ 181.24, 171.79, 166.09, 152.43, 130.05, 127.70, 127.62, 126.60, 126.35, 123.61, 114.73, 114.64, 71.03, 68.13, 67.98, 65.19, 61.88, 61.15, 51.35, 46.57, 40.59, 38.21, 31.88, 30.78, 29.06, 27.61, 26.14, 25.62, 19.37, 12.66.

(2S,4S)-1-((Benzyloxy)carbonyl)-4-cyclohexylpyrrolidine-2-carboxylic acid (MPI56d). MPI56d was prepared as a white solid following a general procedure **G**. ^{1}H NMR (400 MHz, Chloroform-d) δ 7.43 – 7.28 (m, 5H), 5.37 – 5.04 (m, 2H), 4.46 (d, J = 8.9 Hz, 1H), 3.75 – 3.60 (m, 1H), 3.13 – 2.98 (m, 1H), 2.42 (dd, J = 12.8, 6.2 Hz, 1H), 2.05 (d, J = 7.4 Hz, 1H), 1.80 – 1.54 (m, 6H), 1.16 (dq, J = 16.7, 5.9 Hz, 5H), 1.03 – 0.82 (m, 2H).

(2S,4S)-Benzyl 4-cyclohexyl-2-(((S)-1-methoxy-1-oxo-3-((S)-2-oxopyrrolidin-3-yl)propan-2-yl)carbamoyl)pyrrolidine-1-carboxylate (MPI56e). MPI56e was prepared with **Int.i** and MPI56d as a white gummy solid following general procedure **C** (yield 60%). ^{1}H NMR (400 MHz, Chloroform-d) δ 7.74 (s, 0H), 7.54 (d, J = 7.2 Hz, 1H), 7.42 – 7.27 (m, 5H), 6.04 (dd, J = 54.4, 22.8 Hz, 1H), 5.14 (s, 2H), 4.55 (s, 1H), 4.47 – 4.32 (m, 1H), 3.85 – 3.58 (m, 5H), 3.31 – 3.21 (m, 2H), 2.52 – 2.01 (m, 5H), 1.90 – 1.53 (m, 9H), 1.26 – 1.06 (m, 5H), 1.03 – 0.85 (m, 2H).

(2S,4S)-Benzyl 4-cyclohexyl-2-(((S)-1-hydroxy-3-((S)-2-oxopyrrolidin-3-yl)propan-2-yl)carbamoyl)pyrrolidine-1-carboxylate (MPI56f). MPI56f was prepared as a white solid following a general procedure **D** (yield 59%). ^{1}H NMR (400 MHz, Chloroform-d) δ 7.80 (t, J = 8.4 Hz, 1H), 7.36 – 7.22 (m, 5H), 5.06 (d, J = 9.6 Hz, 2H), 4.39 – 4.16 (m, 1H), 4.00 – 3.81 (m, 1H), 3.74 (dd, J = 10.2, 7.7 Hz, 1H), 3.49 – 3.31 (m, 2H), 3.25 – 3.13 (m, 2H), 3.07 – 2.91 (m, 2H), 2.51 – 2.22 (m, 1H), 2.11 – 1.99 (m, 3H), 1.94 – 1.73 (m, 2H), 1.71 – 1.56 (m, 7H), 1.47 (ddd, J = 14.7, 10.8, 3.6 Hz, 1H), 1.27 – 1.09 (m, 5H), 1.00 – 0.88 (m, 2H).

Synthesis of 3-benzyl 2-methyl (1R,2S,5S)-6,6-dimethyl-3-azabicyclo[3.1.0]hexane-2,3-dicarboxylate (MPI57c). To a solution of methyl (1R,2S,5S)-6,6-dimethyl-3-azabicyclo[3.1.0]hexane-2-carboxylate (300 mg, 1.46 mmol) in dichloromethane (20 mL) was added benzyl chloroformate (300 mg, 0.25 mL, 1.75 mmol) dropwise, cooled to 0°C, followed by the addition of DIPEA (566 mg, 0.79 mL, 4.38 mmol). The reaction was allowed to stir at RT for overnight. The product was extracted with ethyl acetate (50 mL) and washed with saturated $NaHCO_3$ solution (2×20 mL), 1 M HCl solution (2×20 mL), and saturated brine solution (2×20 mL) sequentially. The organic layer was dried over anhydrous Na_2SO_4 and then concentrated on vacuo. The residue was then purified with flash chromatography (50-100% EtOAc in hexanes as the eluent) to afford **MPI57c** as white solid (380 mg, 77%). ^{1}H NMR (400 MHz, Chloroform-d) δ 7.24 – 7.15 (m, 5H), 5.13 – 4.86 (m, 3H), 4.16 (d, J = 23.4 Hz, 1H), 3.65 (d, J = 14.5 Hz, 3H), 3.43 (dd, J = 13.9, 10.9 Hz, 1H), 1.32 (d, J = 4.5 Hz, 3H), 0.95 (s, 4H), 0.87 (d, J = 1.9 Hz, 4H). ^{13}C NMR (100 MHz, Chloroform-d) δ 154.18, 153.60, 136.68, 136.58, 128.45, 128.39, 127.91,

127.63, 127.59, 66.96, 66.90, 59.87, 59.53, 52.31, 52.29, 52.16, 46.89, 46.34, 32.03, 31.05, 27.32, 26.48, 26.26, 26.25, 19.40, 19.36, 12.56.

Synthesis of (2S,4R)-1-((benzyloxy)carbonyl)-4-(tert-butoxy)pyrrolidine-2-carboxylic acid (MPI58d). MPI58d was prepared as a white solid following a general procedure **G**. ^{1}H NMR (400 MHz, Chloroform-d) δ 7.33 – 7.16 (m, 5H), 5.18 – 4.92 (m, 2H), 4.45 – 4.34 (m, 1H), 4.27 – 4.16 (m, 1H), 3.71 – 3.60 (m, 1H), 3.35 – 3.15 (m, 1H), 2.21 – 1.97 (m, 2H), 1.16 (t, J = 7.2 Hz, 1H), 1.09 (d, J = 2.1 Hz, 9H). ^{13}C NMR (100 MHz, Chloroform-d) δ 177.30, 176.38, 155.60, 154.47, 136.33, 136.30, 128.51, 128.40, 128.11, 127.89, 127.57, 74.30, 69.14, 68.48, 67.51, 67.27, 60.55, 57.92, 57.54, 53.82, 53.20, 38.49, 37.29, 28.23, 14.18.

Synthesis of benzyl (2S,4R)-4-(tert-butoxy)-2-(((S)-1-methoxy-1-oxo-3-((S)-2-oxopyrrolidin-3-yl)propan-2-yl)carbamoyl)pyrrolidine-1-carboxylate--methane (MPI58e). MPI58e was prepared with **Int.i** and MPI58d as a white gummy solid following general procedure **C** (yield 87%). ^{1}H NMR (400 MHz, DMSO-d6) δ 8.77 (dd, J = 4.4, 1.5 Hz, 1H), 8.62 – 8.49 (m, 2H), 7.62 (d, J = 3.5 Hz, 1H), 7.52 (dd, J = 8.4, 4.4 Hz, 1H), 7.42 – 7.22 (m, 5H), 5.13 – 4.92 (m, 2H), 4.42 – 4.22 (m, 3H), 3.65 – 3.57 (m, 4H), 3.23 – 3.02 (m, 3H), 2.16 – 1.86 (m, 5H), 1.66 – 1.47 (m, 2H), 1.26 (dd, J = 6.9, 4.5 Hz, 4H), 1.13 (d, J = 3.9 Hz, 9H). ^{13}C NMR (100 MHz, DMSO-d6) δ 178.57, 178.27, 172.80, 172.76, 172.72, 172.43, 162.78, 154.21, 151.50, 140.08, 137.46, 137.34, 135.10, 129.29, 128.84, 128.66, 128.23, 128.00, 127.82, 127.24, 121.15, 73.96, 73.93, 68.67, 66.29, 58.89, 58.49, 54.06, 52.42, 50.77, 42.31, 38.72, 38.36, 38.01, 37.93, 36.25, 32.88, 32.72, 31.24, 28.48, 27.45, 18.56, 17.20, 12.96.

Synthesis of benzyl (2S,4R)-4-(tert-butoxy)-2-(((S)-1-hydroxy-3-((S)-2-oxopyrrolidin-3-yl)propan-2-yl)carbamoyl)pyrrolidine-1-carboxylate--methane (MPI58f). MPI58f was prepared as a white solid following a general procedure **D**. Yield (59%). ^{1}H NMR (400 MHz, Chloroform-d) δ 7.42 (d, J = 7.7 Hz, 1H), 7.26 (d, J = 3.7 Hz, 5H), 6.04 (d, J = 11.2 Hz, 1H), 5.19 – 4.94 (m, 2H), 4.36 – 4.15 (m, 2H), 3.86 (d, J = 55.4 Hz, 1H), 3.73 – 3.52 (m, 2H), 3.50 – 3.31 (m, 2H), 3.22 (dd, J = 10.3, 4.2 Hz, 3H), 2.43 (s, 1H), 2.28 (s, 1H), 2.18 – 1.85 (m, 4H), 1.72 (p, J = 9.6 Hz, 2H), 1.51 (dd, J = 18.9, 10.4 Hz, 1H), 1.46 – 1.32 (m, 1H), 1.10 (s, 10H). ^{13}C NMR (100 MHz, Chloroform-d) δ 181.08, 172.94, 155.66, 154.88, 136.54, 128.49, 128.01, 127.73, 74.03, 69.41, 67.20, 65.38, 59.86, 53.61, 50.80, 40.55, 37.73, 31.86, 28.84, 28.27.

Synthesis of (1R,2S,5S)-3-((benzyloxy)carbonyl)-6,6-dimethyl-3-azabicyclo[3.1.0]hexane-2-carboxylic acid (MPI57d). MPI57d was prepared as a white solid following a general procedure **B**. ^{1}H NMR (400 MHz, Chloroform-d) δ 7.30 – 7.13 (m, 5H), 5.13 – 4.94 (m, 2H), 4.22 (s, 1H), 3.69 – 3.59 (m, 1H), 3.46 (dd, J = 15.5, 11.0 Hz, 1H), 1.46 (dd, J = 20.2, 7.4 Hz, 1H), 1.38 – 1.32 (m, 1H), 0.98 (d, J = 1.8 Hz, 3H), 0.89 (s, 3H). ^{13}C NMR (100 MHz, Chloroform-d) δ 177.88, 176.93, 154.75, 153.80, 136.40, 128.52, 128.43, 128.06, 127.90, 127.67, 127.50, 67.37, 67.19, 59.86, 59.34, 46.46, 32.00, 30.86, 27.25, 26.43, 26.30, 26.27, 19.54, 19.43, 12.59.

Synthesis of benzyl (1R,2S,5S)-2-((1-methoxy-1-oxo-3-(2-oxopyrrolidin-3-yl)propan-2-yl)carbamoyl)-6,6-dimethyl-3-azabicyclo[3.1.0]hexane-3-carboxylate (MPI57e). MPI56e was prepared with **Int.i** and MPI56d as a white gummy solid following general procedure **C** (yield 82%). ^{1}H NMR (400 MHz, Chloroform-d) δ 7.29 – 7.12 (m, 5H), 5.12 – 4.95 (m, 2H), 4.37 – 4.21 (m, 1H), 4.08 (d, J = 2.9 Hz, 1H), 3.79 – 3.61 (m, 3H), 3.61 – 3.38 (m, 3H), 3.30 – 3.05 (m, 2H), 2.48 – 1.89 (m, 4H), 1.88 – 1.60 (m, 2H), 1.53 – 1.26 (m, 3H), 0.96 (d, J = 1.7 Hz, 3H), 0.84 (d, J = 2.4 Hz, 3H). ^{13}C NMR (100 MHz, Chloroform-d) δ 179.87, 179.85, 172.64, 172.30, 172.10, 162.58, 154.52, 153.99, 136.72, 136.65, 128.46, 128.33, 127.92, 127.71, 127.53, 127.49, 67.05, 66.99, 61.27, 52.47, 52.37, 52.09, 51.35, 47.35, 38.63, 38.56, 36.51, 33.26, 32.80, 31.45, 31.19, 28.67, 26.40, 19.29, 19.14, 12.68, 12.60.

Synthesis of benzyl (1R,2S,5S)-2-((1-hydroxy-3-(2-oxopyrrolidin-3-yl)propan-2-yl)carbamoyl)-6,6-dimethyl-3-azabicyclo[3.1.0]hexane-3-carboxylate (MPI57f). MPI57f was prepared as a white solid following a general procedure **D** (yield 61%). ^{1}H NMR (400 MHz, Chloroform-d) δ 7.36 – 7.15 (m, 6H), 5.30 – 4.90 (m, 2H), 4.01 – 3.79 (m, 1H), 3.76 – 3.58 (m, 2H), 3.52 – 3.36 (m, 2H), 3.26 – 3.08 (m, 2H), 2.47 – 2.07 (m, 2H), 2.00 – 1.63 (m, 2H), 1.59 – 1.26 (m, 3H), 0.96 (s, 3H), 0.84 (d, J = 4.3 Hz, 3H). ^{13}C NMR (100 MHz, Chloroform-d) δ 181.08, 180.89, 173.46, 172.64, 154.68, 154.11, 136.56, 128.50, 128.47, 128.01, 127.99, 127.74, 127.60, 67.17, 67.07, 66.08, 65.42, 61.90, 51.43, 50.89, 47.34, 46.90, 40.60, 38.38, 38.16, 33.09, 31.95, 31.84, 31.64, 28.82, 28.74, 27.40, 26.23, 26.15, 19.27, 19.22, 12.66, 12.56.

(S)-N-((S)-1-Hydroxy-3-((S)-2-oxopyrrolidin-3-yl)propan-2-yl)-6-azaspiro[3.4]octane-7-carboxamide hydrogen chloride (MPI-59i-1). To a stirred solution of **YR-B-101c** (200 mg, 0.506 mmol) in 1,4-Dioxane (2 mL) at 0 °C was added 4N HCl (1.26 mL, 5.06 mmol). Reaction mixture was stirred at rt for 3 h. After completion of reaction, solvent was concentrated in a

vacuum. The residue was used in the next step without further purification. (150 mg). Crude product proceeded for next step without purification.

Benzyl (S)-7-(((S)-1-hydroxy-3-((S)-2-oxopyrrolidin-3-yl)propan-2-yl)carbamoyl)-6-azaspiro[3.4]octane-6-carboxylate (MPI59f). MPI59f was prepared by using procedure of **MPI57c.** Yield (54%). ^{1}H NMR (400 MHz, CDCl3) δ 7.36 (s, 5H), 5.67 (d, J = 28.6 Hz, 1H), 5.25 – 4.99 (m, 2H), 4.25 (dd, J = 8.1, 6.0 Hz, 1H), 4.11 – 3.70 (m, 2H), 3.53 (s, 2H), 3.42 (dd, J = 11.3, 5.0 Hz, 1H), 3.36 – 3.24 (m, 2H), 2.41 (s, 1H), 2.30 – 2.11 (m, 3H), 2.05 – 1.78 (m, 9H).

tert-Butyl 3-(((S)-1-methoxy-1-oxo-3-((S)-2-oxopyrrolidin-3-yl)propan-2-yl)carbamoyl)-2-azaspiro[4.4]nonane-2-carboxylate (MPI60e). MPI60e was prepared with **Int.i** and 2-(tert-butoxycarbonyl)-2-azaspiro[4.4]nonane-3-carboxylic acid as a white gummy solid following general procedure **C** (yield 69%). ^{1}H NMR (400 MHz, DMSO) δ 8.41 (dd, J = 19.5, 7.8 Hz, 1H), 7.64 (d, J = 34.9 Hz, 1H), 4.35 – 4.18 (m, 1H), 4.13 (t, J = 7.8 Hz, 1H), 3.62 (s, 3H), 3.25 (d, J = 10.8 Hz, 1H), 3.12 (td, J = 19.7, 9.1 Hz, 3H), 2.31 – 1.93 (m, 4H), 1.80 – 1.50 (m, 9H), 1.50 – 1.25 (m, 11H).

Benzyl 3-(((S)-1-methoxy-1-oxo-3-((S)-2-oxopyrrolidin-3-yl)propan-2-yl)carbamoyl)-2-azaspiro[4.4]nonane-2-carboxylate (MPI60e-1). MPI60e-1 was prepared with as a white gummy solid following general procedures **F** and **G** (yield 77%). ^{1}H NMR (400 MHz, DMSO) δ 8.50 (dd, J = 13.0, 7.8 Hz, 1H), 7.61 (s, 1H), 7.41 – 7.23 (m, 5H), 5.11 – 4.91 (m, 2H), 4.40 – 4.18 (m, 2H), 3.61 (d, J = 12.8 Hz, 3H), 3.37 (d, J = 10.2 Hz, 2H), 3.22 (t, J = 10.0 Hz, 1H), 3.15 – 3.03 (m, 1H), 2.20 – 1.86 (m, 4H), 1.75 (td, J = 13.2, 7.8 Hz, 1H), 1.64 – 1.39 (m, 10H).

Benzyl 3-(((S)-1-hydroxy-3-((S)-2-oxopyrrolidin-3-yl)propan-2-yl)carbamoyl)-2-azaspiro[4.4]nonane-2-carboxylate (MPI60f). MPI60f was prepared as a white solid following a general procedure **D**. Yield (58%). ^{1}H NMR (400 MHz, $CDCl_3$) δ 7.79 (d, J = 6.9 Hz, 1H), 7.31 – 7.16 (m, 5H), 6.15 (d, J = 52.2 Hz, 1H), 5.16 – 4.91 (m, 2H), 4.20 (t, J = 7.8 Hz, 1H), 3.88 (d, J = 55.0 Hz, 1H), 3.63 – 3.12 (m, 6H), 2.44 – 2.03 (m, 3H), 1.94 (d, J = 7.6 Hz, 2H), 1.85 – 1.31 (m, 10H).

tert-Butyl 3-(((S)-1-methoxy-1-oxo-3-((S)-2-oxopyrrolidin-3-yl)propan-2-yl)carbamoyl)-2-azaspiro[4.5]decane-2-carboxylate (MPI61e). MPI61e was prepared with **Int.i** and 2-(tert-butoxycarbonyl)-2-azaspiro[4.5]decane-3-carboxylic acid a white gummy solid following general procedure **C** (yield 75%). ^{1}H NMR (400 MHz, $CDCl_3$) δ 6.38 (d, J = 141.5 Hz, 1H), 4.46 (d, J = 60.3 Hz, 1H), 4.18 (dd, J = 8.5, 7.3 Hz, 1H), 3.65 (d, J = 2.7 Hz, 3H), 3.33 – 3.21 (m, 2H), 3.14 –

2.99 (m, 1H), 2.48 – 2.27 (m, 2H), 2.11 (ddd, J = 13.2, 10.5, 4.8 Hz, 2H), 1.82 (dp, J = 11.5, 4.1 Hz, 3H), 1.35 (d, J = 18.7 Hz, 19H).

Benzyl 3-(((S)-1-methoxy-1-oxo-3-((S)-2-oxopyrrolidin-3-yl)propan-2-yl)carbamoyl)-2-azaspiro[4.5]decane-2-carboxylate (MPI61e-1). MPI61e-1 was prepared with as a white gummy solid following general procedures **F** and **G** (yield 90%). ^{1}H NMR (400 MHz, DMSO-d_6) δ 8.57 (ddd, J = 20.3, 10.2, 7.2 Hz, 1H), 7.70 (dd, J = 12.9, 4.7 Hz, 1H), 7.49 – 7.30 (m, 6H), 5.14 (q, J = 6.3, 4.8 Hz, 1H), 5.13 – 4.98 (m, 1H), 4.46 – 4.23 (m, 2H), 3.73 – 3.65 (m, 2H), 3.63 (s, 1H), 3.56 – 3.47 (m, 1H), 3.31 – 3.17 (m, 1H), 3.20 – 3.13 (m, 1H), 3.15 – 2.89 (m, 1H), 2.17 (s, 2H), 2.28 – 2.02 (m, 1H), 1.75 – 1.57 (m, 2H), 1.66 (s, 2H), 1.51 (d, J = 17.1 Hz, 5H), 1.42 (d, J = 14.5 Hz, 8H). ^{13}C NMR (101 MHz, DMSO) δ 22.04, 22.59, 24.93, 33.71, 34.57, 36.95, 37.61, 40.14, 40.99, 49.41, 51.28, 57.64, 65.17, 126.06, 126.64, 126.84, 127.55, 136.34, 153.33, 153.44, 171.66, 177.31.

Benzyl 3-(((S)-1-hydroxy-3-((S)-2-oxopyrrolidin-3-yl)propan-2-yl)carbamoyl)-2-azaspiro[4.5]decane-2-carboxylate (MPI61f). MPI61f was prepared as a white solid following a general procedure **D**. Yield (52%). ^{1}H NMR (400 MHz, CDCl3) δ 7.33-7.19 (m, 5H), 6.40-6.06 (m, 1H), 5.16 – 4.87 (m, 2H), 4.29-4.13 (m, 1H), 3.98-3.75 (m, 1H), 3.65 – 3.05 (m, 6H), 2.48 – 2.21 (m, 1H), 2.21 – 1.60 (m, 6H), 1.48 – 1.16 (m, 10H).

Synthesis of methyl (1R,2S,5S)-3-((4-chlorophenyl)glycyl)-6,6-dimethyl-3-azabicyclo[3.1.0]hexane-2-carboxylate (MPI62c). MPI62c was prepared as a white solid following a general procedure **A**. Yield (69%). ^{1}H NMR (400 MHz, Chloroform-d) δ 7.12 – 6.94 (m, 2H), 6.50 – 6.35 (m, 2H), 3.83 – 3.75 (m, 1H), 3.75 – 3.67 (m, 5H), 1.56 – 1.46 (m, 1H), 1.46 – 1.34 (m, 1H), 1.01 (d, J = 3.6 Hz, 3H), 0.87 (d, J = 14.6 Hz, 3H).

Synthesis of (1R,2S,5S)-3-((4-chlorophenyl)glycyl)-6,6-dimethyl-3-azabicyclo[3.1.0]hexane-2-carboxylic acid (MPI62d). To a stirred solution of 2 (300 mg, 0.1 mmol) in 1,4-dioxane (8 mL) was added a 4 M HCl solution in dioxane (8 mL). The reaction mixture was stirred at rt for 1 h and then concentrated in vacuo to get product **MPI62d**. ^{1}H NMR (400 MHz, DMSO-d6) δ 7.07 (dd, J = 8.9, 2.4 Hz, 2H), 6.67 – 6.53 (m, 2H), 5.95 – 5.80 (m, 1H), 3.87 (d, J = 5.4 Hz, 1H), 3.63 (s, 2H), 1.63 – 1.53 (m, 1H), 1.41 (dd, J = 7.5, 3.4 Hz, 1H), 1.35 (d, J = 3.9 Hz, 1H), 1.27 – 1.15 (m, 1H), 1.03 (d, J = 2.0 Hz, 3H), 0.89 (d, J = 9.8 Hz, 3H).

Synthesis of tert-butyl (S)-6-(((S)-1-methoxy-1-oxo-3-((S)-2-oxopyrrolidin-3-yl)propan-2-yl)carbamoyl)-5-azaspiro[2.4]heptane-5-carboxylate (MPI63c). **MPI63c** was prepared with

(S)-5-(tert-butoxycarbonyl)-5-azaspiro[2.4]heptane-6-carboxylic acid (MPI63a) and Int.i as a white solid following a general procedure **C** (yield 82%).

Synthesis of methyl (S)-3-((S)-2-oxopyrrolidin-3-yl)-2-((S)-5-azaspiro[2.4]heptane-6-carboxamido)propanoate (MPI63i). **MPI63i** was prepared as a white solid following a general procedure **F**.

Synthesis of methyl (S)-2-((S)-5-(2-(2,4-dichlorophenoxy)acetyl)-5-azaspiro[2.4]heptane-6-carboxamido)-3-((S)-2-oxopyrrolidin-3-yl)propanoate (MPI63e). MPI63e was prepared with 2-(2,4-dichlorophenoxy)acetic acid and Int.i as a white solid following a general procedure **C** (yield 44%). ^{1}H NMR (400 MHz, Chloroform-d) δ 7.28 (dd, J = 5.4, 2.5 Hz, 1H), 6.86 (d, J = 8.9 Hz, 1H), 4.92 – 4.25 (m, 4H), 3.64 (d, J = 8.9 Hz, 3H), 3.32 – 3.13 (m, 2H), 2.52 – 2.35 (m, 1H), 2.35 – 2.19 (m, 1H), 2.19 – 1.92 (m, 2H), 1.92 – 1.63 (m, 4H), 1.48 – 1.24 (m, 2H), 0.70 – 0.52 (m, 3H), 0.52 – 0.36 (m, 1H).

Synthesis of (S)-5-(2-(2,4-dichlorophenoxy)acetyl)-N-((S)-1-hydroxy-3-((S)-2-oxopyrrolidin-3-yl)propan-2-yl)-5-azaspiro[2.4]heptane-6-carboxamide (MPI63f). **MPI63f** was prepared as a white solid following a general procedure **D**. (Yield 68%). ^{1}H NMR (400 MHz, Chloroform-d) δ 7.91 (dd, J = 7.3, 3.5 Hz, 1H), 7.28 (t, J = 2.3 Hz, 1H), 7.14 – 7.00 (m, 1H), 6.87 (d, J = 8.8 Hz, 1H), 4.79 – 4.65 (m, 1H), 4.62 – 4.46 (m, 1H), 3.93 – 3.78 (m, 1H), 3.71 – 3.58 (m, 1H), 3.58 – 3.33 (m, 3H), 3.32 – 3.14 (m, 2H), 2.51 – 2.22 (m, 3H), 2.16 (dd, J = 12.8, 8.6 Hz, 1H), 2.01 – 1.91 (m, 1H), 1.91 – 1.81 (m, 1H), 1.81 – 1.71 (m, 1H), 1.55 (ddt, J = 19.3, 14.5, 4.6 Hz, 2H), 1.45 – 1.32 (m, 2H), 1.19 (d, J = 1.7 Hz, 1H), 0.64 – 0.43 (m, 4H).

Methyl (1*R*,2*S*,5*S*)-3-(2-(cyclohexyloxy)acetyl)-6,6-dimethyl-3-azabicyclo[3.1.0]hexane-2-carboxylate (MPI64c). MPI64c was prepared as a white solid following a general procedure **A**. Yield (67%). ^{1}H NMR (400 MHz, DMSO) δ 4.21 – 3.81 (m, 3H), 3.77 – 3.63 (m, 4H), 3.58 – 3.44 (m, 1H), 3.31 – 3.19 (m, 1H), 1.90 – 1.74 (m, 2H), 1.72 – 1.59 (m, 2H), 1.58 – 1.51 (m, 1H), 1.50 – 1.37 (m, 2H), 1.20 (tq, *J* = 9.8, 3.1 Hz, 5H), 1.02 (s, 3H), 0.88 (d, *J* = 4.6 Hz, 3H).

(1*R*,2*S*,5*S*)-3-(2-(Cyclohexyloxy)acetyl)-6,6-dimethyl-3-azabicyclo[3.1.0]hexane-2-carboxylic acid (MPI64d). MPI64d was prepared with as a white gummy solid following general procedure **B**. ^{1}H NMR (400 MHz, $CDCl_3$) δ 4.64-4,32(m, 1H), 4.09 – 3.88 (m, 2H), 3.80 – 3.52 (m, 2H), 3.34-3,15 (m, 1H), 1.90 – 1.76 (m, 2H), 1.64 (dd, *J* = 9.0, 6.2 Hz, 2H), 1.49 – 1.39 (m, 2H), 1.32 – 1.07 (m, 6H), 1.00 (s, 3H), 0.88 (s, 3H).

Methyl (*S*)-2-((1*R*,2*S*,5*S*)-3-(2-(cyclohexyloxy)acetyl)-6,6-dimethyl-3-azabicyclo[3.1.0]hexane-2-carboxamido)-3-((*S*)-2-oxopyrrolidin-3-yl)propanoate (MPI64e). **MPI64e** was prepared with MPI64d and Int.i as a white solid following a general procedure **C** (yield 75%). ^{1}H NMR (400 MHz, $CDCl_3$) δ 8.81 – 8.19 (m, 1H), 7.67-7.24 (m, 1H), 4.53 – 4.25 (m, 2H), 4.05 – 3.95 (m, 2H), 3.77 (dd, *J* = 10.6, 5.1 Hz, 1H), 3.72 – 3.68 (m, 1H), 3.66 (s, 3H), 3.33 – 3.20 (m, 3H), 2.39-2.30 (m, 1H), 2.17 – 2.07 (m, 1H), 1.88-1.80 (m, 3H), 1.49 – 1.43 (m, 2H), 1.31 – 1.07 (m, 9H), 0.98 (s, 3H), 0.85 (s, 3H).

methyl (1R,2S,5S)-3-(3-cyclohexylpropanoyl)-6,6-dimethyl-3-azabicyclo[3.1.0]hexane-2-carboxylate (MPI65c). **MPI65c** was prepared as a white solid following a general procedure **A**. Yield (88%). ^{1}H NMR (400 MHz, $CDCl_3$) δ 4.38 (s, 1H), 3.82 (dd, *J* = 10.1, 5.3 Hz, 1H), 3.75 (s, 3H), 3.48 (d, *J* = 10.1 Hz, 1H), 2.29 – 2.19 (m, 2H), 1.74 – 1.58 (m, 5H), 1.57 – 1.44 (m, 3H), 1.41 (d, *J* = 7.4 Hz, 1H), 1.31 – 1.09 (m, 5H), 1.05 (s, 3H), 0.95 (s, 3H), 0.92 – 0.81 (m, 2H).

(1R,2S,5S)-3-(3-Cyclohexylpropanoyl)-6,6-dimethyl-3-azabicyclo[3.1.0]hexane-2-carboxylic acid (MPI65d). **MPI65d** was prepared as a white solid following a general procedure **B**.

methyl (S)-2-((1R,2S,5S)-3-(3-Cyclohexylpropanoyl)-6,6-dimethyl-3-azabicyclo[3.1.0]hexane-2-carboxamido)-3-((S)-2-oxopyrrolidin-3-yl)propanoate (MPI65e). **MPI65e** was prepared with MPI65d and Int.i as a white solid following a general procedure **C** (yield 73%).^{1}H NMR (400 MHz, $CDCl_3$) δ 7.59 (d, *J* = 7.2 Hz, 1H), 5.92 (s, 1H), 4.58 (ddd, *J* = 11.0, 7.2, 4.2 Hz, 1H), 4.33 (s, 1H), 3.85 (dd, *J* = 10.3, 5.3 Hz, 1H), 3.75 (s, 3H), 3.54 – 3.47 (m, 1H), 3.44 – 3.32 (m, 2H), 2.44 (td, *J* = 7.9, 3.9 Hz, 1H), 2.31 – 2.11 (m, 3H), 2.02 – 1.81 (m, 2H), 1.69 (t, *J* = 9.8 Hz, 4H), 1.58 (d, *J* = 7.6 Hz, 1H), 1.32 – 1.11 (m, 4H), 1.07 (s, 3H), 0.95 (s, 3H), 0.88 (d, *J* = 11.7 Hz, 2H).

(1R,2S,5S)-3-(3-Cyclohexylpropanoyl)-N-((S)-1-hydroxy-3-((S)-2-oxopyrrolidin-3-yl)propan-2-yl)-6,6-dimethyl-3-azabicyclo[3.1.0]hexane-2-carboxamide (MPI65f). **MPI65f** was prepared as a white solid following a general procedure **D**. (Yield 66%). ^{1}H NMR (400 MHz, $CDCl_3$) δ 7.56 (d, *J* = 7.2 Hz, 1H), 5.93 (d, *J* = 32.5 Hz, 1H), 4.25 (s, 1H), 3.98 (tt, *J* = 7.2, 4.0 Hz, 1H), 3.90 (dd, *J* = 10.3, 5.3 Hz, 1H), 3.76 (ddd, *J* = 11.6, 3.9, 2.2 Hz, 1H), 3.54 – 3.43 (m, 2H), 3.33 (dd, *J* = 9.2, 4.4 Hz, 2H), 2.55 – 2.47 (m, 1H), 2.44 – 2.35 (m, 1H), 2.24 (dq, *J* = 18.2, 7.5 Hz, 2H), 2.03 (ddd, *J* = 14.5, 10.7, 6.6 Hz, 1H), 1.89 – 1.74 (m, 1H), 1.70 – 1.59 (m, 6H), 1.53 – 1.44 (m, 4H), 1.18 (tdd, *J* = 20.8, 12.4, 9.4 Hz, 5H), 1.04 (d, *J* = 2.4 Hz, 3H), 0.91 (s, 3H), 0.88 – 0.78 (m, 2H).

tert-Butyl 3-(((S)-1-amino-1-oxo-3-((S)-2-oxopyrrolidin-3-yl)propan-2-yl)carbamoyl)-2-azaspiro[4.4]nonane-2-carboxylate (MPI66-1h). **MPI66-1h** was prepared with MPI66-1g and

Int.ii as a white solid following a general procedure **C** (yield 73%).. ^{1}H NMR (400 MHz, DMSO) δ 8.22 – 7.88 (m, 1H), 7.62 (d, J = 12.6 Hz, 1H), 7.24 (d, J = 44.3 Hz, 1H), 7.05 (s, 1H), 4.29 – 4.18 (m, 1H), 4.18 – 4.05 (m, 1H), 3.30 – 3.04 (m, 4H), 2.40 – 1.90 (m, 4H), 1.78 – 1.41 (m, 10H), 1.33 (t, J = 20.8 Hz, 9H).

N-((S)-1-amino-1-oxo-3-((S)-2-oxopyrrolidin-3-yl) propan-2-yl)-2-azaspiro[4.4]nonane-3-carboxamide (MPI66-1i). MPI66-1i was prepared as a white solid following a general procedure **F** (Yield 80%).

Benzyl3-(((S)-1-amino-1-oxo-3-((S)-2-oxopyrrolidin-3-yl)propan-2-yl)carbamoyl)-2-azaspiro[4.4]nonane-2-carboxylate (MPI66-1k). MPI66-1k was prepared as a white solid following a general procedure **G** (Yield 75%). ^{1}H NMR (400 MHz, DMSO) δ 8.28 – 8.09 (m, 1H), 7.56 (t, J = 14.3 Hz, 1H), 7.41 – 7.17 (m, 5H), 7.03 (d, J = 16.2 Hz, 1H), 5.09 – 4.91 (m, 2H), 4.39 – 4.17 (m, 2H), 3.32 – 2.80 (m, 4H), 2.39 – 2.28 (m, 1H), 2.21 – 1.88 (m, 3H), 1.73 (dt, J = 19.2, 6.1 Hz, 1H), 1.65 – 1.34 (m, 10H).

3-Chlorobenzyl 3-(((S)-1-amino-1-oxo-3-((S)-2-oxopyrrolidin-3-yl)propan-2-yl)carbamoyl)-2-azaspiro[4.4]nonane-2-carboxylate (MPI66-2k). To 3-chlorobenzyl alcohol (0.3 g, 2.104 mmol) in CH_3CN (10 mL) were added DIPEA (1.1 mL, 6.311 mmol) and N,N'-disuccinimidyl carbonate (753 mg, 2.94 mmol) at 0 °C. After 10 h at rt, **MPI66-2i** (750 mg, 2.104 mmol) was added one portion at 0 °C. After 10 h at rt, the reaction mixture was evaporated in vacuo. Purification by silica gel chromatography (Dichloromethane/MeOH = 9:1). 350 mg of compound isolated. Yield 50%. ^{1}H NMR (400 MHz, DMSO) δ 8.37 – 8.10 (m, 1H), 7.72 – 7.52 (m, 1H), 7.43 – 6.97 (m, 5H), 5.13 – 4.90 (m, 2H), 4.46 – 4.17 (m, 2H), 3.38 (t, *J* = 11.3 Hz, 1H), 3.20 (d, *J* = 10.7 Hz, 1H), 3.16 – 2.89 (m, 2H), 2.13 (ddd, *J* = 25.8, 12.5, 7.8 Hz, 2H), 1.84 – 1.24 (m, 13H).

N-((S)-1-Hydroxy-3-((S)-2-oxopyrrolidin-3-yl)propan-2-yl)-2-(4-methoxy-1H-indole-2-carbonyl)-2-azaspiro[4.4]nonane-3-carboxamide (MPI66-3f). MPI66-3f was prepared by **4-methoxy-1H-indole-2-carboxylic acid** (0.345 mmol, 66 mg) and **N-((S)-1-hydroxy-3-((S)-2-oxopyrrolidin-3-yl)propan-2-yl)-2-azaspiro[4.4]nonane-3-carboxamide** (0.345 mmol, 120 mg) in general procedure **C** (Yield 36%). ^{1}H NMR (400 MHz, $CDCl_3$) δ 10.95 (s, 0.5H), 10.14 (s, 0.5H), 7.65 (s, 1H), 7.19 – 6.83 (m, 3H), 6.46 (d, *J* = 7.7 Hz, 1H), 4.64 (d, *J* = 67.9 Hz, 1H), 4.19 – 4.06 (m, 1H), 3.95 (d, *J* = 5.8 Hz, 3H), 3.91 – 3.76 (m, 2H), 3.68 (d, *J* = 16.7 Hz, 1H), 3.51 (s, 1H), 3.14 (s, 1H), 2.93 (s, 1H), 2.58 – 2.31 (m, 2H), 2.27 – 1.91 (m, 3H), 1.80 – 1.23 (m, 10H).

tert-Butyl 3-(((S)-1-amino-1-oxo-3-((S)-2-oxopiperidin-3-yl)propan-2-yl)carbamoyl)-2-azaspiro[4.4]nonane-2-carboxylate (MPI66-4h). MPI66-4h was prepared with MPI66-4g and Int.ii as a white solid following a general procedure **C** (yield 82%).. ^{1}H NMR (400 MHz, $CDCl_3$) δ 4.33 (s, 1H), 4.13 (d, *J* = 9.0 Hz, 1H), 3.24 (h, *J* = 11.3 Hz, 4H), 2.37 – 1.99 (m, 3H), 1.96 – 1.71 (m, 4H), 1.68 – 1.29 (m, 19H).

N-((S)-1-Amino-1-oxo-3-((S)-2-oxopiperidin-3-yl)propan-2-yl)-2-azaspiro[4.4]nonane-3-carboxamide hydrogen chloride (MPI66-4i). MPI66-4i was prepared as a white solid following a general procedure **F** (150 mg).

N-((S)-1-Amino-1-oxo-3-((S)-2-oxopiperidin-3-yl)propan-2-yl)-2-(4-methoxy-1H-indole-2-carbonyl)-2-azaspiro[4.4]nonane-3-carboxamide (MPI66-4k). MPI66-4k was prepared with MPI66-4i and **4-methoxy-1H-indole-2-carboxylic acid** as a white solid following a general procedure **C** (yield 39%).. ^{1}H NMR (400 MHz, DMSO) δ 11.57 (s, 1H), 8.43 (d, *J* = 8.5 Hz, 1H), 7.59 (s, 1H), 7.26 (s, 1H), 7.22 – 7.09 (m, 2H), 7.04 (d, *J* = 8.3 Hz, 1H), 6.93 (s, 1H), 6.53 (d, *J* = 7.7 Hz, 1H), 4.55 (dd, *J* = 9.7, 7.0 Hz, 1H), 4.28 – 4.13 (m, 1H), 3.89 (s, 3H), 3.87 – 3.79 (m, 2H), 3.20 – 3.04 (m, 2H), 2.24 – 2.04 (m, 3H), 2.01 – 1.75 (m, 3H), 1.63 (td, *J* = 7.1, 4.2 Hz, 7H), 1.51 – 1.23 (m, 4H).

Benzyl 3-(((S)-1-amino-1-oxo-3-((S)-2-oxopyrrolidin-3-yl)propan-2-yl)carbamoyl)-2-azaspiro[4.5]decane-2-carboxylate (MPI67k). MPI67k was prepared as a white solid following a general procedure **G** (Yield 79%). ^{1}H NMR (400 MHz, CDCl3) δ 8.46 (d, J = 6.0 Hz, 1H), 7.31 – 7.22 (m, 5H), 7.15 (s, 1H), 6.15 (s, 1H), 5.42 (d, J = 11.8 Hz, 1H), 5.15-5.00 (m, 2H), 4.25 – 4.20 (m, 1H), 3.72 – 3.55 (m, 1H), 3.48 (dd, J = 18.8, 10.0 Hz, 1H), 3.28 (d, J = 8.6 Hz, 2H), 3.16-3.04 (m, 1H), 2.14 (dd, J = 12.7, 8.0 Hz, 2H), 2.10 – 1.96 (m, 2H), 1.95-1.75 (m, 2H), 1.71 – 1.54 (m, 2H), 1.46 – 1.27 (m, 12H).

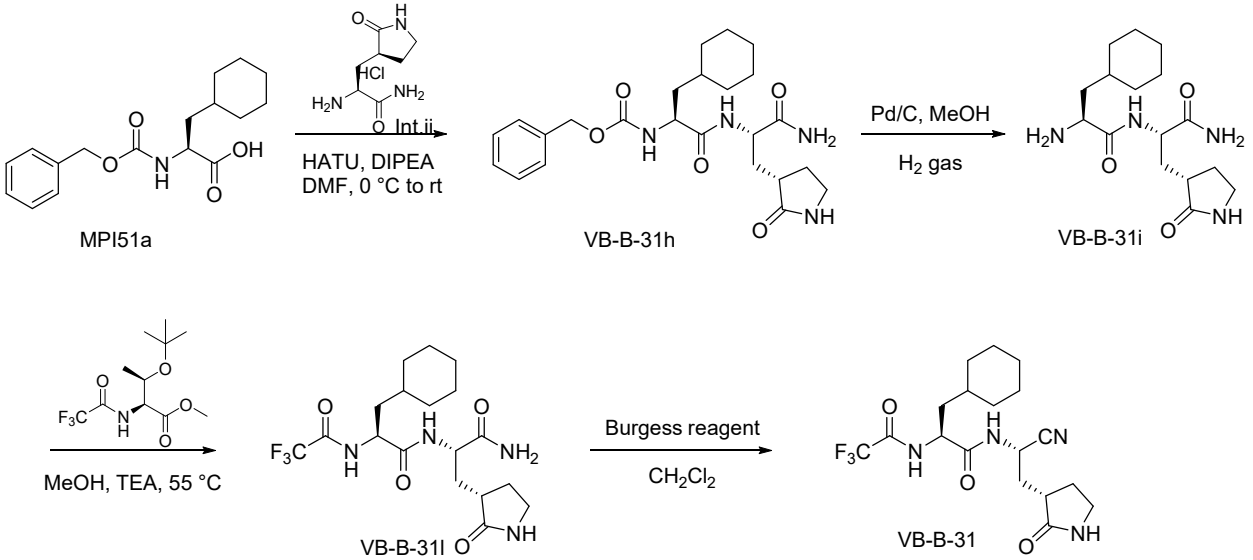

Benzyl ((*S*)-1-(((*S*)-1-amino-1-oxo-3-((*S*)-2-oxopyrrolidin-3-yl)propan-2-yl)amino)-3-cyclohexyl-1-oxopropan-2-yl)carbamate (VB-B-31h). VB-B-31h was prepared with MPI51a and Int.ii as a white solid following a general procedure **C** (yield 82%).^{1}H NMR (400 MHz, $CDCl_3$) δ 8.24 (d, *J* = 6.8 Hz, 1H), 7.31 – 7.17 (m, 5H), 6.97 (s, 1H), 6.74 (s, 1H), 6.10 (s, 1H), 5.92 (d, *J* = 7.3 Hz, 1H), 5.08 – 4.93 (m, 2H), 4.38 (dt, *J* = 10.1, 6.2 Hz, 1H), 4.23 – 4.07 (m, 1H), 3.24-3.08 (m, 2H), 2.31-2.10 (m, 2H), 2.03 – 1.79 (m, 2H), 1.78 – 1.47 (m, 7H), 1.46-1.22 (m, 2H), 1.08 (p, *J* = 11.6 Hz, 3H), 0.93 – 0.68 (m, 2H). ^{13}C NMR (101 MHz, $CDCl_3$) δ 180.70, 174.41, 173.53, 156.64, 136.38, 128.53, 128.14, 127.96, 66.96, 53.58, 52.43, 40.73, 39.96, 38.49, 34.07, 33.75, 32.80, 32.29, 28.46, 26.22, 26.03.

Methyl *O*-(*tert*-butyl)-*N*-(2,2,2-trifluoroethanethioyl)-*L*-threoninate (VB-B-31i).

To a solution of **VB-B-31h** (250 mg, 0.47 mmol) in methanol (10 mL) was added 10% Pd/C (50 mg). The reaction mixture was stirred under H_2 balloon at rt for 3 h. The reaction mixture was filtered with celite, and the filtrate was concentrated *in vacuo* to yield **VB-B-31h** as colorless oil (168 mg, 90%), which was used without further purification. ^{1}H NMR (400 MHz, $CDCl_3$) δ 8.45 (s, 1H), 4.98 – 4.77 (m, 1H), 4.30 (qd, *J* = 6.3, 1.8 Hz, 1H), 3.69 (s, 3H), 1.15 (d, *J* = 6.4 Hz, 3H), 1.08 (s, 9H). ^{13}C NMR (101 MHz, $CDCl_3$) δ 184.85, 184.49, 168.63, 118.77, 115.99, 75.02, 67.14, 63.00, 52.71, 28.23, 21.43.

(*S*)-*N*-((*S*)-1-amino-1-oxo-3-((*S*)-2-oxopyrrolidin-3-yl)propan-2-yl)-3-cyclohexyl-2-(2,2,2-trifluoroethanethioamido)propenamide (VB-B-31l). methyl O-(tert-butyl)-N-(2,2,2-trifluoroacetyl)-L-threoninate (1.5 eq) and VB-B-31i (1 eq) in methanol was added TEA (2.5 eq) stirred at 55 °C for 48 h. Remove the solvent by rotavapor and work up with ethyl acetate. Purified

by silics gel column chromatography. ^{1}H NMR (400 MHz, DMSO) δ 8.52 – 8.28 (m, 1H), 7.67 (s, 1H), 7.36 (d, *J* = 5.5 Hz, 1H), 7.09 (s, 1H), 4.95 (dd, *J* = 11.1, 4.1 Hz, 1H), 4.30 (ddd, *J* = 11.8, 8.2, 4.1 Hz, 1H), 3.29 – 3.01 (m, 3H), 2.35 (t, *J* = 10.8 Hz, 1H), 2.14 – 1.94 (m, 2H), 1.74 – 1.66 (m, 6H), 1.59 – 1.51 (m, 1H), 1.30 (s, 1H), 1.25 – 1.11 (m, 5H), 1.00 – 0.88 (m, 2H).

tert-Butyl (S)-7-(((S)-1-methoxy-1-oxo-3-((S)-2-oxopyrrolidin-3-yl)propan-2-yl)carbamoyl)-6-azaspiro[3.4]octane-6-carboxylate (YR-B-101e). YR-B-101e was prepared by **(S)-6-(tert-butoxycarbonyl)-6-azaspiro[3.4]octane-7-carboxylic acid** and **Int.i** using general procedure **C**. (Yield 79%). ^{1}H NMR (400 MHz, $CDCl_3$) δ 4.51 (d, *J* = 54.1 Hz, 1H), 4.22 (t, *J* = 6.7 Hz, 1H), 3.72 (s, 3H), 3.40 (dd, *J* = 15.8, 8.3 Hz, 4H), 2.43 (s, 2H), 2.15 (dd, *J* = 17.5, 7.7 Hz, 3H), 1.99 – 1.77 (m, 8H), 1.44 (s, 9H).

tert-Butyl (S)-7-(((S)-1-hydroxy-3-((S)-2-oxopyrrolidin-3-yl)propan-2-yl)carbamoyl)-6-azaspiro[3.4]octane-6-carboxylate (Yr-B-101f). MPI101f was prepared as a white solid following a general procedure **D** (Yield 62%). ^{1}H NMR (400 MHz, $CDCl_3$) δ 4.18 (ddd, *J* = 8.2, 5.6, 2.2 Hz, 1H), 4.02 (s, 1H), 3.80 – 3.23 (m, 6H), 2.37 (s, 2H), 2.24 – 1.73 (m, 11H), 1.44 (s, 9H).

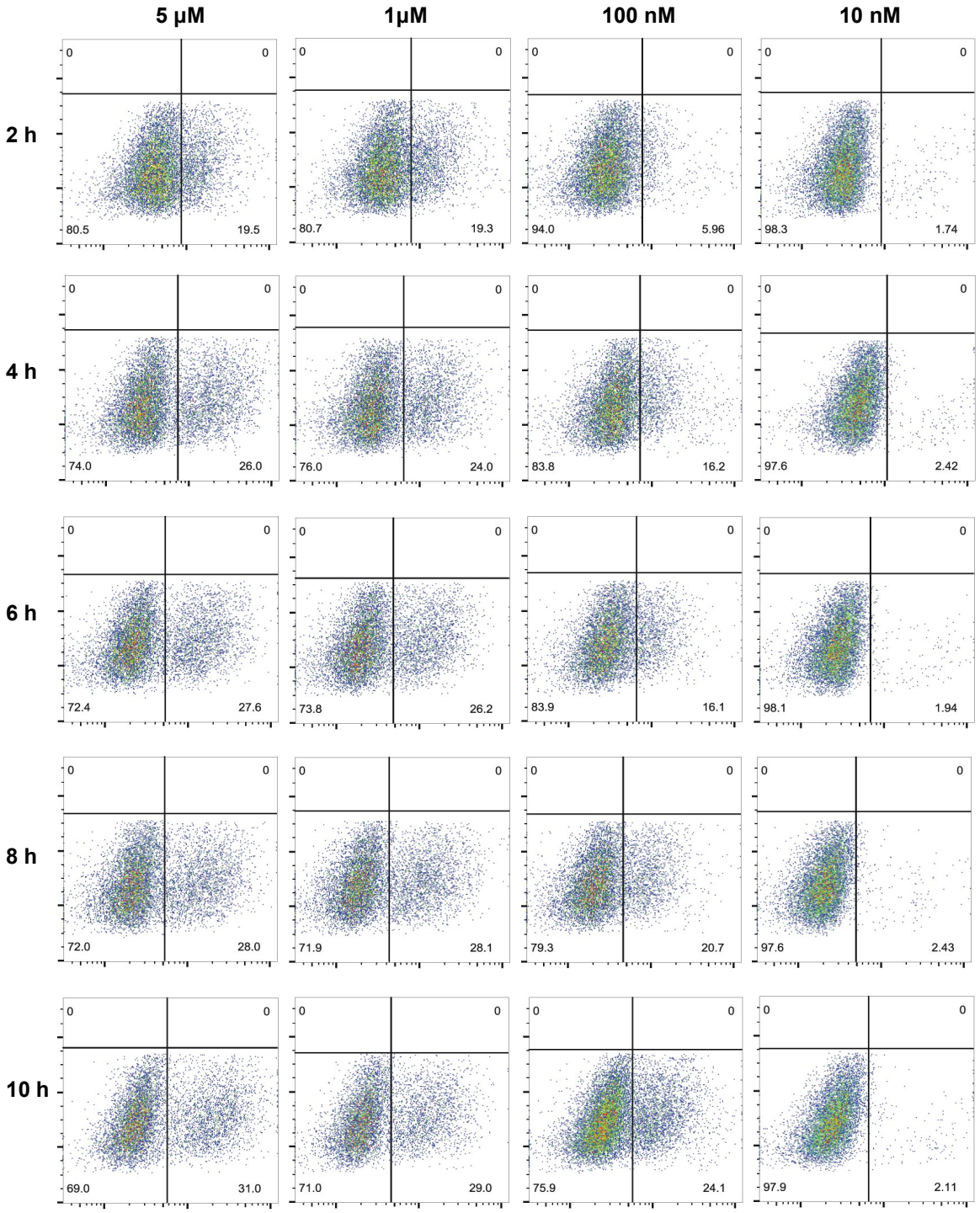

Figure S9. Flow cytometry results of full-length sCAR19 display on T cells at different timepoints and ASV concentration. Alexa Fluor 647-anti-mouse F(ab)2 antibody was used

for the detection of full-length sCAR19 display. The bottom right section of each dot plot shows cells with expressed full-length sCAR19.

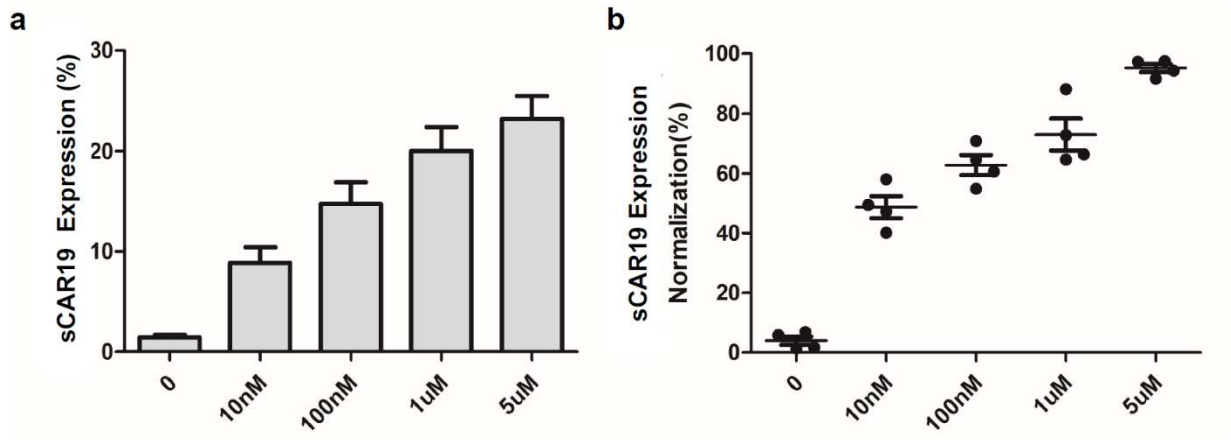

Figure S10. Dose-dependent full-length sCAR19 display on T cells. a. Full-length sCAR19 levels on T cells in the presence of 0, 10 nM, 100 nM, 1 μM and 5 µM ASV at the 10 h time point. b. The displayed full-length sCAR19 on T cells after normalization in the presence of 5µM ASV at the 24 h time point.

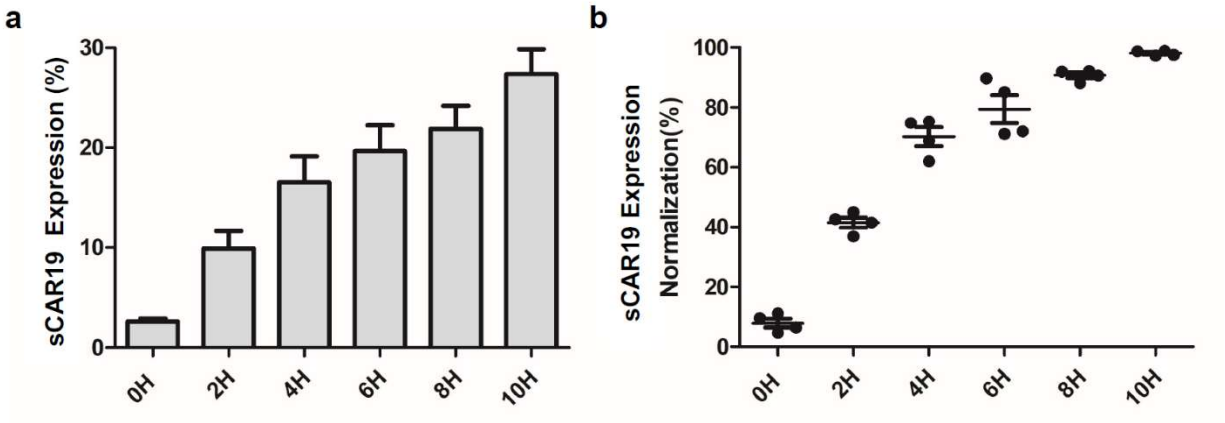

Figure S11. Time-dependent full-length sCAR19 display on the T cell surface in the presence of ASV. a. Full-length sCAR19 levels on the T cell surface at 0, 2, 4, 6, 8 and 10 h time points after the addition of 5 µM ASV. b. Displayed sCAR19 levels after normalization in the presence of 5 µM ASV at different time points.

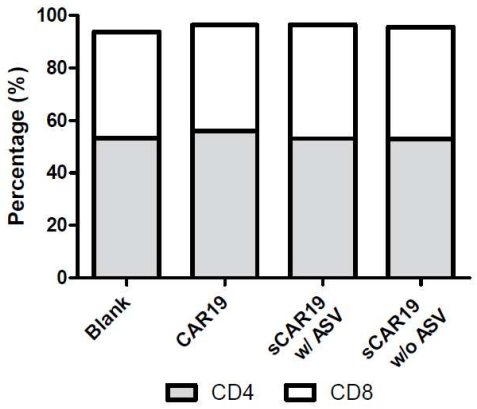

Figure S12 Subsets of sCAR19 T cells. Four groups T cells were cultured with or without 5 μM ASV for 72 h. CD4 and CD8 percentage were analyzed by flow cytometry.

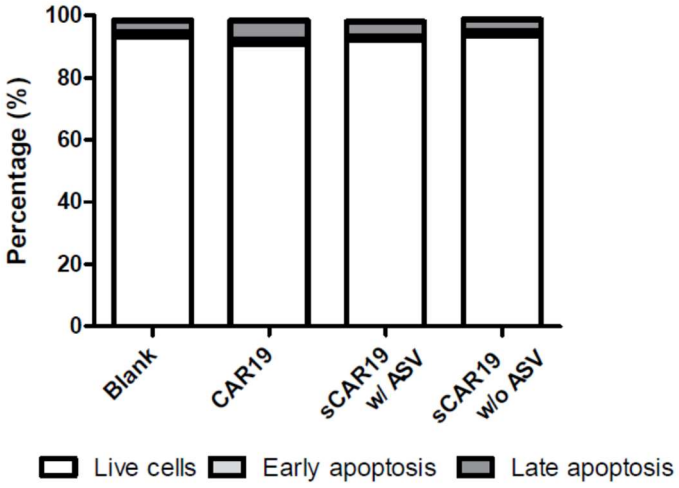

Figure S13. Apoptosis of sCAR19 T cells in the presence of 5 μM ASV. Apoptosis was tested after 3 days of ASV incubation. The apoptotic rate of each group showed no significant difference (P >0.05).

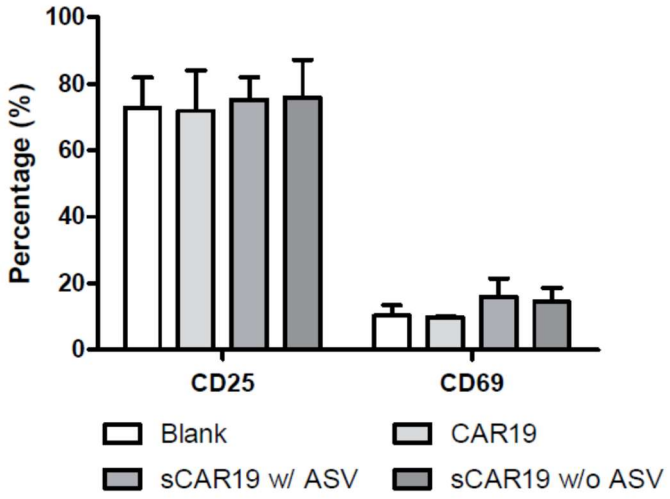

Figure S14. Activation of sCAR19 T cells. CD25 and CD69 were analyzed by flow cytometry after three days culture. The expression of CD25 and CD69 showed no significant difference in four groups (P > 0.05). ASV was provided as 5 μM.

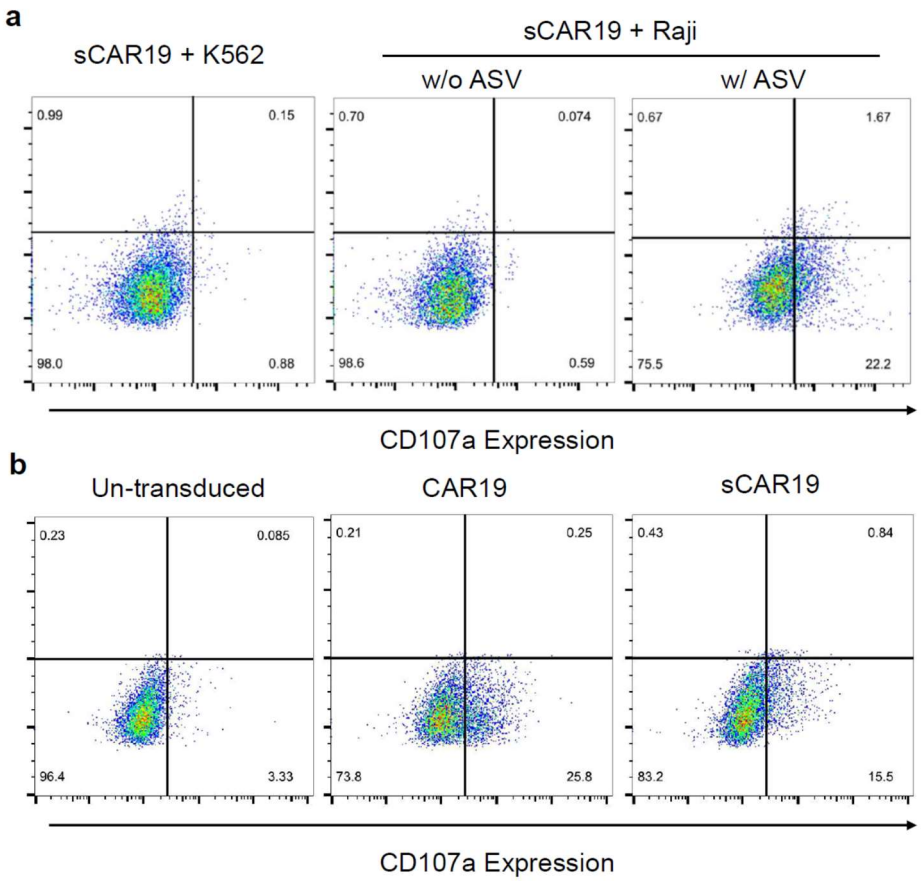

Figure S15. Degranulation analysis of sCAR19 T cells by the detection of CD107a expression. sCAR19 T and target cells were cocultured with and without 1 μM ASV for 4 h and analyzed by flow cytometry. The plots are gated on $CD3^+$ portions. a. sCAR19 cocultured with K562 ($CD19^-$) and Raji ($CD19^+$) with or without 1 μM ASV. For K562 cells, only data in the presence of 1 μM ASV are shown. b. Un-transduced, CAR19 and sCAR19 T cells cocultured with Raji with 1μM ASV.

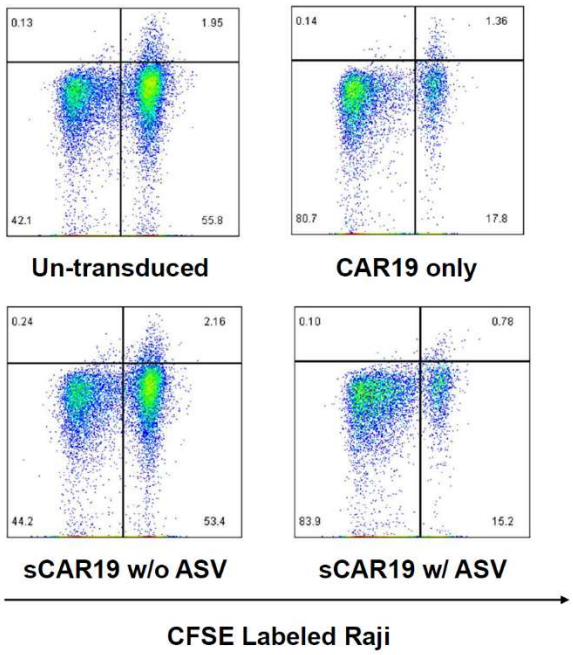

Figure S16. Long-term antitumor effects of sCAR19 T cells in the presence of 1 μM ASV. CFSE labeled Raji cells were cocultured with CAR19 or sCAR19 at low ratio of effector to target cells (E: T = 1: 10). After 72 hours of coculturing, the proportion of $CFSE^+$ Raji cells was detected by flow cytometry.

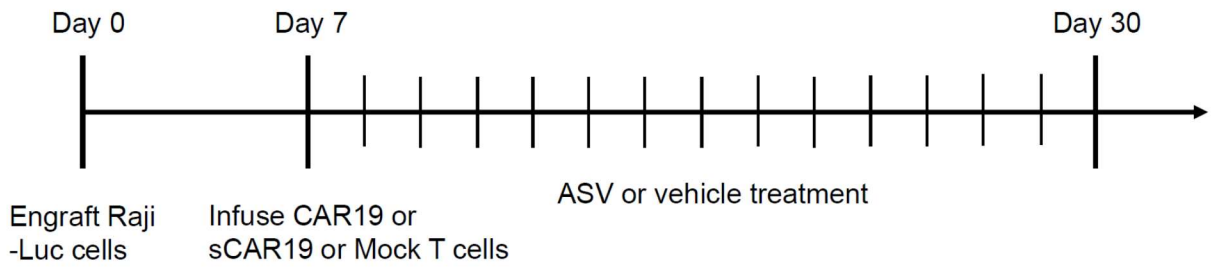

Figure S17. Flowchart of the mouse study. Raji-Luci cells were engrafted on Day 0, then CAR19, sCAR19, or Mock T cells were infused according to the group. ASV or vehicle was given once per day since T cell infusion until Day 30.

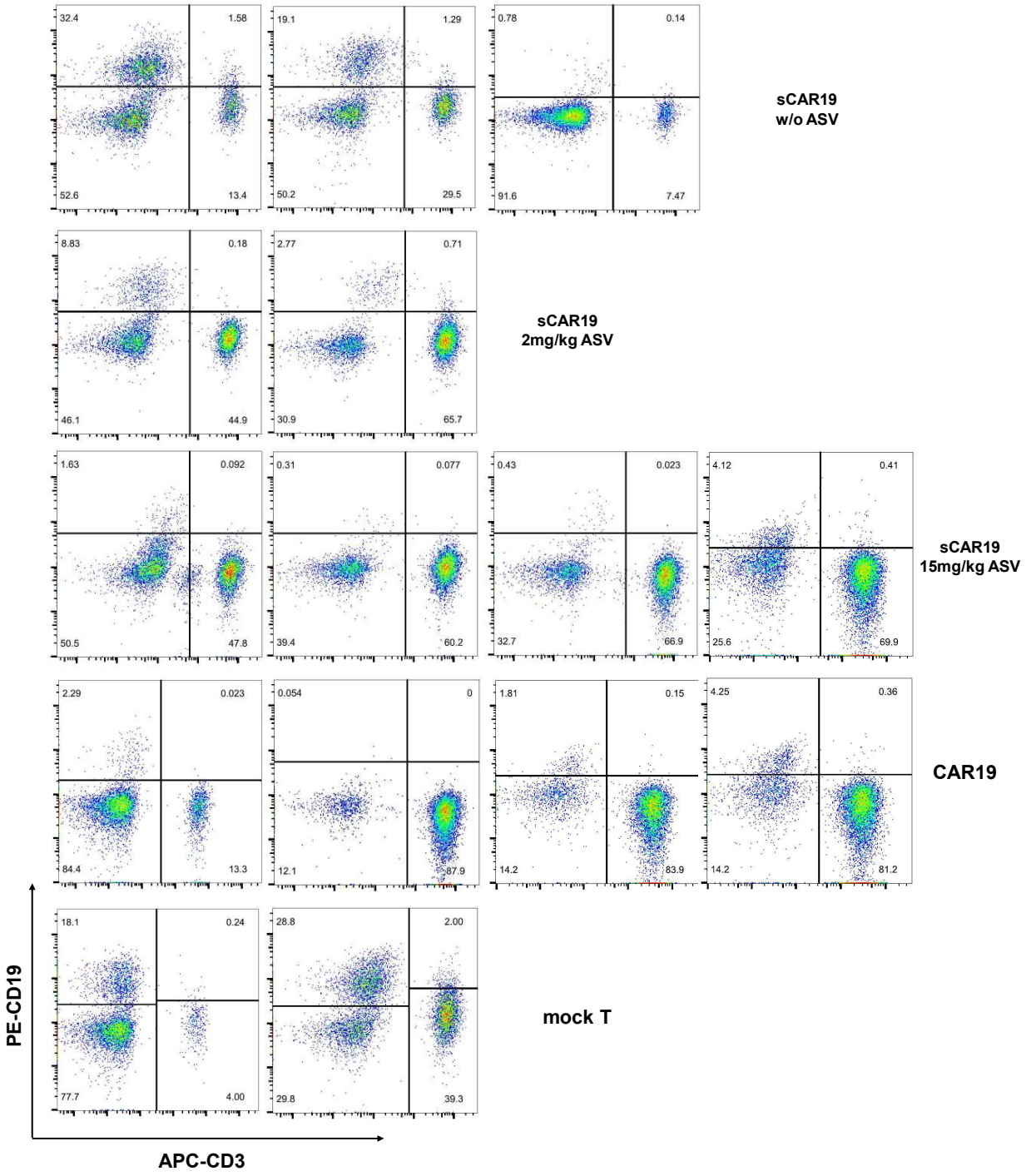

Figure S18. Flow cytometry results of CD3 and CD19 detection of blood in all individual survived mice in different groups in Day 18. Each dot plot represents data for each

particular mouse. APC-CD3 and PE-CD19 were used to differentiate Raji tumor cells and human T cells.

Table S3. Sequence Information

Fragments	**Sequences**
Anti-human CD19 scFv	MALPVTALLLPLALLLHAARPIPDIQMTQTTSSLSASLGDRV TISCRASQDISKYLNWYQQKPDGTVKLLIYHTSRLHSGVPSR FSGSGSGTDYSLTISNLEQEDIATYFCQQGNTLPYTFGGGTK LEITGSTSGSGKPGSGEGSTKGEVKLQESGPGLVAPSQSLSV TCTVSGVSLPDYGVSWIRQPPRKGLEWLGVIWGSETTYYNS ALKSRLTIIKDNSKSQVFLKMNSLQTDDTAIYYCAKHYYYG GSYAMDYWGQGTSVTV
Hinge and cytoplasmic regions	TTTPAPRPPTPAPTIASQPLSLRPEACRPAAGGAVHTRGLDF AFWVLVVVGGVLACYSLLVTVAFIIFWVRSKRSRLLHSDY MNMTPRRPGPTRKHYQPYAPPRDFAAYRSKRGRKKLLYIF KQPFMRPVQTTQEEDGCSCRFPEEEEGGCELRVKFSRSADA PAYQQGQNQLYNELNLGRREEYDVLDKRRGRDPEMGGKP RRKNPQEGLYNELQKDKMAEAYSEIGMKGERRRGKGHDG LYQGLSTATKDTYDALHMQALPPR
HCV-NS3 T54A	DEMEECSQHGGSGGSTGCVVIVGRIVLSGSGTSAPITAYAQ QTRGLLGCIITSLTGRDKNQVEGEVQIVSTATQTFLATCING VCWAVYHGAGTRTIASPKGPVIQMYTNVDQDLVGWPAPQ GSRSLTPCTCGSSDLYLVTRHADVIPVRRRGDSRGSLLSPRPI SYLKGSSGGPLLCPAGHAVGLFRAAVCTRGVAKAVDFIPVE NLETTMRSPVFTDNSSPPAVTLTH
Firefly luciferase	MEDAKNIKKGPAPFYPLEDGTAGEQLHKAMKRYALVPGTI AFTDAHIEVDITYAEYFEMSVRLAEAMKRYGLNTNHRIVVC SENSLQFFMPVLGALFIGVAVAPANDIYNERELLNSMGISQP TVVFVSKKGLQKILNVQKKLPIIQKIIIMDSKTDYQGFQSMY TFVTSHLPPGFNEYDFVPESFDRDKTIALIMNSSGSTGLPKG VALPHRTACVRFSHARDPIFGNQIIPDTAILSVVPFHHGFGMF

	TTLGYLICGFRVVLMYRFEEELFLRSLQDYKIQSALLVPTLF SFFAKSTLIDKYDLSNLHEIASGGAPLSKEVGEAVAKRFHLP GIRQGYGLTETTSAILITPEGDDKPGAVGKVVPFFEAKVVDL DTGKTLGVNQRGELCVRGPMIMSGYVNNPEATNALIDKDG WLHSGDIAYWDEDEHFFIVDRLKSLIKYKGYQVAPAELESIL LQHPNIFDAGVAGLPDDDAGELPAAVVVLEHGKTMTEKEI VDYVASQVTTAKKLRGGVVFVDEVPKGLTGKLDARKIREIL IKAKKGGKIAV

Table S4. Primer sequences

Primers	Sequences
CAR19-F1	GGATCTATTTCCGGTGAATTCGCCACCATGGCGCTGCCTG
CAR19-R1	CCGCGGCGCAGGTGTCGTGGTCACCGTAACGGAGGTTCC TTGTCCCCAAT
CAR19-F2	ATTGGGGACAAGGAACCTCCGTTACGGTGACCACGACAC CTGCGCCGCGG
CAR19-R2	AGGTTGATTGTTCCAGACGCGTTTATCTCGGAGGCAGAG CCTGCATATG
NS3-F	GAAGCGACGAAATGGAGGAATGTTC
NS3-R	AGATCCACCATGGGTGAGAGTGACA
Luc-F	CGGAATTCGCCACCATGGAAGACG
Luc-R	GCTCTAGATTACACGGCGATCTTTCC
Lenti-F	CTGTGACCGCATTGCTCCTT
Lenti-R	AGTCCCGTCTGGCTTCTGCT

Table S5. Antibodies and providers

Antibody	Vendor	Part number
Alexa Fluor 647 rabbit anti-mouse F(ab)^2	Jackson ImmunoResearch Laboratories	315-606-003
FITC human CD19	AcroBiosystems	CD9-HF251

PE anti-human CD19	BD Biosciences	561741
FITC anti-human CD3	BD Biosciences	555332
PE anti-human CD4	BD Biosciences	555347
APC anti-human CD3	BioLegend	300412
APC anti-human CD69	BioLegend	310910
PE anti-human CD25	BioLegend	302606
FITC anti-human CD4	BioLegend	317408
APC anti-human CD8a	BioLegend	301014
FITC anti-human CD45	BioLegend	304006
Annexin V Apoptosis Detection Kit	BD Biosciences	V13241
CFSE Cell Proliferation Kit	BD Biosciences	C34570
PE anti-human CD107a	BD Biosciences	560948
Protein Transport Inhibitor	BD Biosciences	554724

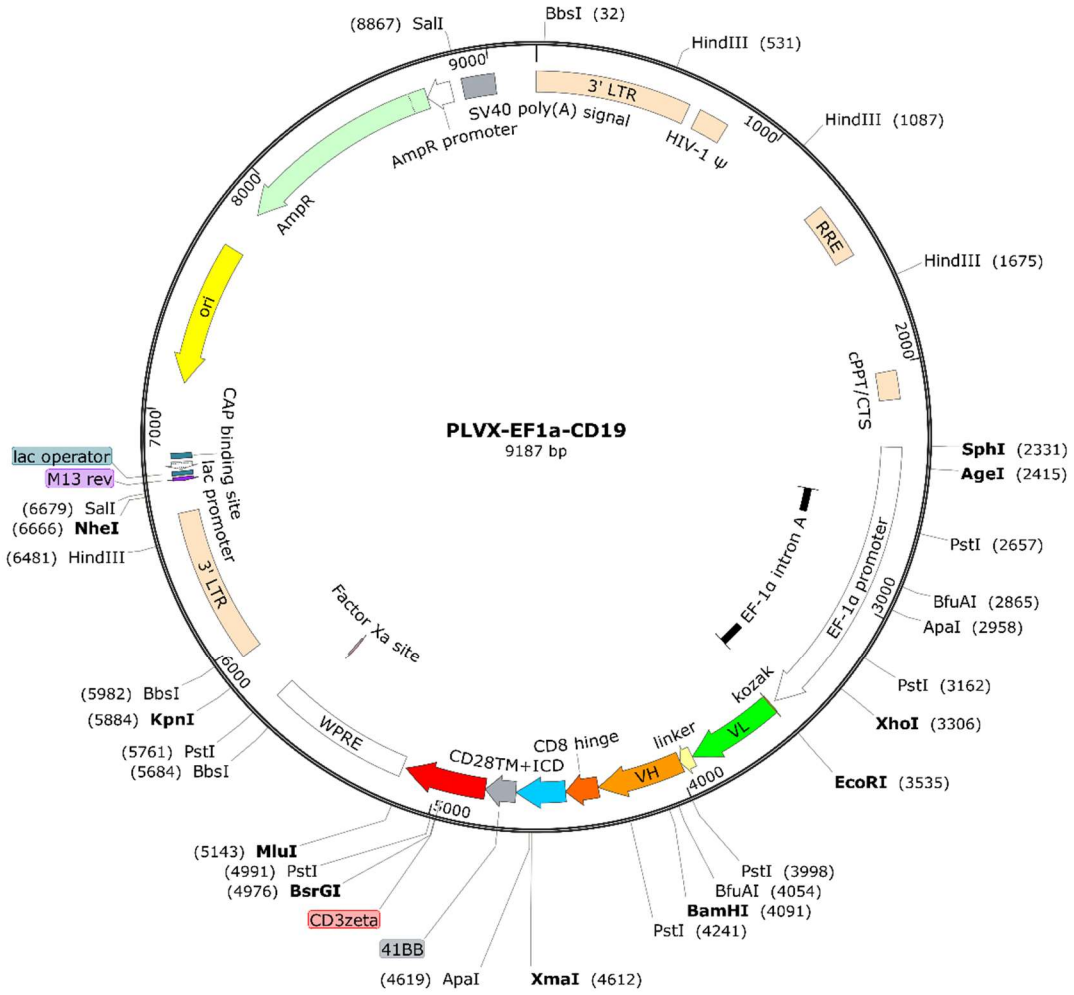

Figure S19. The plasmid map for pLVX-EF1a-CAR19

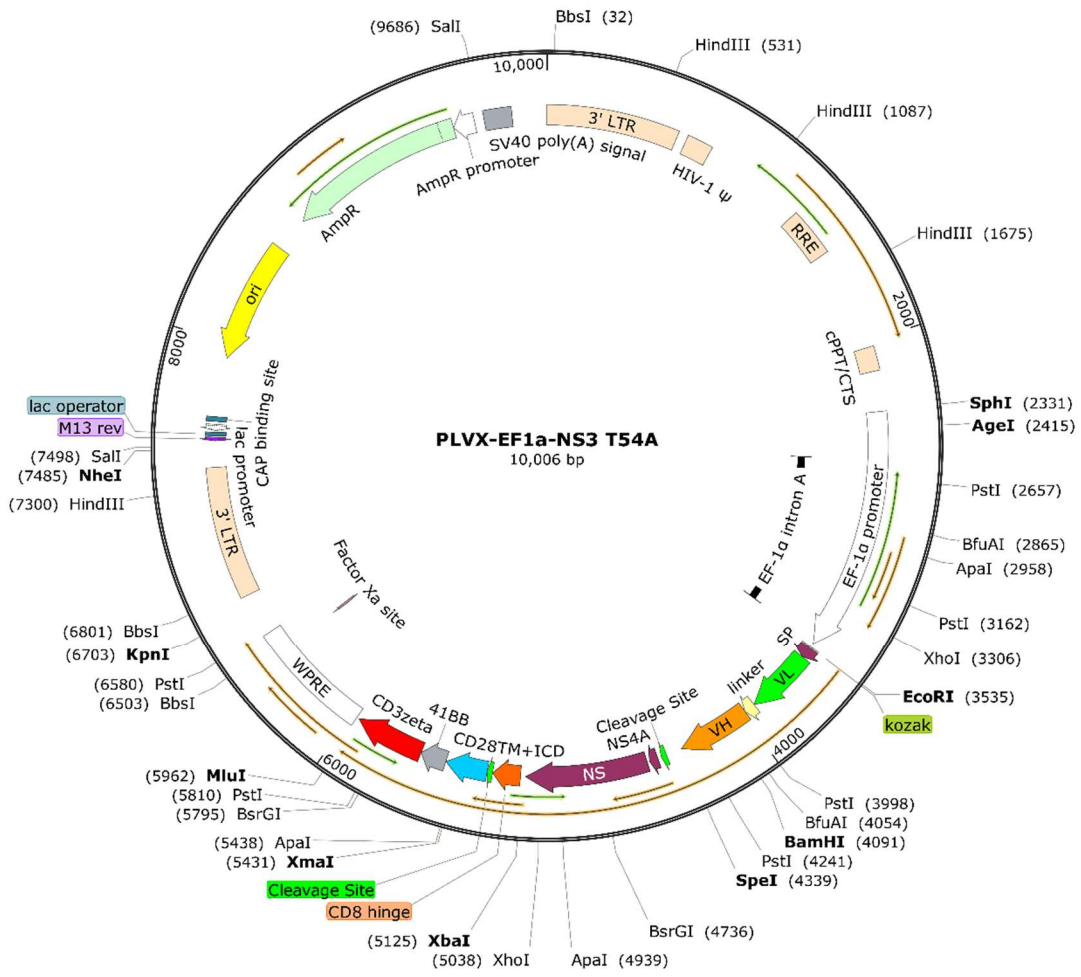

Figure S20. The plasmid map for pLVX-EF1a-sCAR19

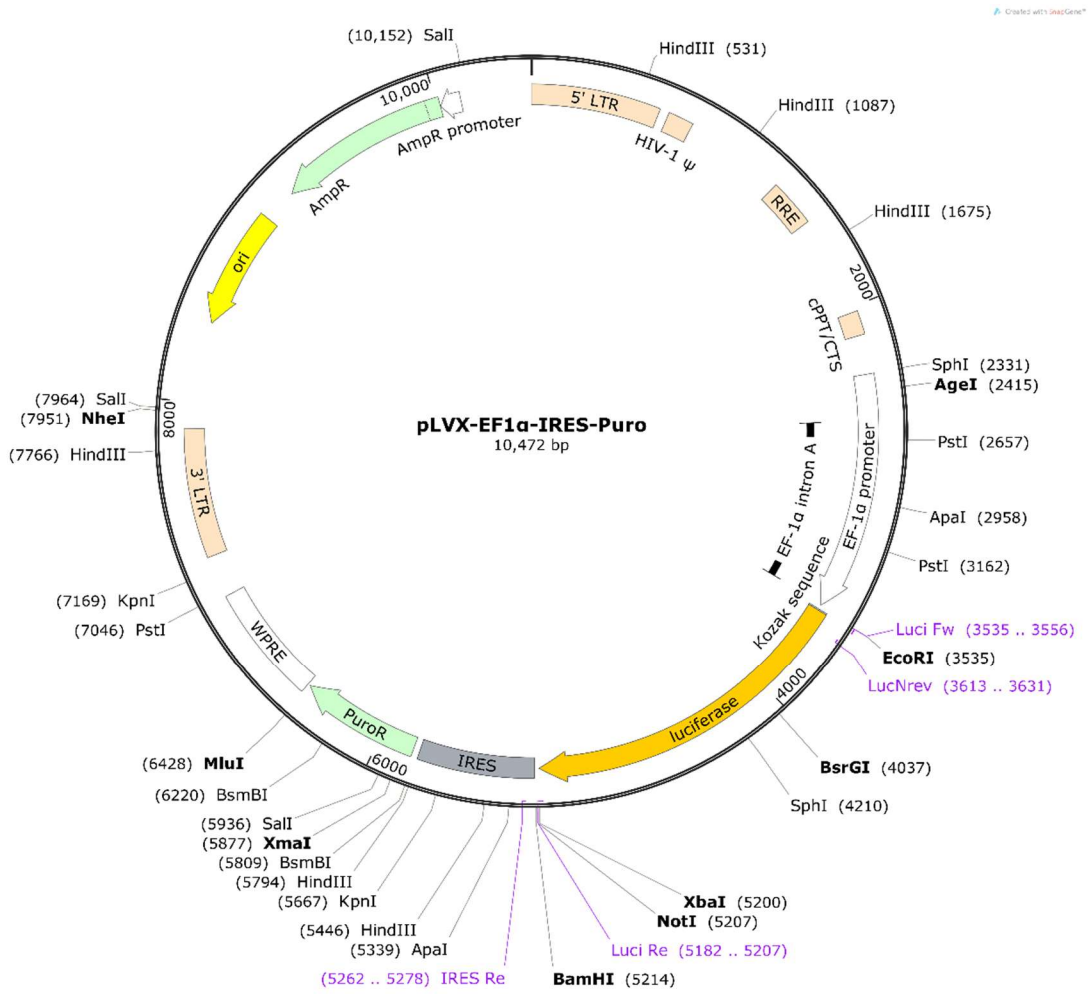

Figure S21. The plasmid map of pLVX-Luc-Puro

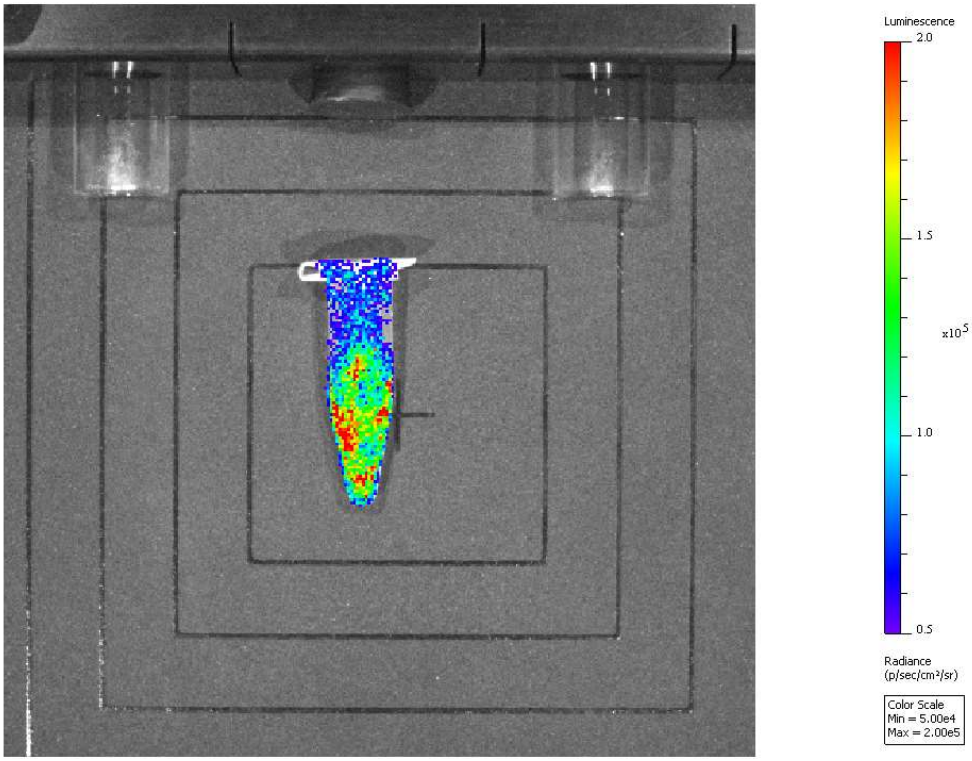

Figure S22. Raji-Luc Cell imaging